RECONCILING MODELS AND OBSERVATIONS OF TYPE IA SUPERNOVAE AND SUPERNOVA REMNANTS

by

Héctor Martínez Rodríguez

B. Sc. in physics, Universidad Complutense, Madrid (2013)

M. Sc. in astrophysics, Universidad Complutense, Madrid (2014)

Submitted to the Graduate Faculty of

the Kenneth P. Dietrich School of Arts and Sciences in partial fulfillment

of the requirements for the degree of

Doctor of Philosophy

University of Pittsburgh

2019

UNIVERSITY OF PITTSBURGH

DIETRICH SCHOOL OF ARTS AND SCIENCES

This dissertation was presented

by

Héctor Martínez Rodríguez

It was defended on

March 27th 2019

and approved by

Dr. Carlos Badenes, Dept. of Physics and Astronomy, University of Pittsburgh

Dr. Desmond John Hillier, Dept. of Physics and Astronomy, University of Pittsburgh

Dr. Michael Wood−Vasey, Dept. of Physics and Astronomy, University of Pittsburgh

Dr. Joseph Boudreau, Dept. of Physics and Astronomy, University of Pittsburgh

Dr. Matthew Walker, Dept. of Physics, Carnegie Mellon University

Dissertation Director: Dr. Carlos Badenes, Dept. of Physics and Astronomy, University of Pittsburgh

RECONCILING MODELS AND OBSERVATIONS OF TYPE IA SUPERNOVAE AND SUPERNOVA REMNANTS

Héctor Martínez Rodríguez, PhD

University of Pittsburgh, 2019

Type Ia supernovae (SNe Ia) are the thermonuclear explosions of carbon-oxygen white dwarfs (WDs) in binary stellar systems. After many decades of research, the nature of their progenitors is still unclear. There are two main proposed channels: the single-degenerate scenario, where the WD companion is a non-degenerate star (e.g. a main-sequence star, a sub-giant, a red giant or a helium star), and the double-degenerate scenario, where the WD companion is another WD. Some observational probes, such as the neutron excess in the supernova ejecta and the amount and shape of the circumstellar material left behind in the post-explosion supernova remnant (SNR), are sensitive to the properties of the progenitor before, during and after the thermonuclear runaway. Here, we compare the predictions from models of pre-explosion single-degenerate scenarios, explosive nucleosynthesis, and expanding SNRs with real X-ray spectra of SNRs in order to elucidate the properties of their progenitors. We find that a) there is observational evidence for high neutronization in several Type Ia SNRs, b) this neutron-rich content in the supernova ejecta cannot be explained by current chemical evolution models, as it is in tension with the metallicity distribution functions of the Milky Way and the Large Magellanic Cloud, pointing to a different source for the neutron excess, and c) simple one-dimensional hydrodynamical models with uniform ambient media for expanding SNRs are able to reproduce the bulk properties (Fe Kα centroid energy and luminosity, radius and expansion age) of most known Ia SNRs, with a few exceptions.

TABLE OF CONTENTS

LIST OF TABLES

LIST OF FIGURES

A mis padres

PREFACE

Mientras la ciencia a descubrir no alcance
las fuentes de la vida,
y en el mar o en el cielo haya un abismo
que al cálculo resista,
mientras la humanidad siempre avanzando
no sepa adónde camina,
mientras haya un misterio para el hombre,
¡habrá poesía!

Gustavo Adolfo Bécquer

Coming to the United States to do a PhD and work at NASA was my long-life dream. When I was a young kid and told my parents about it, they used to smile with the kind leniency we adults show when dealing with infants, probably thinking that it was one of those childhood dreams that never get fulfilled. These lines prove that that little kid raised in a working-class neighborhood in Madrid (Marqués de Vadillo, Carabanchel) gave his all, and foremost, was given the chance to make it come true.

I would like to start by thanking my advisor, Carles, for having given me the chance to do research under his guidance, and for his excellent and thoughtful supervision, introducing me to our excellent collaborators. I remember the moment, in October 2014, when he showed me his funded NASA proposal that would eventually become my PhD dissertation. Before that, when I was still in Madrid, he and I had a Skype teleconference where he made me realize that going to Pittsburgh to pursue my PhD was a good idea. I accepted the offer on

March 18th, 2014, and came to the US on August 2nd, 2014, so long ago.

I want to thank my parents, as they have always supported me in countless, difficult moments, being there for me. My strong passion for reading, for knowledge, comes from them. I also want to thank the rest of my family back in Spain, who always believed in me.

Regarding my life in Pittsburgh, I thank Marina and Daniel for having given me the chance to do my PhD at this university, as it would never have happened without them, and Arthur, for our encouraging email exchanges during my application process. Simone, for having eased my transition from Spain to America, offering me to become his roommate and constantly giving me information and advice. Ayres, Andrew and Adam, for their righteousness and support during my first semester here. Sandhya, for her reassuring words and for having made me love being an astronomy teaching assistant. Leyla, for her constant help. Jonny and Clarisse, for their unconditional friendship since I arrived to Pittsburgh. Kevin, for our conversations about Fortran when I started to learn that programming language and for having been my office buddy. Dritan, for understanding my homesickness-related tribulations. Christine, my "academic sister", for having made me feel fully integrated in the US. My numerous Spanish friends in here, for our happy and funny outings that helped me bring home a little closer ("*siempre, a gañote*").

There are many astrophysicists who have made this journey fascinating and from whom I have learned more than I ever dreamed of. Tony, who has been a second PhD advisor to me, guiding me through my first paper, as well as Josiah, who fully introduced me to the `MESA` code and gave me his unconditional help. Hiroya, who gave me the chance of doing research at NASA during those three weeks I shall never forget, and who taught me how to do *Suzaku* data reduction. Eduardo, my "academic grandfather" who introduced me to the realm of supernova explosion models and has supported me since. Frank, for having believed in me as a scientist, for all his help and for having bestowed me upon attending the `MESA` summer school in Santa Bárbara as a teaching assistant, a priceless experience that I cherished at the very moment I started using the code. Katie, for inviting me to visit her at the Ohio State University many times, including a whole month in Columbus, for being such a nice host and for her guidance. Lluís, for our many conversations in the office, especially during my fourth year, and for his guidance. Herman and Dan, for sharing their `ChN` with

me and patiently teaching me how to use it. Wolfgang, for polishing my statistical analyses. I am going to miss you all.

I am especially grateful for having so many friends from my life in Madrid who, in spite of the long distance, have always been there to encourage me and give me their support. This long journey might have become untenable had it not been for them. My friends from my neighborhood, my "*monchitos*", Sergio, Miguel, Mateo, Rubén, Álvaro and José Manuel (in order of historical acquaintance), who have always been there and with whom I have grown and shared a deep friendship since my teen ages, back in secondary school. My friends from high school, Celia (who came back to my life after many years apart), Miguel Ángel (that many walks together in Madrid), and Javi (who was also my buddy in college), for having befriended me during those onerous years. Raúl, whom I met in the Spanish Physics Olympiad, for talking to me every day (*el Retiro* is waiting for us). My friends from college, Laura (thank you for being so proud of me), Joserra (*siempre nos quedará California, y el Carabirubí*, thank you for having given me shelter in Barcelona), Carlos (that second year was truly complicated in many different ways), Jesús (great minds think alike), Lucía, Irene and Lucía, with whom I have shared precious moments while surviving to our everlasting and tortuous undergrad in physics, and Virginia, with whom I shared heartwarming moments, especially when celebrating our birthdays. Amparo, for believing in me and opening my eyes. Irene, for your empathy and our frequent conversations. Paula and Elena, though from the distance, for having shared this American experience with me. My friends from my master's degree, who befriended me the year before I came to the United States, my happiest moments ever: Igone, for your support and for having let me stay at your apartment when I went to Leiden; Sabina, for our deep conversations every time I have gone back home.

I want to thank several teachers and professors back in Madrid, such as Miguel Ángel, Luis, Esther, Javier, Ana, Julián, Felipe, Gabriel, Artemio, Javier, Gemma, Juan Pedro, Ricardo, Jaime, Antonio, and especially David and José Antonio, who introduced me to doing research in astrophysics. Our weekly Friday meetings to discuss exoplanets are among some of my happiest moments as a researcher. Last, but not least, if I forgot to thank anybody, please be aware that it has not been intentional.

De Marqués de Vadillo al cielo.

I INTRODUCTION

I.1 OVERVIEW

Supernovae (SNe) are energetic stellar explosions that signify the demise of certain types of stars. SNe are rare events, occurring on average twice a century in a galaxy. Typically, a supernova (SN) explosion releases an ejecta kinetic energy $\sim 10^{51}$ erg (e.g. Thornton et al., 1998), which is approximately the total energy the Sun will radiate during its main sequence lifetime of ten billion years. Some SNe can even reach kinetic energies $\sim 10^{53}$ erg (super-luminous, isotropic SNe, Gal-Yam, 2012; Howell, 2017). Hence, SNe are the main source of energy of the interstellar medium (ISM), affecting the local star formation in their environments (Stinson et al., 2006; Dalla Vecchia & Schaye, 2012; Hopkins et al., 2014), and are also essential to understand the chemical enrichment evolution of the Universe (Kobayashi et al., 2006; Matteucci et al., 2006; Andrews et al., 2017; Weinberg et al., 2017; Prantzos et al., 2018). They make many of the elements in nature, from carbon to zirconium, and by extension in our bodies ("stardust").

SNe are also an important source of cosmic rays below their spectrum "knee" (distinctive bump in their intensity coming from elements with atomic numbers < 6) at $0.2 - 0.5$ PeV (Hillas, 2005; Haungs, 2015), and a key to understand gamma-ray bursts (Izzard et al., 2004; Mazzali et al., 2005a; Pian et al., 2006; Woosley & Bloom, 2006; Kaneko et al., 2007). They are the formation sites of neutron stars and stellar mass-black holes (e.g. Woosley et al., 2002; Carroll, 2004; Woosley & Janka, 2005) or pulsar wind nebulae (Weiler & Panagia, 1978). Some supernovae can be used as "standard candles" (see Howell, 2011, for a review) to measure dark energy (Riess et al., 1998; Perlmutter et al., 1999). Consequently, SNe play a relevant role in may fields of astrophysics.

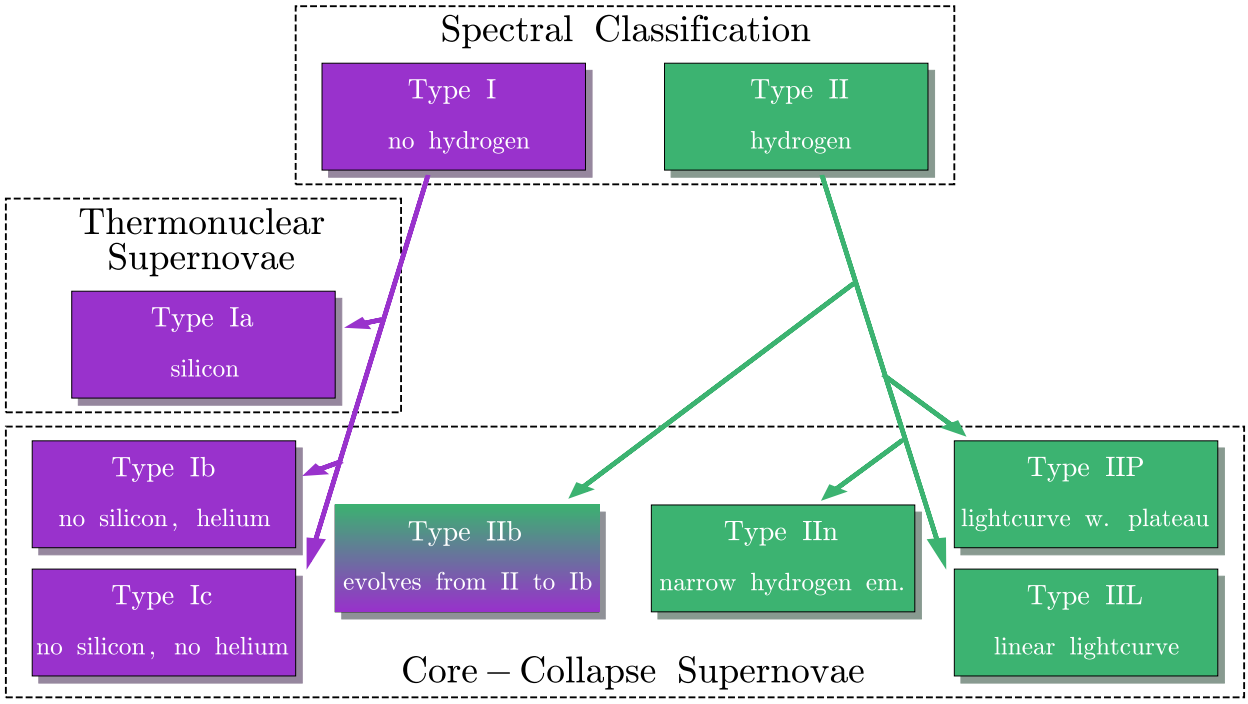

Figure 1: Supernova classification, based on spectral and photometric properties.

I.2 SUPERNOVA CLASSIFICATION

SNe fall into the category of transient events, as their brightness rises and then fades away over time. Several sub-classes of SNe can be distinguished based on their spectral features in the optical near maximum peak brightness and on the evolution of their light curves (Filippenko, 1997). Traditionally, SNe were classified as either Type II or Type I depending on whether or not their spectra showed hydrogen signatures (Minkowski, 1941). The current SN classification originates from this, but distinguishes more sub-categories. Within Type I, there are three sub-types: Type Ia, which show silicon lines, Type Ib, which show helium but not silicon lines, and Type Ic, which show neither silicon nor helium lines. On the other hand, Type II SNe comprise four categories: Type IIb, which evolve from early hydrogen-rich spectra to helium-dominated Ib events near peak maximum, Type IIn, which show narrow hydrogen emission lines, Type IIP, which have a plateau in their light curves (Anderson et al., 2014), and Type IIL, which show a linear decline after maximum (see Gal-Yam, 2017, for a review and an extended classification, and Figure 1 for clarification). Like all classification systems, this oversimplifies a complex reality, as there seems to be a continuous distribution between Type IIP and Type IIL light curves (Anderson et al., 2014; Galbany et al., 2016). Figure 2 illustrates the near-maximum spectra of various types of SNe.

There is yet another way to label SNe, based on a different physical approach: *the nature of their progenitor systems*. Following this, there are two main SN categories: thermonuclear and core-collapse supernovae (CC SNe). The former encompasses Type Ia SNe (SNe Ia), while the latter covers the rest of the SN types (see Figure 1), whose diversity is a consequence of the mass of the progenitor and the mass loss history after the explosion (e.g., Woosley et al., 2002). The light curves of SNe Ia are powered by the radioactive decay $^{56}\mathrm{Ni} \rightarrow {}^{56}\mathrm{Co} \rightarrow {}^{56}\mathrm{Fe}$, with decay half-lives of 6 and 77 days, respectively. At late times $\gtrsim$ 300 days after the explosion, $^{57}\mathrm{Co} \rightarrow {}^{57}\mathrm{Fe}$ and $^{55}\mathrm{Fe} \rightarrow {}^{55}\mathrm{Mn}$, with decay half-lives of 272 and 1000 days, respectively, become dominant (Seitenzahl et al., 2009). The light curves of Type IIP CC SNe are powered by a post-collapse shock, whereas for some super-luminous supernovae it is the interaction with the surrounding medium that originates the light curve.

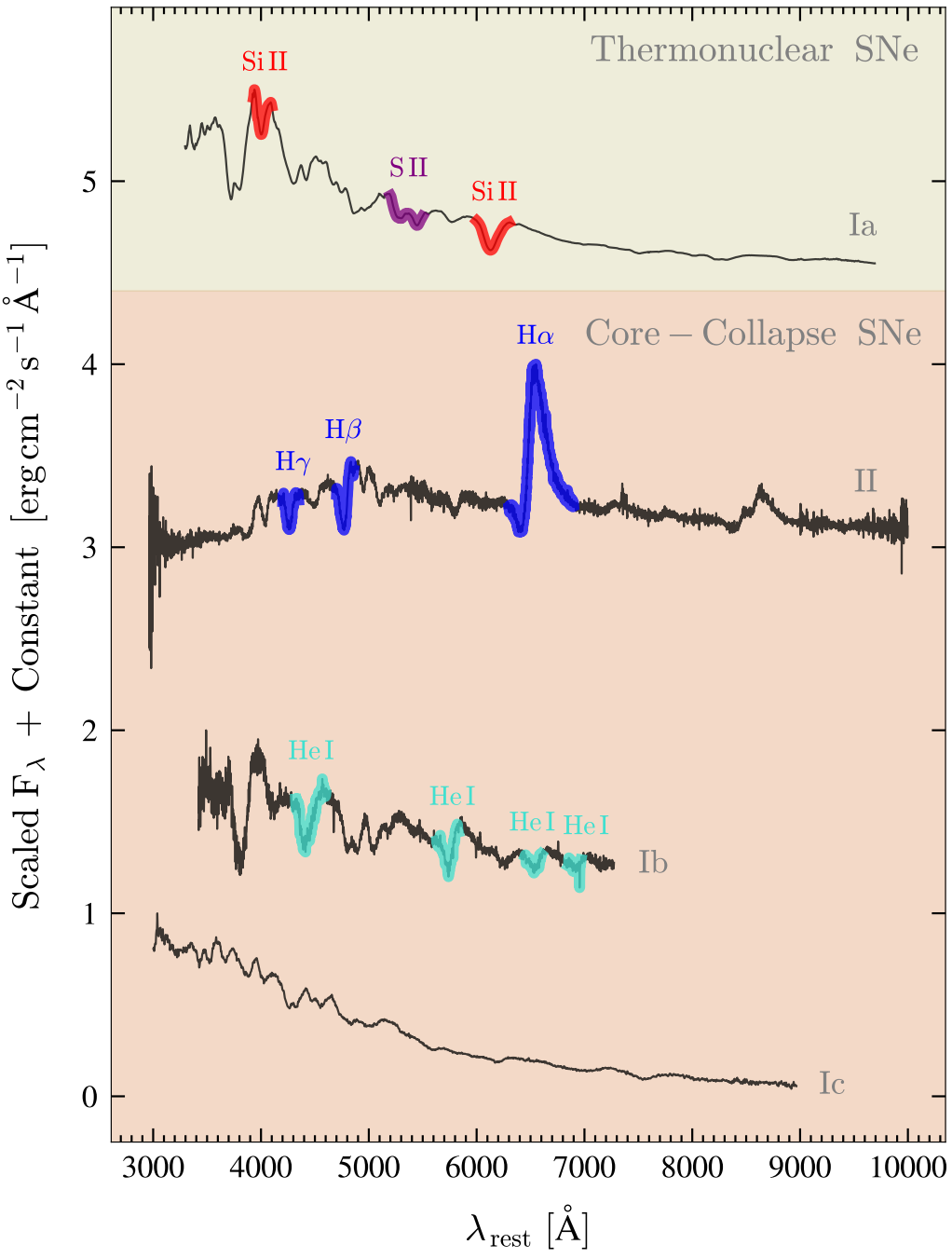

Figure 2: Optical and near-infrared spectra for representative supernova types: Ia (SN2011fe, Aldering et al., 2002; Pereira et al., 2013), II-P (CSS141118:092034+504148, Yaron & Gal-Yam, 2012; Arcavi et al., 2017), Ib (SN2005bf, Tominaga et al., 2005; Modjaz et al., 2014), Ic (SN2015bn, Yaron & Gal-Yam, 2012; Nicholl et al., 2016). The supernova phases are -0.8, -2, -1 and -1 days from maximum, respectively. Data taken from the Open Supernova Catalog (Guillochon et al., 2017).

I.2.1 Core-collapse supernovae

CC SNe are the endpoints in the evolution of massive stars ($M \gtrsim 8\,M_{\odot}$, Woosley et al., 2002; Woosley & Heger, 2007). These stars are initially powered by main sequence-hydrogen burning, followed by helium, carbon, oxygen, and finally silicon burning into iron-peak elements. When each fuel is depleted, the star contracts because of energy losses, as the efficiency of energy production diminishes in each successive burning stage, the star's central temperature increases, and the losses from neutrino-antineutrino pairs increase dramatically (Janka, 2012). Every burning process leaves some unburned ashes (see Farmer et al., 2016; Sukhbold et al., 2016; Fields et al., 2018, for recent models of each burning stage and the impact of the nuclear reaction rates). CC SNe mainly contribute to the chemical enrichment of the Universe via α-elements (e.g. Arnett, 1996).

The sharp decrease in the energy yield for fusion reactions with increasing mass number drives the star to burn fuel increasingly faster to compensate gravity and maintain its equilibrium. While hydrogen burning lasts for millions of years, silicon burning only takes a couple of weeks (Woosley et al., 2002; Woosley & Janka, 2005). As the binding energy per nucleon reaches a maximum for iron, no more nuclear energy can be produced, and the star collapses into its iron core, which can no longer support itself, when the mass of this core surpasses the Chandrasekhar limit ($M_{\rm Fe} \sim 1.4 - 1.8\,M_{\odot}$ for initial masses $M \in 15 - 30\,M_{\odot}$, Farmer et al., 2016). The repulsive, residual, strong nuclear force stops and thereafter reverses this gravitational collapse. The proto-neutron star bounces and creates a shock that propagates through the envelope, powering up the light curve of the CC SN (O'Connor, 2017).

Depending on the properties of the progenitor and of the explosion (Nomoto & Hashimoto, 1988; Woosley & Weaver, 1995; Limongi & Chieffi, 2003; Nomoto et al., 2013; Ofek et al., 2014), massive stars will either keep or lose their hydrogen envelope, which explains the distinction between Type Ib-c and Type II SNe (see Section I.2). Likewise, the progenitor mass determines whether the collapsed iron core will become a neutron star or whether it will become a black hole (Woosley & Weaver, 1995; Timmes et al., 1996; O'Connor, 2017; Horvath & Valentim, 2017). In the first case, a rotating progenitor with sufficiently high spin could enhance the transient's luminosity (Sukhbold & Woosley, 2016).

I.2.2 Thermonuclear supernovae

For stars with low main-sequence masses ($M \lesssim 8\,M_{\odot}$), the evolutionary picture differs from the one that was explained in Section I.2.1. Such stars, in their post-main sequence stages, cannot reach sufficiently high central temperatures and densities to achieve oxygen fusion and lose most of their envelopes. Consequently, they will have inert carbon-oxygen (C/O), oxygen-neon (O/Ne) or He cores with thin, outer hydrogen-helium layers. These are called white dwarfs (WDs). The WD mass distribution ranges between $M \sim 0.4 - 1.2\,M_{\odot}$, being $M \sim 0.6\,M_{\odot}$ a typical value for a C/O WD (Kalirai et al., 2005, 2008, 2009, 2014).

In C/O WDs, the C/O abundance ratio depends on the initial mass and on the uncertainties in the nuclear reaction rates (such as the α-capture by ^{12}C, $^{12}\mathrm{C}(\alpha,\gamma)^{16}\mathrm{O}$, Fields et al., 2016). The third most-abundant isotope in C/O WDs, after ^{12}C and ^{16}O, is ^{22}Ne, whose mass fraction equals the progenitor metallicity (Timmes et al., 2003). For stars with $M \sim 8\,M_{\odot}$, oxygen burning can be achieved, which results in an oxygen-neon (O/Ne) WD (Nomoto et al., 1984; Ritossa et al., 1996; Woosley et al., 2002) unless the star undergoes off-center carbon burning during the post-asymptotic giant branch, which creates a hybrid C/O/Ne WD with an O/Ne/Na mantle (see Brooks et al., 2017, and references therein). Finally, He WDs are not the product of single stellar evolution, as their progenitors would have $M \lesssim 0.5\,M_{\odot}$ and thus would be unable to leave their main sequences before the Hubble time. They originate from the binary evolution of stellar systems where the Roche lobe overflow takes place before the onset of helium ignition in the primary star (Webbink, 1984; Althaus & Benvenuto, 1997; Driebe et al., 1998; Althaus et al., 2010)

SNe Ia are the thermonuclear explosions of C/O WDs stars in binary systems (Hoyle & Fowler 1960; see Bloom et al. 2012; Maoz et al. 2014 for a review, and Toonen et al. 2012 for an analysis of the binarity of the local WD population). O/Ne WDs are expected to become electron capture-supernovae, undergoing an accretion-induced collapse (Nomoto et al., 1984; Schwab et al., 2015; Brooks et al., 2017; Schwab et al., 2017). In addition, the high nuclear binding energy in O/Ne WDs would prevent these from exploding as a SN (Shen & Bildsten 2014; although see Marquardt et al. 2015).

After decades of studies on SNe Ia, the exact nature of the dominant channel in their

progenitor systems remains elusive. Observational and theoretical analyses have failed to establish whether the binary companion is a non-degenerate star (the so-called single degenerate, or SD, scenario) or another WD (double degenerate, DD – see Wang & Han 2012; Maoz et al. 2014; Livio & Mazzali 2018; Soker 2018; Wang 2018 for recent reviews). This is known as the *Type Ia supernova progenitor problem*. In both cases, a relatively massive WD explodes after an accretion episode, but there are important differences between them.

In the SD scenario, the WD accretes material from its companion over a relatively long timescale ($t \sim 10^6$ years) by either a strong companion wind or Roche-lobe overflow (Li & van den Heuvel, 1997). This companion can be either a main-sequence star, a subgiant, a He star or a red giant (see Wang & Han, 2012; Maoz et al., 2014, and references therein). Eventually, the thermonuclear runaway ensues when the WD mass approaches the Chandrasekhar limit $M_{Ch} \simeq 1.4\,M_\odot$ (Nomoto et al., 1984; Thielemann et al., 1986; Hachisu et al., 1996; Han & Podsiadlowski, 2004). One of the greatest challenges of this scenario is getting the WD mass to grow and reach this limit, as the range of accretion rates for stable hydrogen burning is extremely narrow ($\dot{M} \sim 1 - 5 \times 10^{-7}\,M_\odot\,\mathrm{yr}^{-1}$, Nomoto, 1982; Wolf et al., 2013), in many cases resulting into nova eruptions on the surface of the WD (e.g., Starrfield et al., 1972; Wolf et al., 2013). In addition, this scenario predicts that there should be surviving companions, whose discovery might be feasible based on atypical physical properties (e.g. composition, rotation, high-velocity features or over-luminosities, Kasen, 2010; Liu et al., 2013a,b; Pan et al., 2013; Shappee et al., 2013; Marion et al., 2016). However, recent searches around known post-explosion SNe Ia have been unable to find those companions (e.g., Krause et al., 2008; Rest et al., 2008a; Kerzendorf et al., 2009, 2012, 2014, 2017; Ruiz-Lapuente, 2018; Ruiz-Lapuente et al., 2018).

In the DD scenario, there are several situations that might lead to a thermonuclear runaway. In general, the most massive ("primary") WD becomes unstable on a dynamical timescale (Iben & Tutukov, 1984) and explodes with a mass either below, equal to, or above M_{Ch} (e.g., Raskin et al., 2009; Sim et al., 2010; van Kerkwijk et al., 2010). One possibility is that the primary WD disrupts the least massive ("secondary") WD by tidal interactions and accretes it in a disk configuration until the final explosion (e.g. Lorén-Aguilar et al., 2009; Pakmor et al., 2012; Schwab et al., 2012; Shen et al., 2012; Toonen et al., 2012). This

way, by accreting C/O-rich material, the primary WD could efficiently increase its mass and ignite carbon in the core. Violent mergers (e.g., Pakmor et al., 2012, 2013) are an alternative possibility. Here, right before the secondary WD is disrupted, carbon burning starts on the surface of the primary WD and a detonation propagates through the whole merger. As an argument in favor of WD coalescence, WDs in the Milky Way merge at a rate larger than that of SN Ia explosions (Badenes & Maoz, 2012). However, an off-center ignition could be likely in WD mergers, which would lead to a hybrid C/O/Ne WD, and in turn, to an accretion-induced collapse that would create a neutron star. On the other hand, DD systems could also originate from the collisions of multiple WDS in sufficiently dense environments (e.g. Raskin et al., 2009; Rosswog et al., 2009; Raskin et al., 2010; Hawley et al., 2012; Kushnir et al., 2013). However, the final collision rates in multiple systems struggle to reproduce the rate of standard SNe Ia (Toonen et al., 2018).

Another possibility, common to both SD and DD progenitors, is the explosion of a sub-M_{Ch} WD. In these so-called sub-Chandrasekhar scenarios (e.g., Woosley & Weaver, 1994; Sim et al., 2010; Woosley & Kasen, 2011; Bravo et al., 2019), the WD cannot detonate spontaneously. Double-detonations (e.g., Shen et al., 2013; Shen & Bildsten, 2014; Shen & Moore, 2014; Shen et al., 2018) are among the most popular models. Here, the WD accretes He-rich material from its companion. Eventually, this He layer becomes unstable, ignites, and sends a shock wave into the core. This blast wave converges and triggers a carbon denotation, which causes the demise of the WD. Alternatively, other sub-M_{Ch} scenarios present pure detonations of WDs with various masses without explaining how these initiated. Remarkably, these analyses have been successfully reconciled with observables such as light curves, nickel ejecta masses, and isotopic mass ratios (Sim et al., 2010; Piro et al., 2014; Yamaguchi et al., 2015; Blondin et al., 2017; Martínez-Rodríguez et al., 2017; Goldstein & Kasen, 2018; Shen et al., 2018; Bravo et al., 2019).

In principle, it might be feasible to discriminate between SD and DD scenarios, given that some observational probes depend on properties such as the pre-explosion mass, the duration of the accretion process and the amount of circumstellar material (CSM) left behind by the progenitor (e.g., Badenes et al., 2007, 2008a; Seitenzahl et al., 2013a; Margutti et al., 2014; Scalzo et al., 2014; Yamaguchi et al., 2015; Chomiuk et al., 2016; Martínez-Rodríguez et al.,

2016, 2017, 2018). **This has been the main goal of my PhD thesis**.

I.3 TYPE IA SUPERNOVA EXPLOSIONS AND NUCLEOSYNTHESIS

I.3.1 Explosion mechanisms

SNe Ia mainly contribute to the chemical enrichment of the Universe with stable isotopes of iron-peak elements (iron, chromium, manganese, nickel, Matteucci & Tornambe, 1987; Matteucci et al., 2009; Maoz & Graur, 2017; McWilliam et al., 2018; Prantzos et al., 2018), which are synthesized in the inner layers of the exploding WD, and with silicon. The intermediate-mass elements (e.g. sulphur, argon, calcium) are produced in regions with partial burning, whereas there can be some unburned C/O material in the outer layers (e.g. Hillebrandt & Niemeyer, 2000). Among all the elements produced in the explosion, ^{56}Ni (alongside with the kinetic energy of the explosion) has the strongest influence in the shape and evolution of the light curve (e.g., Colgate & McKee, 1969; Arnett, 1982; Bersten & Mazzali, 2017).

There are several mechanisms that can explain the burning front propagation through the exploding WD. If the WD mass is close to M_{Ch}, both pure deflagrations (Nomoto et al., 1984) and delayed detonations (Khokhlov, 1991) are feasible. For sub-M_{Ch} scenarios, it propagates as a pure detonation (Woosley et al., 2004; Sim et al., 2010; Woosley & Kasen, 2011).

In a pure deflagration, the strong electron degeneracy boosts a carbon flash into the final runaway. A burning flame, subsonic with respect to the unburned material, slowly propagates across the WD ($v_0 \sim 0.03 - 0.1\ v_{\rm sound}$). The WD expands, which eventually weakens the explosive burning (Nomoto et al., 1984). These models, in general, struggle to reproduce the yields of iron-peak elements in SNe Ia.

In a pure detonation, a supersonic shock originated by external compression causes the demise of the WD. The less massive the WD, the greater the amount of intermediate-mass elements will be synthesized, and the lower the yields of iron-peak elements. The amount of ^{56}Ni, and thereby the brightness of the SN, is directly determined by the progen-

itor mass. Some of these calculations are unable to account for the high-velocity features ($v \sim 10^4$ km s^{-1}, Mazzali et al., 2005b) of silicon in the spectra of SNe Ia (Zhao et al., 2015). Recent work by Wilk et al. (2018), though, was able to reproduce the high-velocity features of calcium.

Given these difficulties to reproduce some of the observed properties of SNe Ia by pure deflagrations and pure detonations, delayed-detonations (DDTs) combine both explosion mechanisms (Khokhlov, 1991). The explosion starts as a subsonic deflagration, during which the WD expands, and turns into a supersonic detonation at a given deflagration-to-detonation transition density ($\rho_{\rm DDT} \gtrsim 10^7$ g cm^{-3}, e.g. Yamaguchi et al., 2015; Bravo et al., 2019). The higher this transition density, the more iron-peak elements will be synthesized, and thus the brighter (determined by the amount of ^{56}Ni) the SN explosion will be. The DDT models introduced in Martínez-Rodríguez et al. (2018) and Bravo et al. (2019) show a slight increase in the kinetic energy with increasing $\rho_{\rm DDT}$ ($E_k\,[10^{51}\,{\rm erg}] = 1.18, 1.31, 1.43, 1.49$ for $\rho_{\rm DDT}\,[10^7\,{\rm g\,cm^{-3}}] = 1.2, 1.6, 2.4, 4.0$).

I.3.2 Nucleosynthesis and neutron-rich isotopes

The stable isotopes of chromium, manganese and nickel (secondary iron-peak elements, Iwamoto et al., 1999) are especially relevant to chemically tag the progenitors of SNe Ia, as they keep information about both pre-explosion and explosion features of the SN, such as the number of neutrons per proton and the density of the exploding WD (see Badenes et al., 2008a; Bravo, 2013, for a discussion). To understand how these are produced, it is necessary to analyze the different burning regimes in SNe Ia (Thielemann et al., 1986, see Table 1). These are determined by the physical conditions of the fuel (T, ρ), and thus will take place in different regions of the WD. The iron-peak elements are synthesized in three regimes: explosive silicon burning, nuclear statistical equilibrium (NSE) and neutron-rich nuclear statistical equilibrium (n-NSE).

Explosive silicon burning is characterized by the partial photodisintegration of ^{28}Si and by the production of heavier nuclei, such as ^{32}S, ^{36}Ar, ^{40}Ca, ^{56}Ni and small traces of ^{58}Ni, ^{55}Co and ^{52}Fe. ^{58}Ni is a stable isotope, whereas the other two eventually decay to stable

Table 1: Thermonuclear burning regimes in SNe Ia (adapted from Thielemann et al., 1986).

Burning regime	**Physical conditions** (T, ρ)	**Main yields** (after nuclear decays, unburned fuel in brackets)
Explosive C-Ne burning	$T \lesssim 3.2\,GK$	[C, Ne], O, Ne, Mg, Si
Explosive O burning	$3.2\,GK \lesssim T \lesssim 4.5\,GK$	[O], Si, S
Explosive Si burning	$4.5\,GK \lesssim T \lesssim 5.5\,GK$	[Si, S], Ar, Ca, **Cr, Mn, Fe, Ni**
NSE	$T \gtrsim 5.5\,GK$, $\rho \lesssim 10^8\,g\,cm^{-3}$	**Fe, Ni**
n-NSE	$T \gtrsim 5.5\,GK$, $\rho \gtrsim 10^8\,g\,cm^{-3}$	**Cr, Mn, Fe, Ni**

manganese and chromium, $^{55}Co \rightarrow {}^{55}Fe \rightarrow {}^{55}Mn$ and $^{52}Fe \rightarrow {}^{52}Mn \rightarrow {}^{52}Cr$.

NSE occurs at slightly higher temperatures than explosive silicon burning. ^{28}Si gets depleted, rearranging into ^{56}Ni, ^{58}Ni, ^{57}Fe and ^{60}Ni. The abundances are determined by a set of coupled Saha equations that depend on the density, on the temperature and on the number of free electrons per proton (Y_e), or equivalently, on the neutron excess $\eta = 1 - 2Y_e = \sum_i X_i\ (N_i - Z_i)\ /\ A_i$, where X_i, N_i, Z_i and A_i are the mass fraction, neutron number, charge and nucleon number of element i. The higher the neutron excess, the higher the abundance of ^{58}Ni (Hartmann et al., 1985).

n-NSE only takes place in the inner, densest regions ($\sim 0.2\,M_\odot$) of a WD exploding close to M_{Ch}. The densities of the degenerate material (and therefore, the Fermi energy) are high enough for electron captures to take place during nucleosynthesis, shifting the equilibrium point of NSE away from ^{56}Ni to more neutron-rich species like ^{55}Mn and ^{58}Ni regardless of the fuel composition (Iwamoto et al., 1999; Brachwitz et al., 2000).

As the main contribution to the yields of neutron-rich stable manganese and nickel comes from n-NSE, exclusive of M_{Ch}-WDs, **the neutron excess provides a way to discriminate between progenitor systems, and therefore, to tackle the Type Ia progenitor**

problem (see Badenes et al., 2008a; Park et al., 2013; Yamaguchi et al., 2015; Martínez-Rodríguez et al., 2016, 2017). Aside from n-NSE, there are another two ways to enhance the fuel η before the explosion: ^{22}Ne and carbon simmering.

As mentioned in Section I.2.2, ^{22}Ne is the third most-abundant isotope in WDs after ^{12}C and ^{16}O, which have zero η. Intermediate-mass stars ($2\,M_\odot \lesssim M \lesssim 7\,M_\odot$) burn hydrogen during their main sequence via the CNO cycle, whose slowest, bottle-neck reaction is ^{14}N(p,γ)^{15}O. At the end of hydrogen burning, most of the metals in the progenitor pile up onto ^{14}N, which in turn becomes ^{22}Ne during hydrostatic helium burning through the chain ^{14}N(α, γ)^{18}F(β^+, ν_e)^{18}O(α, γ)^{22}Ne. Hence, this isotope contributes to all the neutron-rich material of the final WD. Using these arguments, Timmes et al. (2003) found a linear relation between neutron excess and progenitor metallicity Z: $\eta = 0.1Z$.

This simple relation between Z and η could be modified in M_{Ch}-WDs by means of a process called carbon simmering (Woosley et al., 2004; Wunsch & Woosley, 2004; Chamulak et al., 2008; Piro & Bildsten, 2008; Piro & Chang, 2008; Martínez-Rodríguez et al., 2016; Piersanti et al., 2017; Schwab et al., 2017). After millions of years of slow accretion from a companion, a WD can reach sufficiently high central temperatures and densities to start fusing carbon. Instead of exploding immediately, neutrinos cool the star until the final runaway. The onset of simmering occurs when the heat from carbon burning overcomes the neutrino cooling. A convective core starts growing outwards as way to efficiently transport the energy away from the center until carbon fusion becomes fast enough, which triggers the thermonuclear runaway at a central temperature $T \sim 0.8\,GK$ (Woosley et al., 2004). This convective core expands up to $\sim 1 - 1.2\,M_\odot$ during $\sim 1000 - 10000$ years (Piro & Bildsten, 2008; Piro & Chang, 2008; Martínez-Rodríguez et al., 2016), increasing the neutron excess of the core via the electron capture reactions ^{13}N(e$^-$, ν_e)^{13}C (see Chamulak et al., 2008) and ^{23}Na(e$^-$, ν_e)^{23}Ne (see Chamulak et al., 2008; Piro & Bildsten, 2008, for details). These reactions feed upon the products of carbon fusion, therefore this enhancement in η is directly linked to the amount of carbon consumed prior to the explosion. This increase in η is independent of the progenitor metallicity ("simmering floor" Piro & Bildsten, 2008; Martínez-Rodríguez et al., 2016), but strongly depends on whether convective mixing is advective or whether it is diffusive (Piersanti et al., 2017; Schwab et al., 2017), i.e., on

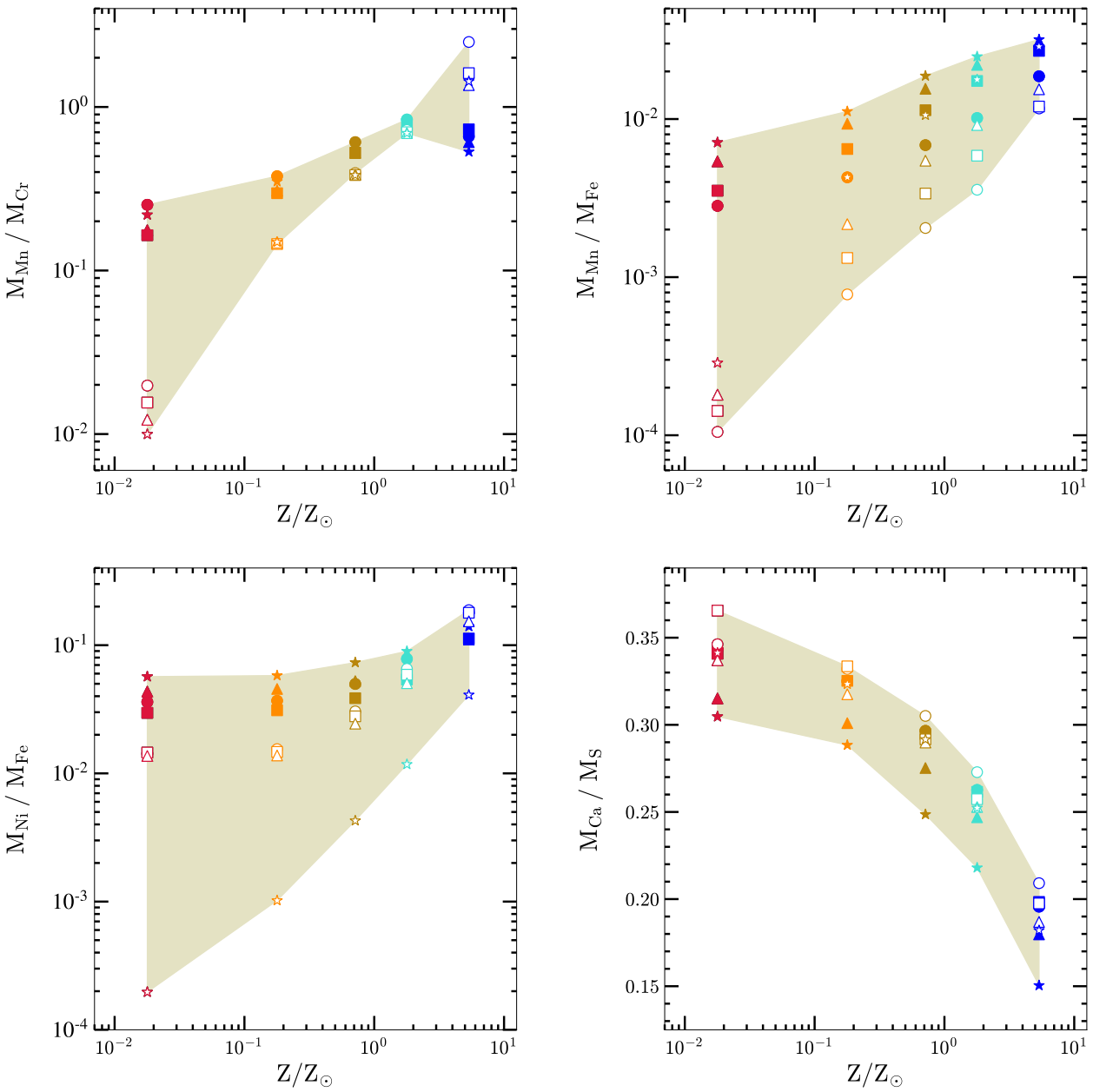

Figure 3: Elemental mass ratios sensitive to either the neutron excess or to the n-NSE burning regime (Badenes et al., 2008a; Yamaguchi et al., 2015; Martínez-Rodríguez et al., 2017) in delayed-detonation, M_{Ch} models (filled symbols) and in pure-detonation, sub-M_{Ch} models (empty symbols) as a function of progenitor metallicity. It is assumed that $Z_{\odot} = 0.014$ (Asplund et al., 2009).

whether particles move along the bulk flow or whether particles move from high-concentration to low-concentration regions.

In conclusion, neutron-rich isotopes in SNe Ia can give clues about their progenitors. Several mass ratios are sensitive to either η (M_{Mn}/M_{Cr}, Badenes et al. 2008a; M_{Ca}/M_S, Martínez-Rodríguez et al. 2017) or to the n-NSE burning regime (M_{Mn}/M_{Fe}, M_{Ni}/M_{Fe}, Yamaguchi et al. 2015). Figure 3 shows these ratios for M_{Ch} and sub-M_{Ch} nucleosynthesis models. M_{Mn}/M_{Cr} and M_{Ca}/M_S slowly increase and linearly decrease with metallicity, respectively. For a given metallicity, M_{Mn}/M_{Fe} and M_{Ni}/M_{Fe} are, in general, substantially lower for the sub-M_{Ch} detonations.

Models of the nebular phase of SNe Ia do not predict any noticeable effects of ^{55}Mn and ^{58}Ni in the spectra (Botyánszki & Kasen 2017; although see Maguire et al. 2018). In addition, the decay $^{55}\text{Fe} \rightarrow {}^{55}\text{Mn}$ has a long half-life of 1000 days. However, it is feasible to quantify these mass ratios in young ($t \gtrsim 100$ years) Ia supernova remnants (SNRs) using X-ray telescopes (see Section I.4), which can constrain essential aspects of the physics of explosions and of the progenitors of SNe Ia.

I.4 SUPERNOVA REMNANTS

During and after the explosion, the SN ejecta expands. At late times $\gtrsim 100$ days, the optical depth of the ejecta decreases due to the reduced column densities, so that it starts becoming optically thin to its own radiation, which is called the SN nebular phase (e.g. Sollerman et al., 2004; Mazzali et al., 2015; Botyánszki & Kasen, 2017; Jerkstrand et al., 2017; Sollerman et al., 2019). The SN spectrum transitions from a blackbody with absorption lines to showing multiple emission lines from the inner ejecta. In addition, all the ejecta reaches homologous expansion (i.e., purely radial velocities with $v = r/t$).

After a few years, when the ejecta density becomes comparable to that of the surrounding medium, either the ISM or a more or less extended circumstellar medium (CSM) modified by the SN progenitor, the supernova remnant phase begins. There is no accepted lower age boundary for this, so "SNR" usually refers to SNe $\gtrsim 100$ years old (Jerkstrand et al., 2017).

The ejecta drive an outwards blast wave into the ambient medium ("forward shock", FS), whereas the pressure gradient creates another wave that shocks the ejecta inwards ("reverse shock", RS; McKee & Truelove, 1995; Truelove & McKee, 1999). The ambient medium and the ejecta are separated by a contact discontinuity (CD). The dynamical evolution of SNRs can be divided into four phases, which depend on the relationship between the ejecta mass and the shocked ambient mass (Woltjer, 1972): free expansion/ejecta dominated, Sedov/adiabatic, "snow plough" and final dissipation (e.g., Reynolds et al., 2008). Figure 4 shows the evolution of a fiducial SN Ia progenitor into the SNR phase during the first two stages, which are called "nonradiative" because radiative losses are insignificant, so that energy is conserved (Woltjer, 1972; Truelove & McKee, 1999).

Oftentimes, SNRs undergoing free expansion are referred as "young" SNRs. In this phase, the emission is dominated by the reverse shock, which heats, compresses and decelerates the expanding ejecta to X-ray emitting temperatures. The RS radius initially increases, but later decreases as it moves towards the center of the SNR. The dynamical evolution can be approximated by means of a self-similar solution that depends on three variables: the ejecta mass, the kinetic energy of the explosion and the ambient medium density (see Equations 9-11 from McKee & Truelove 1995, as well as, e.g., Dwarkadas & Chevalier 1998; Badenes et al. 2003, 2007; Patnaude et al. 2012, 2017; Woods et al. 2017, 2018 to understand the connection with SNR observations). In a nutshell, the denser the ambient medium, the smaller the SNR and the less time it will take for the RS to reach the center (typically a few thousands of years). Due to the low typical densities of the ISM ($n \sim 1\,\mathrm{cm}^{-3}$), the number of ionizing collisions in the SNR plasma is low, therefore the recombination and ionization rates cannot find an equilibrium point (Itoh, 1977; Badenes, 2010). Thus, young SNRs are plasmas in non-equilibrium ionization.

Eventually, the ejecta decelerates due to the increase in the swept-up ambient medium mass. When the shocked medium becomes hydrodynamically relevant, the Sedov phase begins ($\sim 10^3$ years, Shklovskii, 1962; Taylor, 1950; Sedov, 1959; Truelove & McKee, 1999). After $\sim 10^4$ years, when radiative losses become important, and thus energy is not conserved anymore, the "snow plough" phase starts, until the SNR finally merges with the surrounding medium ($\sim 10^6$ years, Reynolds et al., 2008).

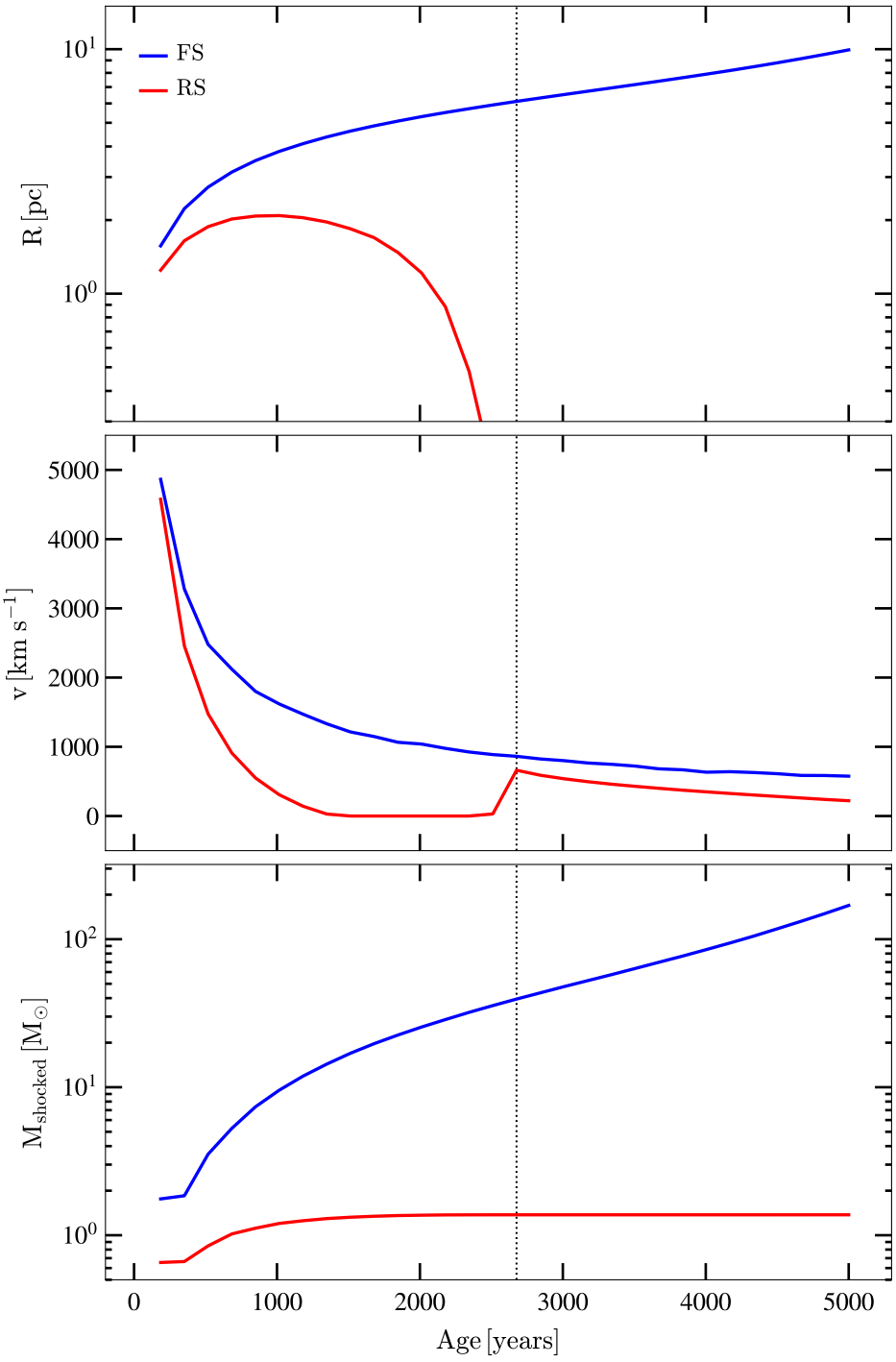

Figure 4: Dynamical evolution (radius, shock velocity and shocked mass) of a DDT explosion into the SNR phase between 20 and 5000 years. The dotted, vertical line marks the age when the RS reaches the center of the SNR, fully shocking the ejecta. Model taken from Martínez-Rodríguez et al. (2018).

Unless a pulsar is detected at the center of a SNR, it can be difficult to classify it as Ia or CC, but Yamaguchi et al. (2014a) proposed a successful method using the centroid energy (ionization) of the Fe Kα emission as a diagnostics tool. As the CSM around CC SNRs is expected to be denser than that around Ia SNRs due to the strong mass loss from the pre-explosion progenitor, the number of ionizing collisions should be enhanced in CC plasmas, which shifts the Fe Kα to higher values and therefore separates both types of progenitors. Combining this measurement with its corresponding line luminosity discriminates between bright and dim SNe, while doing so with the remnant's physical size reveals whether the ambient medium around the SNR is uniform or whether it has been strongly modified by the progenitor (Patnaude & Badenes, 2017).

In conclusion, young SNRs, and especially their X-ray spectra, show imprints from both the chemical and physical composition of their progenitors and the structure of their surrounding CSM / ISM sculpted before the explosion (e.g., Badenes et al., 2005, 2006, 2008b; Badenes, 2010; Vink, 2012; Lee et al., 2013, 2014, 2015; Slane et al., 2014; Patnaude et al., 2015). SNRs can thus put strong constraints on fundamental aspects of both SN explosion physics and stellar evolution scenarios for SN progenitors (Badenes, 2010). X-ray analyses of SNRs are independent of, and complimentary to, spectroscopic follow-ups of SN light echoes. When compared to optical studies of nebular spectra (e.g., Stehle et al., 2005; Tanaka et al., 2011; Ashall et al., 2016; Wilk et al., 2018), X-rays offer an advantage: as the plasma is optically thin, this allows to circumvent the intricacies of radiative transfer. The archival data of the *XMM-Newton*, *Chandra* and *Suzaku* telescopes make it possible to fit the X-ray spectra of Ia SNRs and determine elemental abundances, whose neutron-rich mass ratios (Badenes et al., 2008a; Park et al., 2013; Yamaguchi et al., 2015; Martínez-Rodríguez et al., 2017, see Section I.3.2) can be reconciled with SN Ia explosion models (Bravo et al., 2019) in order to gain knowledge about their progenitors.

I.5 THESIS OUTLINE

My PhD thesis aims to compare observational results from the X-ray spectra of Type Ia SNRs with theoretical models of SNe Ia in order to better understand the nature of SN Ia

progenitors. My dissertation is organized as follows. In Chapter II (Martínez-Rodríguez et al., 2016), I calculate the increase in the neutron excess during carbon simmering in SN Ia progenitors near the Chandrasekhar mass by means of the `MESA` stellar evolution code. In Chapter III (Martínez-Rodríguez et al., 2017), I combine SN Ia nucleosynthesis models with measurements of Ca/S mass ratios in the X-ray spectra of Type Ia SNRs to probe the neutron-rich material in SN Ia ejecta. In Chapter IV (Martínez-Rodríguez et al., 2018), I run hydrodynamical models of expanding Type Ia SNRs in uniform ambient media by means of the one-dimensional `ChN` code, use these to generate synthetic X-ray spectra, and reconcile the bulk properties derived from these models with real observations. These three papers have been published in The Astrophysical journal (ApJ). Finally, in Chapter V, I summarize my work and outline future research projects that can be derived from my thesis.

II NEUTRONIZATION DURING CARBON SIMMERING IN TYPE IA SUPERNOVA PROGENITORS

Martínez-Rodríguez, H., Piro, A. L., Schwab, J., & Badenes, C. 2016, ApJ, 825, 57

II.1 INTRODUCTION

Type Ia supernovae (SNe Ia) are the thermonuclear explosions of white dwarf (WD) stars (Maoz et al., 2014). They play a key role in galactic chemical enrichment through Fe-peak elements (Iwamoto et al., 1999), as cosmological probes to investigate dark energy (Riess et al., 1998; Perlmutter et al., 1999) and constrain ΛCDM parameters (Betoule et al., 2014; Rest et al., 2014), and as sites of cosmic ray acceleration along with other SN types (Maoz et al., 2014). However, the exact nature of their progenitor systems remains mysterious. While it is clear that the exploding star must be a C/O WD in a binary system (Bloom et al., 2012), decades of intensive observational and theoretical work have failed to establish whether the binary companion is a non-degenerate star (the so-called single degenerate, or SD, scenario), another WD (double degenerate, DD – see Wang & Han 2012; Maoz et al. 2014 for recent reviews), or some combination of scenarios. Both cases result in the explosion of a relatively massive WD after one or potentially many more mass accretion episodes, but there are key differences between them. In the SD scenario, the accretion happens over relatively long timescales ($\sim 10^6$ yr, Hachisu et al., 1996; Han & Podsiadlowski, 2004) until the mass of the WD gets close to the Chandrasekhar limit ($M_{\rm Ch} = 1.45(2Y_e)^2 \approx 1.39\,M_\odot$, where Y_e is the mean number of electrons per baryon, Nomoto et al. 1984; Thielemann et al. 1986; Hachisu et al. 1996; Han & Podsiadlowski 2004; Sim et al. 2010). In the DD

scenario, the explosion is the result of the violent interaction or merging of two WDs on a dynamical timescale (Iben & Tutukov, 1984), and the mass of the exploding object is not expected to be directly tied to $M_{\rm Ch}$ (Sim et al., 2010; van Kerkwijk et al., 2010). Attempts to discriminate between SD and DD systems based on these differences have had varying degrees of success. On the one hand, it is known that WDs in the Milky Way merge at a rate comparable to SN Ia explosions (Badenes & Maoz, 2012), and statistical studies of the ejecta and ^{56}Ni mass distribution of SN Ia indicate that a significant fraction of them are not near-Chandrasekhar events (Piro et al., 2014; Scalzo et al., 2014). On the other hand, the large amount of neutron-rich material found in solar abundances (Seitenzahl et al., 2013a) and in some supernova remnants (SNRs) believed to be of Type Ia origin (Yamaguchi et al., 2015) seems to require burning at high densities, which indicates that at least *a non-negligible fraction* of SNe Ia explode close to $M_{\rm Ch}$.

Here we focus on the role that these neutron-rich isotopes play as probes of SN Ia explosion physics and progenitor evolution channels. In particular, we explore the effect of carbon simmering, a process wherein slowly accreting near-$M_{\rm Ch}$ WDs develop a large convective core due to energy input from ^{12}C fusion on timescales of $\sim 10^3 - 10^4$ yr before the onset of explosive burning (Woosley et al., 2004; Wunsch & Woosley, 2004; Piro & Chang, 2008). Previous studies (Chamulak et al., 2008; Piro & Bildsten, 2008) have pointed out that weak nuclear reactions during this phase enhance the level of neutronization in the fuel that will be later consumed in the different regimes of explosive nucleosynthesis. Here, we perform detailed models of slowly accreting WDs with the stellar evolution code `MESA` (Paxton et al., 2011, 2013, 2015), paying close attention to the impact of carbon simmering on the neutron excess.

This paper is organized as follows. In Section II.2, we provide an overview of the main processes contributing to neutronization in SNe Ia, and the importance of understanding these processes in the context of observational probes of SN Ia explosion physics and the pre-SN evolution of their stellar progenitors. In Section II.3, we outline our simulation scheme and describe our grid of `MESA` models for accreting WDs. In Section II.4, we present the main results obtained from our model grid, and in Section II.5, we summarize our conclusions and suggest directions for future studies.

II.2 NEUTRONIZATION IN TYPE IA SUPERNOVAE

It is commonly accepted that WDs are the end product of most main-sequence stars (see Althaus et al., 2010, and references therein). A typical WD is a $\sim 0.6\,M_\odot$ stellar object made up by a C/O core that encompasses most of its size, surrounded by an thin $\sim 0.01\,M_\odot$ He envelope that, in turn, has a shallower $\sim 10^{-4}\,M_\odot$ H layer on top (Althaus et al., 2010). On the other hand, massive WDs ($M \gtrsim 1.1\,M_\odot$) are believed to have O/Ne cores. Therefore, the composition of the core and the outer layers strongly depends on the characteristics of the initial star (Ritossa et al., 1996). The specific chemical composition of a WD determines its properties, which can vary after the AGB phase, along the cooling track, via important processes such as convection, phase transitions of the core and gravitational settling of the chemical elements (Althaus et al., 2010). For this abundance differentiation the main role is played by ^{22}Ne (García-Berro et al., 2008; Althaus et al., 2010) because its neutron excess makes it sink towards the interior as the WD cools. The released gravitational energy by this process influences both the cooling times of WDs (Deloye & Bildsten, 2002) and the properties of SNe Ia (Bravo et al., 2010).

A critical parameter that controls the synthesis of neutron-rich isotopes in SN Ia explosions is the neutron excess

$$\eta \;=\; 1 - 2Y_e \;=\; \sum_i \frac{N_i - Z_i}{A_i}\, X_i\,, \tag{1}$$

where N_i, A_i and Z_i are the neutron number, the nucleon number and charge of species i with mass fraction X_i, respectively. The starting value of η in the SN Ia progenitor is set by its metallicity. This works as follows. Stars with zero-age main-sequence masses $> 1.3\,M_\odot$ burn hydrogen through the CNO cycle (Thielemann et al., 1986). The slowest step is $^{14}\mathrm{N}(\mathrm{p},\gamma)^{15}\mathrm{O}$, which causes all the C, N and O present in the plasma to pile up at ^{14}N. Subsequently, during the hydrostatic He burning, ^{14}N converts to the neutron-enriched isotope ^{22}Ne through the reaction chain $^{14}\mathrm{N}(\alpha,\gamma)^{18}\mathrm{F}(\beta^+,\nu_\mathrm{e})^{18}\mathrm{O}(\alpha,\gamma)^{22}\mathrm{Ne}$.

Because all CNO elements are converted to ^{22}Ne during He burning, there is a linear relationship between the metallicity of a main sequence star and the neutron excess in the WD it eventually produces. Indeed, Timmes et al. (2003) found that this process relates

the neutron excess of the WD and its progenitor metallicity via $\eta = 0.101Z$, where Z refers to the mass fraction of CNO elements, resulting in a value for solar metallicity material of $\eta_\odot = 1.4 \times 10^{-3}$. Gravitational settling of ^{22}Ne might enhance the relative neutronization in the core, but only at the expense of shallower material from the outer layers (Piro & Chang, 2008).

II.2.1 Neutron production during carbon simmering

This relation between η and Z can subsequently be modified by carbon simmering (Piro & Bildsten, 2008; Chamulak et al., 2008), and we summarize the main features of this process in Figure 5. Carbon ignition in the core of a WD takes places through the channels $^{12}\mathrm{C}(^{12}\mathrm{C}, \alpha)^{20}\mathrm{Ne}$ and $^{12}\mathrm{C}(^{12}\mathrm{C}, \mathrm{p})^{23}\mathrm{Na}$ with a branching ratio 0.56/0.44 for $T < 10^9\,\mathrm{K}$ (Caughlan & Fowler, 1988) when the heat from these nuclear reactions surpasses the neutrino cooling. This burning regime (Nomoto et al., 1984), which starts at the gray, dashed line in Figure 5, marks the onset of simmering. The central conditions then trace out the rising dashed, brown line as the star heats and decreases slightly in density. At the same time, a convective region grows outward (Woosley et al., 2004; Wunsch & Woosley, 2004), shown at four different epochs with thick, solid lines. This convection encompasses $\sim 1\,M_\odot$ during a period of $\sim 10^3 - 10^4\,\mathrm{yr}$ before the final thermonuclear runaway at a central temperature of $T_c \approx 8 \times 10^8\,\mathrm{K}$ and the explosion as a Type Ia SN (Piro & Chang, 2008).

During carbon simmering, the protons produced by the $^{12}\mathrm{C}(^{12}\mathrm{C}, \mathrm{p})^{23}\mathrm{Na}$ reaction capture onto ^{12}C, producing ^{13}N. Subsequently, the electron-capture reactions $^{13}\mathrm{N}(\mathrm{e}^-, \nu_\mathrm{e})^{13}\mathrm{C}$ (discussed in detail in Section 2.2 of Chamulak et al., 2008) and $^{23}\mathrm{Na}(\mathrm{e}^-, \nu_\mathrm{e})^{23}\mathrm{Ne}$ (Chamulak et al., 2008; Piro & Bildsten, 2008) produce an enhancement in the neutronization of the core. These reactions consume the products of carbon fusion, so the increase in η is directly related to the amount of carbon consumed prior to the explosion. This proceeds until sufficiently high temperatures or low densities are reached such that timescale for the ^{23}Na electron captures becomes longer than the heating timescale. (The location where these timescales are equal is shown as a magenta, dashed line in Figure 5.) Additionally, as we find here, ^{23}Ne carried into lower density regions of the convection zone can be converted

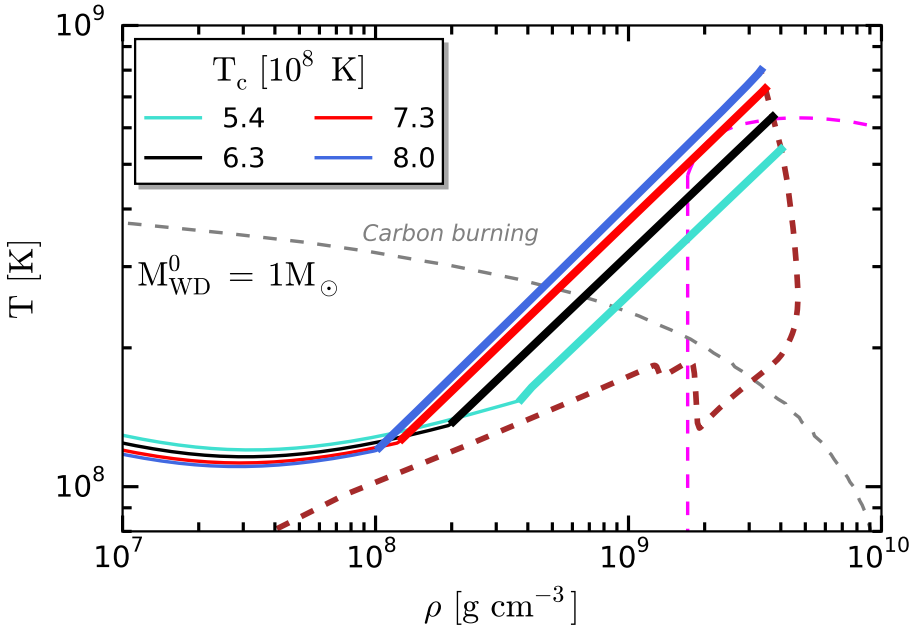

Figure 5: Temperature versus density profiles taken from our fiducial model (Section II.4.1), presented analogously to Figure 1 from Piro & Bildsten (2008). Each profile represents a snapshot in time as the central temperature increases and the convective region grows. The convective region of each profile is represented with thick lines. The dashed, brown line tracks the central density and temperature over time, showing how the central density decreases as the central temperature increases during simmering. The two sharp drops at $\log(\rho_c/\gamma\,\mathrm{cm}^{-3}) \approx 9.1 - 9.2$ correspond to neutrino losses in the ^{23}Na–^{23}Ne and ^{25}Mg–^{25}Na Urca shells, as explained in Section II.2.2 and shown in Figure 6. The dashed, magenta line shows where the heating timescale and ^{23}Na electron-capture timescale are equal; at lower densities/higher temperatures, electron captures on ^{23}Na are frozen out. The dashed, gray line is an approximate C-ignition curve from `MESA` that considers a 100% carbon composition in the core.

back to ^{23}Na by beta decay. These nuclear processes determine the final composition and properties of the ejected material (Iwamoto et al., 1999) and are crucial to obtain synthetic spectra (Brachwitz et al., 2000).

Using these basic arguments, Piro & Bildsten (2008) semi-analytically calculated the amount of carbon consumed during simmering to estimate that the increase in the neutron excess should be $\Delta\eta \sim 10^{-3}$ with an upper bound of $0.93\,\eta_\odot$ known as the "simmering limit". Such a floor to the neutron excess is important to identify because it should be present in any SN Ia progenitor that went through a simmering phase, regardless of how low the progenitor's metallicity is. Using a more detailed nuclear network, but only focusing on the central conditions of the convective zone, Chamulak et al. (2008) predicted a decrement in the mean number of electrons per baryon of $|\Delta Y_e| = 2.7 - 6.3 \times 10^{-4}$, which corresponds to $\Delta\eta \approx 5.4 - 13 \times 10^{-4}$. Although both these works found similar levels of neutronization, they also made strong simplifications, and this is an important motivation for revisiting these results here.

II.2.2 Urca-process cooling

Weak reactions can also affect the thermal state of the WD. An Urca pair consists of two nuclei (Z, A) and $(Z-1, A)$ that are connected by electron-capture $(Z, A) + e^- \rightarrow (Z - 1, A) + \nu_e$ and beta-decay $(Z-1, A) \rightarrow (Z, A) + e^- + \bar{\nu}_e$. Below a threshold density $\rho_{\rm th}$ the beta-decay reaction is favored and above it the electron-capture reaction is favored. Near this threshold density, both reactions occur at a significant rate, and since each produces a neutrino that then free-streams from the star, this has the net effect of cooling the plasma (Gamow & Schoenberg, 1941).

As the WD is compressed, its density increases above the threshold density of numerous Urca pairs. For the compositions and densities of our WD models, the two most important Urca pairs are ^{25}Mg–^{25}Na (with $\log(\rho_{\rm th}/\gamma\,{\rm cm}^{-3}) \approx 9.1$) and ^{23}Na–^{23}Ne (with $\log(\rho_{\rm th}/\gamma\,{\rm cm}^{-3}) \approx 9.2$) (Iben, 1978). These threshold densities are below the density at which carbon ignition occurs, and hence in the central parts of the WD *this local Urca-process cooling occurs before the simmering phase begins.* This effect was discussed in the

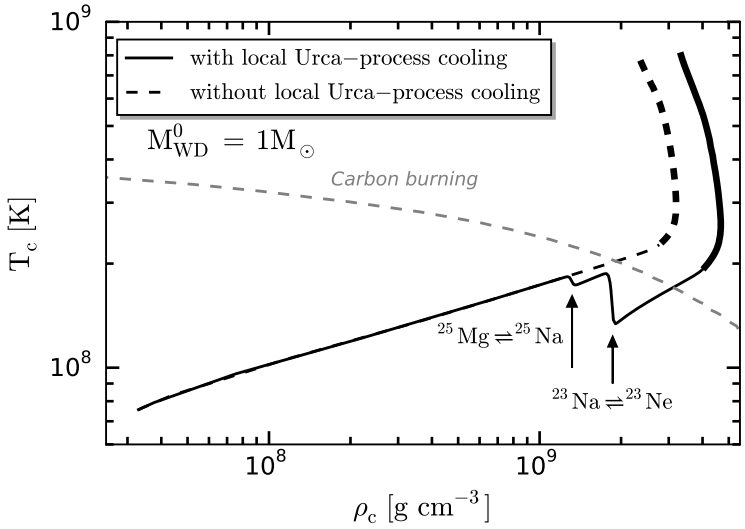

Figure 6: A comparison of the evolutionary tracks for the central density and temperature in our fiducial model (Section II.4.1) with (black line) and without (dashed line) the effects of the ^{23}Na–^{23}Ne and ^{25}Mg–^{25}Na Urca pairs (see Section II.2.2). The evolution during the simmering phase is denoted with thick lines. The gray, dashed line is an approximate C-ignition curve from `MESA` that considers a 100% carbon composition in the core.

context of accreting C/O cores by Paczyński (1973), but is often not included in progenitor models.[1] We make use of new capabilities of `MESA` that allow these processes to be easily included (Paxton et al., 2015). As shown in Figure 6, additional cooling shifts the point at which carbon ignition occurs to higher densities. The specific energy loss rate due to Urca-process neutrinos scales $\propto T^4$ (Tsuruta & Cameron, 1970), so this effect is most pronounced in hotter WDs (those with short cooling ages).

After carbon ignition occurs and the simmering phase begins, the Urca process continues to operate as convection mixes material from regions where it has electron-captured into regions where it will beta-decay and vice-versa. This *convective* Urca process and its effects have been an object of considerable study (e.g., Paczyński, 1972; Bruenn, 1973; Shaviv &

[1]This effect was included in a recent study by Denissenkov et al. (2015), who used a large nuclear network that incorporated new weak rate tabulations from Toki et al. (2013).

Regev, 1977; Barkat & Wheeler, 1990; Lesaffre et al., 2005). We allow for the operation of the convective Urca process in our MESA models, inasmuch as we incorporate appropriate weak rates and allow composition to mix throughout the convective zone. However, limitations imposed by the temporal and spatial averaging that enter into a formulation of 1D mixing-length theory do not allow us to self-consistently treat the effects of the Urca process on the convection itself. In some of our models, in particular those with the solar or super-solar metallicities and hence the highest abundances of ^{25}Mg and ^{23}Na, we observe that, when the convective zone first reaches the Urca shell, it splits in two and remains split for the remainder of the calculation. It seems likely this behavior is a manifestation of these limitations, so when we report our results in Tables 8-10, we mark these models with the note "Convection zone splits during simmering". The development of a model able to fully incorporate the interaction of convection and the Urca process is beyond the scope of this work and will likely require multi-dimensional hydrodynamics simulations (e.g., Stein & Wheeler, 2006). Given the existing uncertainties, Denissenkov et al. (2015) explored the possible effects of the convective Urca process in MESA models by employing a series of mixing assumptions, such as limiting the mass of the convective core to the mass coordinate of the ^{23}Na–^{23}Ne Urca shell. Future work could employ a similar approach to explore the potential effects of the convective Urca process on neutronization.

II.3 WHITE DWARF MODELS

Motivated by the discussion above, we next explore the impact of the neutron-rich isotopes at WD formation and during carbon simmering using MESA[2] (Paxton et al., 2011, 2013, 2015). We create WDs with five different metallicities: $Z/Z_\odot = 0.01, 0.10, 0.33, 1.00, 2.79$[3], where $Z_\odot = 0.014$ (Asplund et al., 2009). In each case, we start from $4.5 M_\odot$ ZAMS-models by using the inlists from the suite case `make_co_wd`, which makes a protostar go through the MS until the AGB thermal pulses and then reveals its C/O core. These models are stopped when

[2] http://mesa.sourceforge.net/index.html

[3] Our intention was to create a $3Z_\odot$ star. However, MESA presents several convergence problems for this high metallicity during the AGB phase and a $2.79Z_\odot$ WD was created instead.

the total luminosity reaches $\log L/L_\odot = -0.5$. MESA presents convergence problems due to the unstable He shell burning on accreting WDs (Shen & Bildsten, 2009), so we artificially remove the H/He shallower envelope via a negative accretion rate. The resulting WDs have $\log L/L_\odot \approx -1.4$. Then, we rescale the initial masses of our WDs to 0.70, 0.85 and $1.00 M_\odot$ without changing the chemical composition as a function of the Lagrangian mass coordinate.

To evaluate the effect of cooling times in the properties of WDs (Lesaffre et al., 2006; Althaus et al., 2010), we let our stars cool for 1 and 10 Gyr, ages that are consistent with the spread for the delay-time distribution (DTD) of SNe Ia ($\sim$40 Myr–10 Gyr, Maoz et al., 2012, 2014). We do not account for residual heating by the external H/He envelope (Althaus et al., 2010), as this material has already been removed in our models. We also do not include the effects of diffusion, sedimentation, or crystallization, as the development of MESA's treatment of these processes is ongoing. With these caveats in mind, we classify our WDs as "hot" (no cooling applied), "warm" (1 Gyr) and "cold" (10 Gyr).

We use these 45 WDs (five metallicities, three masses, and three cooling ages) as an input for our simmering MESA inlists, based on the suite case `wd_ignite`, which models the accretion in the Type Ia SNe SD channel by considering a C/O WD, a uniform, pure C/O accretion and a stopping condition such that the total luminosity from the nuclear reactions reaches $10^8\,L_\odot$. We use a nuclear network consisting of 48 isotopes, shown in Table 2, and the reactions linking them. This is the main difference between the present study and the one performed by Chen et al. (2014), who also examined the properties of accreting C/O WDs, but used a more limited network. We use a version of MESA based on release 7624, but modified to incorporate a rate for the $^{13}\mathrm{N}(\mathrm{e}^-,\,\nu_\mathrm{e})^{13}\mathrm{C}$ reaction that is appropriate for the high density conditions of a WD interior. We motivate and describe our modifications in Appendix A.1.

For the accreted material, we consider uniform accretion with three different rates, 10^{-6}, 10^{-7} and $5\times10^{-8}\,M_\odot\,\mathrm{yr}^{-1}$, which yield accretion ages $\sim 10^6$ yr that agree with the literature (Hachisu et al., 1996; Han & Podsiadlowski, 2004). The chemical abundances of the accretion are set equal to the initial surface composition of each WD. This makes a total of 135 different models whose results are presented in Section II.4.2. In order to achieve a higher spatial and temporal resolution during the Urca-process cooling and carbon simmering phases, we

Table 2: Nuclear network used in our calculations.

Isotope	A	Isotope	A
n	1	O	14–18
H	1–2	F	17–19
He	3–4	Ne	18–24
Li	7	Na	21–25
Be	7	Mg	23–26
Be	9–10	Al	25–27
B	8	Si	27–28
C	12–13	P	30–31
N	13–15	S	31–32

stop our accreting models when the WD mass reaches 1.3 $M_{\odot}$, which corresponds to central densities below the Urca cooling densities discussed in Section II.2.2. We then continue the models with controls that incorporate timestep limits based on the the variation of the central density and temperature. To confirm that our models are converged, we perform runs with increased temporal and spatial resolution. To corroborate that our results are insensitive to the treatment of the outer boundary of the central convection zone, we execute a run with overshooting. We verify that the quantities of interest are unchanged and refer the reader to Appendix A.2 for more detailed information.

For the stopping condition of our inlists, we choose the one derived by Woosley et al. (2004), and broadly discussed in Chamulak et al. (2008), Piro & Bildsten (2008) and Piro & Chang (2008), which estimates that simmering should end when dynamical burning is triggered. This requires $T_{\rm c} \approx 8 \times 10^8\,{\rm K}$, i.e., $\log(T_{\rm c}/{\rm K}) \approx 8.9$. In turn, Piro & Bildsten (2008) argued that the final thermonuclear runaway should ensue when the heating time scale $t_h = c_{\rm p} T_{\rm c}/\epsilon$ (where $c_{\rm p}$ is the specific heat of the liquid ions) gets comparable to the

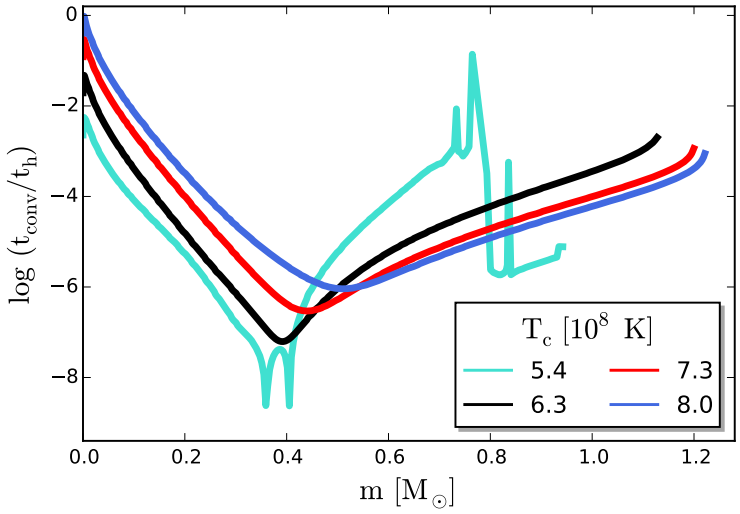

Figure 7: Profiles of the ratio between the convective and the heating time scales versus the Lagrangian mass in the growing convective region for our fiducial model (Section II.4.1). The convective overturn timescale $t_{\rm conv}$ gets comparable to t_h at the center of the WD right before the final thermonuclear runaway as shown by the blue curve. Various nuclear reactions with rates λ should freeze out when $t_h < \lambda^{-1}$.

dynamical time scale $t_{\rm dyn} \equiv (G\rho_{\rm c})^{-1/2} \sim 1\,{\rm s}$. Our conclusion is that, in general, $t_h \gtrsim 10 t_{\rm dyn}$ when $T_{\rm c} \approx 8 \times 10^8\,{\rm K}$, so that $t_h \sim t_{\rm dyn}$ does not hold. Figure 7 shows that simmering ends when the heating time scale approaches the convective time scale $t_h \leq t_{\rm conv}$ in the core of the WD (Piro & Chang, 2008). Here, $t_{\rm conv} = \min\{H_p, R_{\rm conv}\}/v_{\rm conv}$, where $v_{\rm conv}$ is the convective velocity, $R_{\rm conv}$ the extent of the convective zone and H_p the pressure scale height, which `MESA` calculates as $H_p = \min\{P/(g\rho), \sqrt{P/G}/\rho\}$.

II.4 RESULTS

We next summarize the main results of our survey of simmering WD models. We begin in Section II.4.1 by focusing on a fiducial model, a 1 $M_\odot$, solar-metallicity WD with an

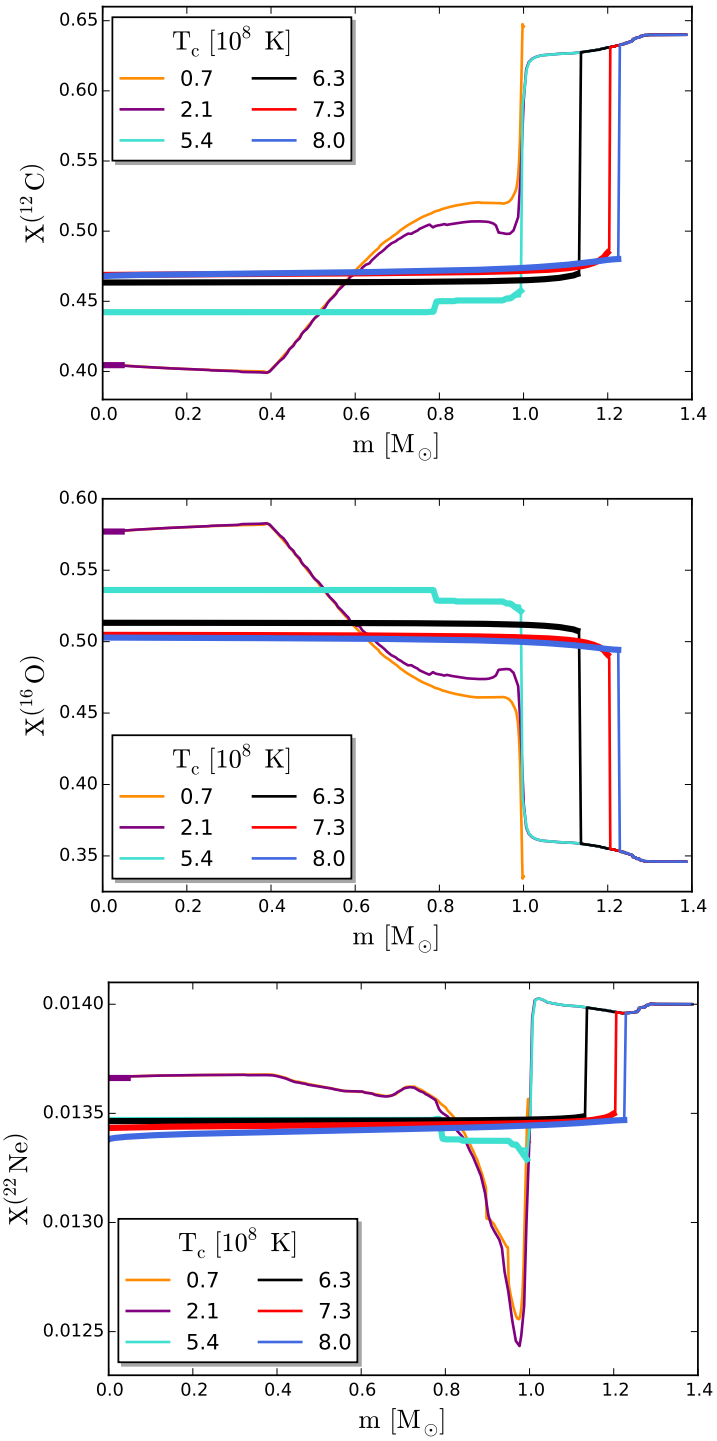

Figure 8: Abundance profiles of ^{12}C (top), ^{16}O (middle) and ^{22}Ne (bottom) in our fiducial model. The orange curve represents the initial model, while the purple one corresponds to the onset of carbon simmering. The convective region of each profile is depicted with thick lines.

accretion rate of $10^{-7}\,M_{\odot}\,\mathrm{yr}^{-1}$. This is used to compare and contrast with our large grid of models in Section II.4.2.

II.4.1 Fiducial model

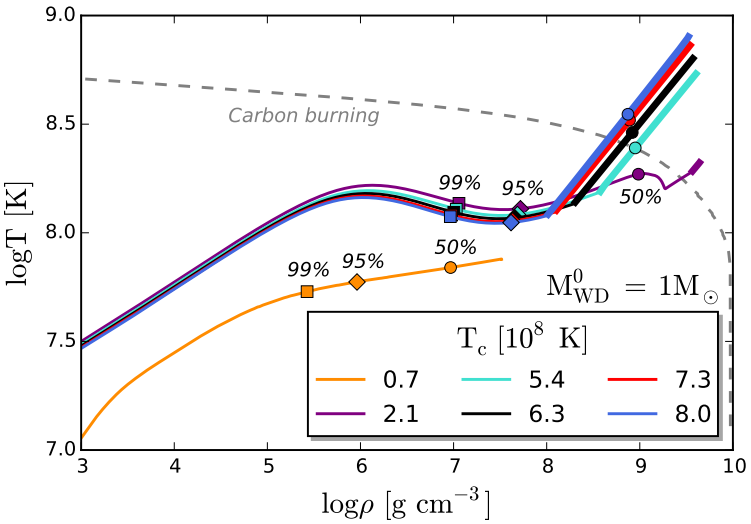

Figure 9: Temperature versus density profiles during several stages of the stellar evolution in our fiducial model. The color legend is the same as the one of Figure 8, whereas the gray, dashed line is an approximate C-ignition curve from `MESA` that considers a 100% carbon composition in the core, which is why the purple profile does not exactly match it. Finally, some points encompassing fractions of the stellar mass are depicted along each of the curves.

In Figure 8, we show the evolution of the chemical profiles of ^{12}C, ^{16}O and ^{22}Ne for our fiducial model during the different stages of the accretion process and through the simmering phase. We have labeled our curves at different time steps with the corresponding central temperature because of our stopping condition (Woosley et al., 2004). After carbon simmering, all the chemical profiles become homogeneous within the convective core (shown by the thick, fairly flat regions of the profiles). In turn, the accreted material eventually gets mixed into the core when the edge of this convective region reaches the initial mass of the star, which is why the carbon fraction increases at the center (carbon-rich material is mixed in rate higher than the consumption by carbon burning). The last profiles show a

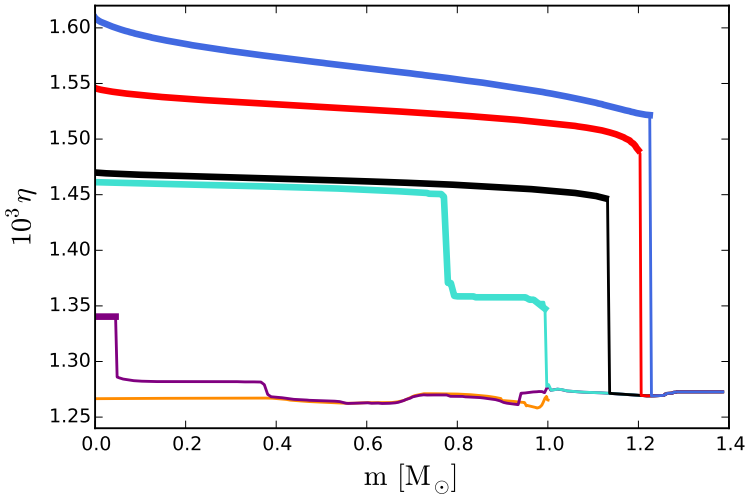

Figure 10: Neutron excess profiles as a function of the Lagrangian mass for the same series of snapshots as shown in Figure 8.

clear distinction between convection, which encompasses $\approx 90\%$ of the star by mass, and the outer, non-convective regions of the WD.

Figure 9 shows the $\log T - \log \rho$ profiles for the fiducial model. Initially, the hot, accreted material increases the effective temperature of the WD, while the interior of the star remains unchanged. After $\sim 10^{3-4}$ years, the temperature gradient steepens due to the energy lost via neutrinos ($\propto T^3$, Chen et al., 2014), so that a temperature inversion arises in the outer regions of the WD. This is critical because, for high accretion rates and cold WDs, the outer layers will be hotter than the core and off-center ignitions might take place (Chen et al., 2014). Finally, there is a change in the thermal structure of the star after the onset of simmering. Since convection is very efficient in the core given the high thermal conduction timescale $\sim 10^6$ yr, the convective profile is nearly an adiabat (Piro, 2008).

Figure 10 shows the neutron excess as a function of depth. This starts relatively constant with depth at a value of $\eta \approx 1.25 - 1.3 \times 10^{-3}$ set by the progenitor metallicity. Then, as the simmering proceeds, a region with an increased neutron excess is seen to grow out in mass. At the onset of thermonuclear runaway, the central neutron excess is enhanced by an amount

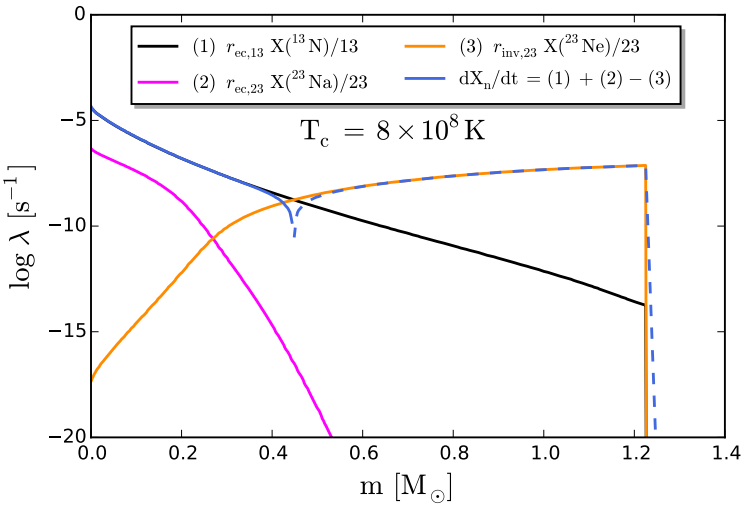

Figure 11: Profile of the variation of the neutron fraction dX_n/dt for $T_c = 8 \times 10^8$ K (blue) and the rates λ of the three weak reactions involved. The dashed line indicates the region where it is negative. The black and the magenta lines refer to, respectively, the electron capture reactions ^{13}N(e$^-$,ν_e)^{13}C and ^{23}Na(e$^-$,ν_e)^{23}Ne. Finally, the orange line is the beta decay ^{23}Ne(ν_e,e$^-$)^{23}Na whose dominance in the outer, lower-density regions explains why the increase in the neutron excess is smaller than the one predicted by Piro & Bildsten (2008) and Chamulak et al. (2008).

$\approx 3 \times 10^{-4}$, so that Y_e is reduced by $\approx 1.5 \times 10^{-4}$. This is smaller than the decrement within the convective zone at the center $|\Delta Y_e| = 2.7 - 6.3 \times 10^{-4}$ predicted by Chamulak et al. (2008), as well as than the maximum neutronization estimate $|\Delta Y_e| \approx 6 \times 10^{-4}$ calculated by Piro & Bildsten (2008). The reason for this discrepancy is that we have resolved the entire convective zone at each time and the range of densities encompassed by it. The electron captures are very sensitive to density, and thus the outer, lower-density regions do not experience the same level of electron captures and corresponding neutronization. This can be appreciated in Figures 11 and 12. As we find here, ^{23}Ne can be converted back to ^{23}Na when it is carried into the portion of the convection zone below the threshold density. In contrast, both Piro & Bildsten (2008) and Chamulak et al. (2008) focused on the

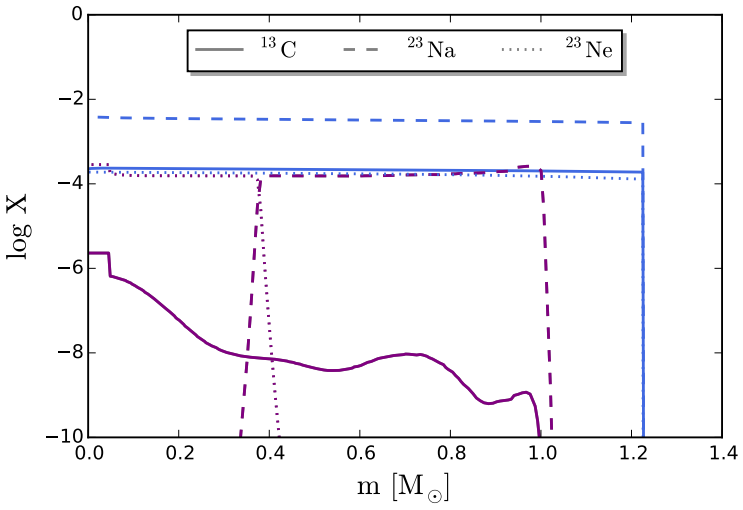

Figure 12: Abundance profiles of ^{13}C, ^{23}Na and ^{23}Ne in our fiducial model at the onset of simmering ($T_c = 2.1\times10^8$ K; purple lines) and the end of our calculation ($T_c = 8\times10^8$ K; blue lines). During simmering, the convection zone is fully mixed, allowing ^{23}Ne to be converted back to ^{23}Na when it is transported below the threshold density.

central, highest-density conditions for deriving rates, and thus overestimated the amount of neutronization.

II.4.2 Cooled models and global results

We next consider more broadly the results of the 135 models of our parameter survey. Figure 13 shows the behavior of the central density and temperature, the growth of the central neutron excess and the evolution of the convective core for the "hot" fiducial model discussed in Section II.4.1, as well as the "warm" and "cold" versions of it. The effect of the Urca-process neutrino cooling disappears as the cooling age of the WD increases and the central temperature of the WD at the electron capture threshold density decreases. The local Urca-process cooling can also be appreciated in the evolutionary track of η_c, where T_c decreases while η_c increases above its initial value $\eta_{c,0}$ (which is mainly determined by the original abundance of ^{22}Ne, as discussed in Section II.2.1). In addition, it decreases around

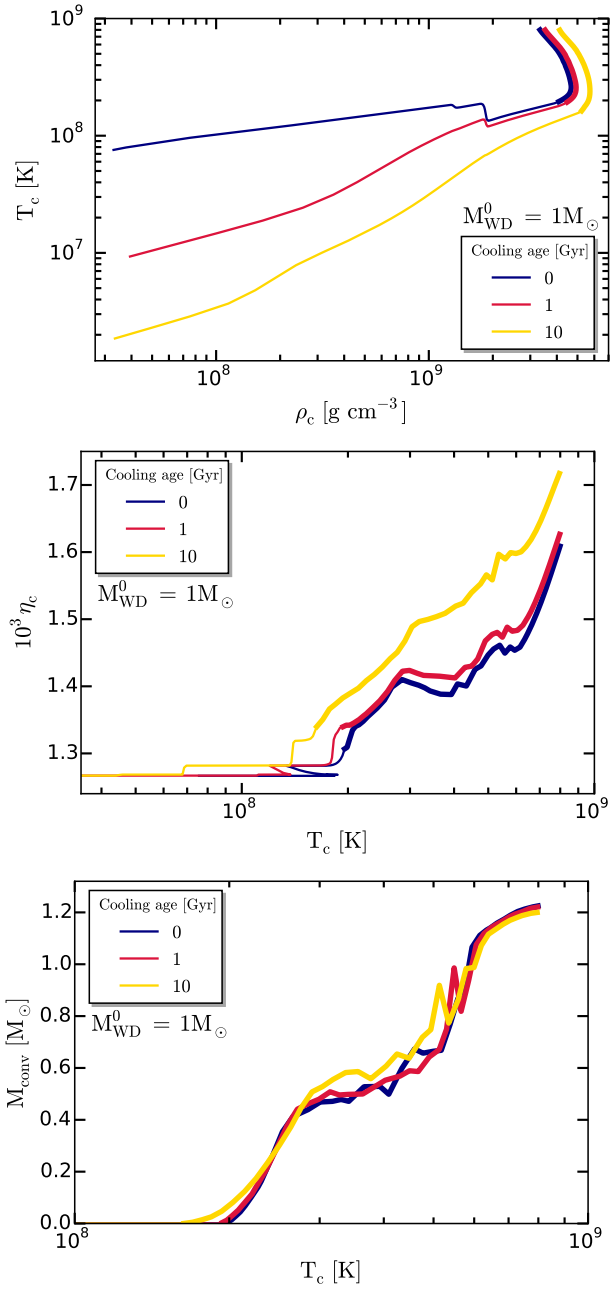

Figure 13: The impact on the simmering of cooling ages equal to 0 Gyr (blue curve), 1 Gyr (red curve), and 10 Gyr (yellow curve). In each case, the simmering region is represented with thick lines. The top panel shows the evolution of the central temperature and the central density of a 1 $M_\odot$, solar-metallicity star with an accretion rate of $10^{-7}\,M_\odot\,\mathrm{yr}^{-1}$ and different cooling ages. The middle panel plots the evolution of the central neutron excess as a function of the central temperature. The bottom panel summarizes the growth of the mass of the convective core. Notice that the temperature limits are different in this plot.

$T_{\rm c} \approx 3 \times 10^8$ K when the outer edge of the convection zone crosses the ^{23}Na–^{23}Ne Urca shell.

The central neutron excess is slightly larger for the "cold" WD because the electron captures increase for higher densities. The central temperature at the onset of simmering is approximately the same for the three WDs, as well as the final extent of the convective core. At the onset of the thermal runaway, $\rho_{\rm c}$ is the main relic of the cooling process, whereas accretion has "erased" the memory of the initial mass of the WD.

The remainder of our results are summarized in Figures 14, 15, 16, and 17, and in Tables 8, 9 and 10. Note that there are no fast accretors ($\dot{M} = 10^{-6} M_\odot\,{\rm yr}^{-1}$) in the case of the cooled WDs because they lead to off-center ignitions (Chen et al., 2014). In our tabulated results, we indicate these models with the note "Off-center carbon ignition".

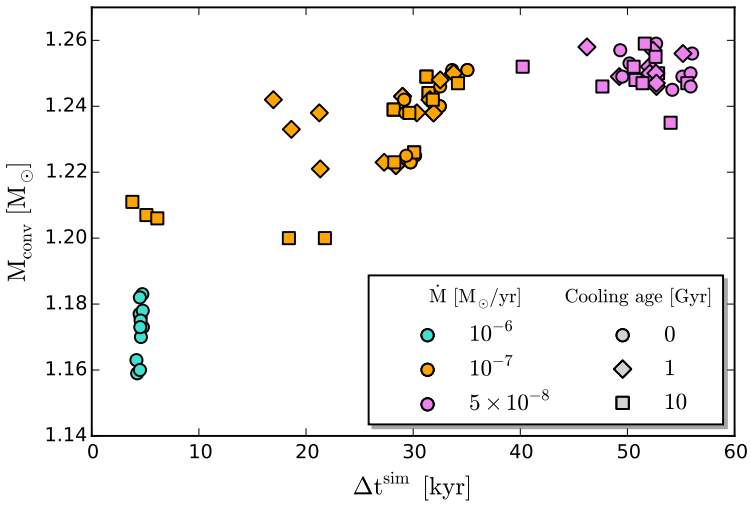

Figure 14: Final mass of the convective core versus elapsed time during carbon simmering. Note that the different initial masses and metallicities are not labeled.

Some of the general trends are as follows. The final masses of the convective core (shown in Figures 14, 15, and 16) have relatively similar values $M_{\rm conv} \approx 1.16 - 1.26\,M_\odot$, encompassing $\approx 85 - 90\%$ of the final stars. This result agrees with the estimates of Piro & Chang (2008). The elapsed times during simmering are longer when the convective core is larger (see Figure 14) and are typically $\gtrsim 10^4$ years. The only models with $\Delta t \sim 10^3$ years are the fast accretors and the "cold" WDs with an initial mass of $1\,M_\odot$. Accretion times for these

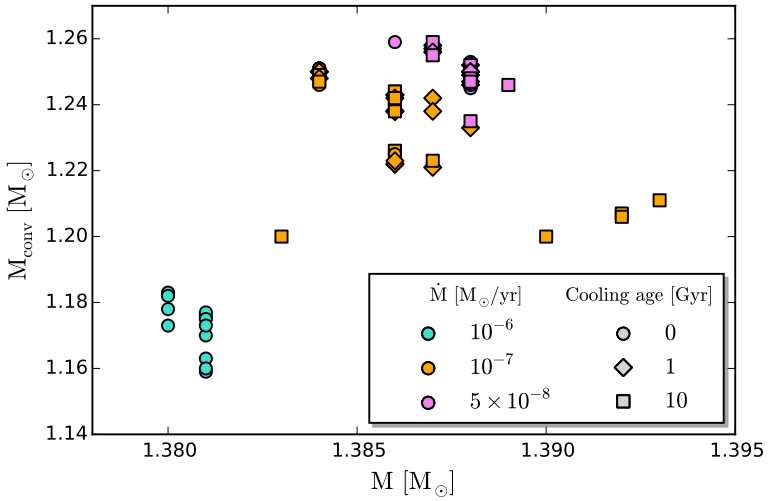

Figure 15: Final mass of the convective core versus final mass.

models are smaller and the shallower heat is unable to get to the core until a long time has elapsed. This, in turn, translates into higher ignition densities and more brief elapsed times during simmering. This is somewhat different from the estimate of $\Delta t \sim 10^3$ years obtained by Piro & Chang (2008), which was based on the central conditions. This work does note that a realistic value for the simmering time depends on the size of the region heated (see Equation (8) of Piro & Chang, 2008, which describes this). The neutron excess increases with higher central densities (see Figure 17) as the electron captures get more favored.

Finally, our results concerning the impact of simmering on the neutronization are summarized in Figure 18, where we plot the expected neutron excess of a SN Ia progenitor versus its initial metallicity. The blue curve shows the linear relationship of $\eta = 0.101Z$ derived by Timmes et al. (2003). The red region shows the range of maximum neutronization estimates, in the range of $0.93\,\eta_\odot$, from Piro & Bildsten (2008) and demonstrates the role played by the simmering floor. Namely, at sufficiently low metallicity, the neutron excess no longer reflects that of the progenitor but instead the amount of neutronization during simmering. Although we do find some small differences between models, Figure 17 demonstrates that the range of

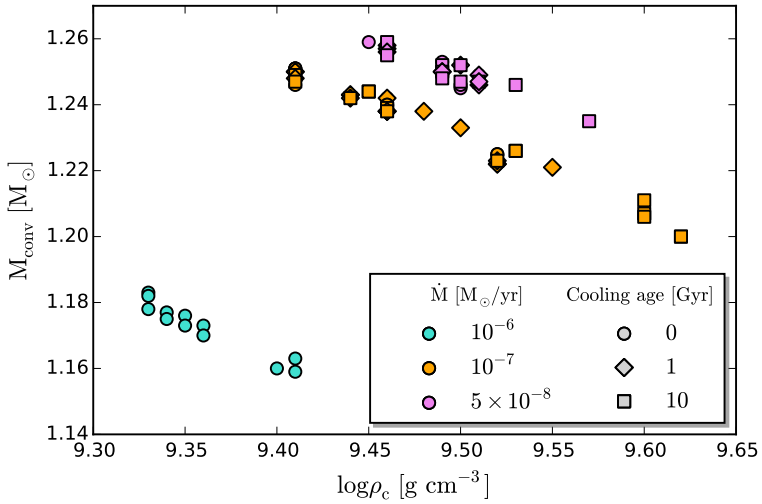

Figure 16: Final mass of the convective core versus final central density.

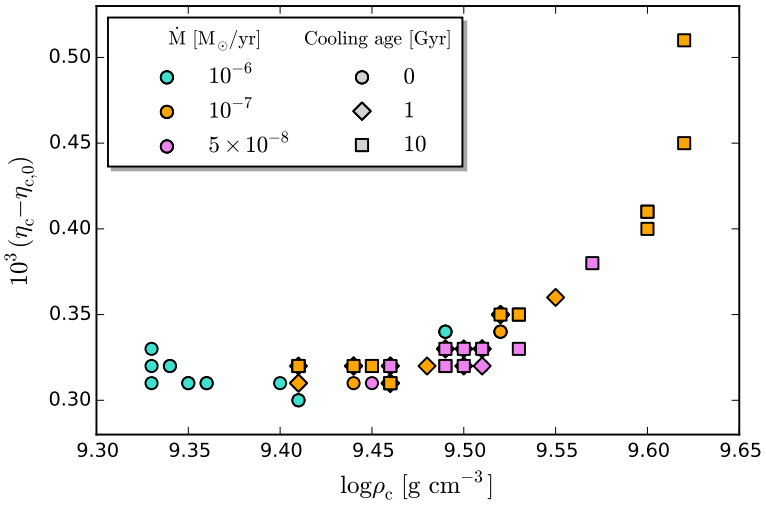

Figure 17: Increase in the central neutron excess versus final central density.

possible neutron excesses is relatively small, and thus we take the fiducial simmering limit to be $0.22\,\eta_\odot$ (yellow, shaded region in Figure 18), well below the value found by Piro & Bildsten (2008) for the reasons outlined in the discussions above.

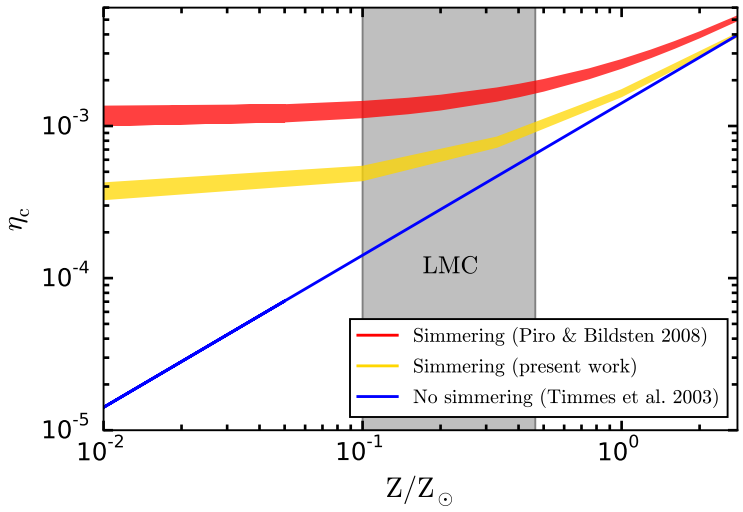

Figure 18: The central neutron excess as a function of the metallicity of SNe Ia progenitors that experience no simmering (blue line), simmering according to Piro & Bildsten (2008) (red region), and simmering according to our work here (yellow region). This highlights the impact of the simmering floor at sufficiently low metallicities. Typical values of Z for the Large Magellanic Cloud (Piatti & Geisler, 2013) are shown as a gray shaded region. Note that we use $Z_\odot = 0.014$ (Asplund et al., 2009).

II.5 CONCLUSIONS

We have performed the first study of carbon simmering in SNe Ia progenitors with numerical models that fully resolve the extent of the convective region and include a complete nuclear network with Urca processes. We find that the final mass of the convective zone in the accreting WD is in the range of $M_{\rm conv} \approx 1.16 - 1.26\,M_\odot$. Our final values for the increase in the central neutron excess $\eta_{\rm c}$ before the onset of thermonuclear runaway are fairly constant at $\approx 3 - 4 \times 10^{-4}$. These values are $\approx 70\%$ lower than those found by previous studies (Piro & Bildsten, 2008; Chamulak et al., 2008), with the difference stemming from our ability to properly resolve the full density profile of the convection zone and determine accurately where and at what rate electron captures occur. As the convection zone grows, it eventually spans

many density scale heights, with electron captures favored in regions above the threshold density and beta decays favored in regions below it. While the convective zone remains fully mixed, the overall neutronization is determined by the mass-weighted average of the reaction rates across the convection zone.

As summarized in Figure 18, the lower simmering floor that we obtain makes it more challenging to find an observational "smoking gun" for the presence of simmering in SN Ia progenitors with metallicities $\gtrsim 1/3\,Z_{\odot}$, typical of the thin disk of the Milky Way (Nordström et al., 2004). The strongest constraints on the degree of neutronization in individual SN Ia progenitors come from the analysis of the X-ray emission from Fe-peak nuclei (Mn, Cr, Fe, and Ni) in Galactic SNRs like Tycho, Kepler and 3C 397 (see Badenes et al., 2008a; Park et al., 2013; Yamaguchi et al., 2015). In the dynamically young SNRs Tycho and Kepler, where the bulk of the shocked Fe-peak elements were synthesized in the explosive Si burning regime (Park et al., 2013), the Mn/Cr mass ratio is a clean tracer of progenitor neutronization. Badenes et al. (2008a) and Park et al. (2013) found a high level of neutronization in these SNRs, which translates to super-solar progenitor metallicities $Z/Z_{\odot} = 3.4^{+3.6}_{-2.6}$ and $Z/Z_{\odot} = 3.6^{+4.6}_{-2.0}$ if the contribution from simmering is neglected. The constraints on the progenitor neutronization in SNR 3C 397 are more model-dependent because this is a dynamically older object, and the shocked ejecta has a large contribution from neutron-rich NSE material. Nevertheless, Yamaguchi et al. (2015) also found that, neglecting the contribution from simmering, Chandrasekhar-mass explosion models for this SNR require very high ($Z/Z_{\odot} \sim 5$) progenitor metallicities. These high levels of neutronization in Galactic Type Ia SNRs seem to be in tension with our results, because simmering is unable to reconcile the observations with a population of progenitors that is typical of the thin disk of the Milky Way, which contains very few stars with $Z/Z_{\odot} \gtrsim 3$. We hope to gain further insight on this apparent mismatch between models and observations by examining Type Ia SNRs in the LMC, which should have progenitor metallicities $\approx 0.1 - 0.4 Z_{\odot}$ (Piatti & Geisler, 2013, see Figure 18), low enough to clearly determine whether their progenitors underwent a carbon simmering phase and constrain the resulting degree of neutronization.

In the future, our models could be used as an input for SNe cosmology and explosion studies, as done by Moriya et al. (2016) and Piro & Morozova (2016), who created models

with MESA and then employed a different code (Morozova et al., 2015) to track the evolution of the supernova light curves. Using our models as inputs for explosive burning calculations would also be helpful for exploring the impact of the centrally neutron-enhanced core on the explosion and the resulting light curve (e.g. Bravo et al., 2010). For example, Townsley et al. (2009) and Jackson et al. (2010) studied the influence of ^{22}Ne on the laminar flame speed, energy release, and nucleosynthesis during the SN explosion. The enhanced neutronization would have a similar impact, and although the influence of the ^{22}Ne was found to be modest in these studies, we also predict spatial differences caused by the presence of the convection zone.

In addition, there are pieces of physics that could be added to our simmering models. As mentioned in Section II.3, the gravitational settling of ^{22}Ne will be implemented in an upcoming MESA release. We expect to revisit these models with a more complete approach including this process, as well as an in-depth treatment of the chemical diffusion and rotation during convection. Piro & Chang (2008) and Piro (2008) initially explored these effects with a series of semi-analytic models, and it will be interesting to revisit them with a more realistic treatment. The properties of the convective zone and neutron excess we found here are fairly homogeneous over a wide range of parameters. Therefore, it will be useful to see if other effects can add more diversity.

We thank the whole MESA community for their unconditional help during the elaboration of this paper, and especially Frank Timmes for useful discussions in regards to the implementation of nuclear reactions in MESA. We also thank Ed Brown and Remco Zegers for helpful communications regarding the ft-values for electron capture on ^{13}N, and Sumit Sarbadhicary for his initial work in the project. Finally, we are grateful to the anonymous referee, Dean Townsley and D. John Hillier for their useful feedback which helped improve the quality of this paper. This work has been funded by NASA ADAP grant NNX15AM03G S01. JS is supported by NSF grant AST-1205732.

III OBSERVATIONAL EVIDENCE FOR HIGH NEUTRONIZATION IN SUPERNOVA REMNANTS: IMPLICATIONS FOR TYPE IA SUPERNOVA PROGENITORS

Martínez-Rodríguez, H., Badenes, C., Yamaguchi, H., et al. 2017, ApJ, 843, 35

III.1 INTRODUCTION

Type Ia supernovae (SNe Ia) are the thermonuclear explosions of white dwarf (WD) stars that are destabilized by mass accretion from a close binary companion. Despite their importance for many fields of astrophysics, such as galactic chemical evolution (Kobayashi et al., 2006; Andrews et al., 2017), studies of dark energy (Riess et al., 1998; Perlmutter et al., 1999) and constraints on ΛCDM parameters (Betoule et al., 2014; Rest et al., 2014), key aspects of SNe Ia remain uncertain, including the precise identity of their stellar progenitors and the mechanism that triggers the thermonuclear runaway. Discussions of SN Ia progenitors are often framed by the single degenerate and double degenerate scenarios, depending on whether the WD companion is a non-degenerate star or another WD. In the single degenerate scenario, the WD grows in mass through accretion over a relatively long timescale ($t \sim 10^6$ year) and explodes when it gets close to the Chandrasekhar limit $M_{Ch} \simeq 1.4\,M_\odot$ (Nomoto et al., 1984; Thielemann et al., 1986; Hachisu et al., 1996; Han & Podsiadlowski, 2004). In most double degenerate scenarios, by contrast, the destabilizing event (a merger or collision) happens on a dynamical timescale (Iben & Tutukov, 1984), quickly leading to an explosion that is not necessarily close to M_{Ch} (Raskin et al., 2009; Rosswog et al., 2009; Raskin et al., 2010; Sim et al., 2010; van Kerkwijk et al., 2010; Kushnir et al., 2013). In principle, it is possible

to discriminate between single degenerate and double degenerate systems exploding on a dynamical timescale after merging, provided that some observational probes are sensitive to the presence or absence of an extended accretion phase leading to the thermonuclear runaway and to the mass of the exploding star (see the recent reviews by Wang & Han 2012 and Maoz et al. 2014). Here we examine one of these probes, the degree of neutronization in SN Ia ejecta.

The neutron excess, defined as $\eta = 1 - 2Y_{\rm e} = 1 - 2\,\langle Z_A \rangle\,/\,\langle A \rangle$ (where $Y_{\rm e}$ is the electron fraction, Z_A is the atomic number, and A is the mass number) should be zero in WDs composed solely of ^{12}C and ^{16}O. The value of η can be increased through weak interactions taking place at different stages during the life of SN Ia progenitors. So far, three such mechanisms have been proposed.

1. **Progenitor metallicity**. The bottleneck reaction in the CNO cycle, ^{14}N(p,γ)^{15}O, causes all the C, N, and O in the progenitor to pile up onto ^{14}N at the end of H burning, which then becomes ^{22}Ne during hydrostatic He burning through the chain ^{14}N(α, γ)^{18}F(β^+, ν_e)^{18}O(α, γ)^{22}Ne. Since ^{22}Ne carries a neutron excess, this results in a linear scaling of η with progenitor metallicity Z: $\eta = 0.1Z$ (Timmes et al., 2003; Bravo et al., 2010; Moreno-Raya et al., 2016). Hence, this ^{22}Ne content is usually defined as the "metallicity" of a WD.
2. **Carbon simmering**. In SN Ia progenitors that approach $\rm M_{Ch}$ through slow accretion, carbon can ignite close to the center without immediately triggering a thermonuclear runaway. Instead, the WD develops a large ($\sim 1\,M_\odot$) convective core for a few thousands of years until the heat from fusion overwhelms neutrino cooling and an explosion ensues (Woosley et al., 2004; Wunsch & Woosley, 2004; Piro & Chang, 2008). During this 'C simmering' phase, electron captures on the products of C fusion (mostly ^{13}N and ^{23}Na) increase the value of η (Chamulak et al., 2008; Piro & Bildsten, 2008; Martínez-Rodríguez et al., 2016).
3. **Neutron-rich Nuclear Statistical Equilibrium** (n-NSE). When a WD explodes close to $\rm M_{Ch}$, the inner $\sim 0.2\,M_\odot$ is dense enough for electron captures to take place during nucleosynthesis, shifting the equilibrium point of NSE away from ^{56}Ni to more neutron-rich species like ^{55}Mn and ^{58}Ni (Iwamoto et al., 1999; Brachwitz et al., 2000).

To summarize, the baseline neutronization level in all SNe Ia is set by progenitor metallicity. Additional neutronization can be introduced only in systems that explode close to M_{Ch}, by C simmering or n-NSE. C simmering will affect most of the SN ejecta, while n-NSE will only affect the NSE material synthesized in the innermost layers (i.e., Fe-peak elements). Thus, while mixing may blur this distinction to some degree, accurate measurements of η in SNe have the potential to constrain the fundamental properties of SN Ia progenitors.

Emission lines from stable Mn and Ni in the X-ray spectra of Type Ia supernova remnants (SNRs) have been used to measure η and infer the properties of SN Ia progenitors (Badenes et al., 2008a; Park et al., 2013; Yamaguchi et al., 2015). However, these weak lines are often hard to detect, and it is difficult to disentangle the neutronization effects of n-NSE and C simmering using Fe-peak nuclei (see Park et al., 2013; Yamaguchi et al., 2015, for discussions). Here, we report on a new method to measure neutronization in SNe Ia based on the sensitivity of the Ca/S yield to η identified by De et al. (2014). ^{40}Ca and ^{32}S are produced in a quasi-nuclear statistical equilibrium in a temperature range $\simeq 2{-}4{\times}10^9$ K. In this regime, the nuclear abundances are determined by a set of coupled Saha equations that ultimately depend on the temperature, density, and Y_e (e.g. Clifford & Tayler, 1965; Hartmann et al., 1985; Nadyozhin & Yudin, 2004; Seitenzahl et al., 2008; De et al., 2014). Thus, the abundances of symmetric nuclei such as ^{32}S and ^{40}Ca depend on the overall Y_e. For explosive events such as SNe Ia, the freeze-out from high temperatures occurs on a time scale faster than the nuclear rearrangement, ensuring that the abundances produced at these temperatures are the same as the final abundances (De et al., 2014; Miles et al., 2016). Among the intermediate-mass elements, ^{40}Ca is the most sensitive to changes in the electron fraction. De et al. (2014) found a systematic quasi-linear ^{32}S yield with respect to Y_e, and a more complex trend for the global abundance of ^{40}Ca. Thus, more neutron-rich progenitors should have a lower Ca/S mass ratio (M_{Ca}/M_S). Here we show that the Ca/S mass ratio in SN Ia ejecta is indeed a good observational tracer of neutronization, with the key advantages that (a) it is not affected by n-NSE and (b) it uses much stronger emission lines that can be easily measured in a larger sample of objects.

This paper is organized as follows. In Section III.2, we describe the observations and derive M_{Ca}/M_S values. In Section III.3, we interpret the inferred M_{Ca}/M_S and discuss the

implications for SN Ia physics. In Section III.4, we analyze the relation between M_{Ca}/M_S and the $^{12}C+^{16}O$ reaction rate. Finally, in Section III.5, we summarize our results and outline future lines of work.

III.2 OBSERVATIONS AND DATA ANALYSIS

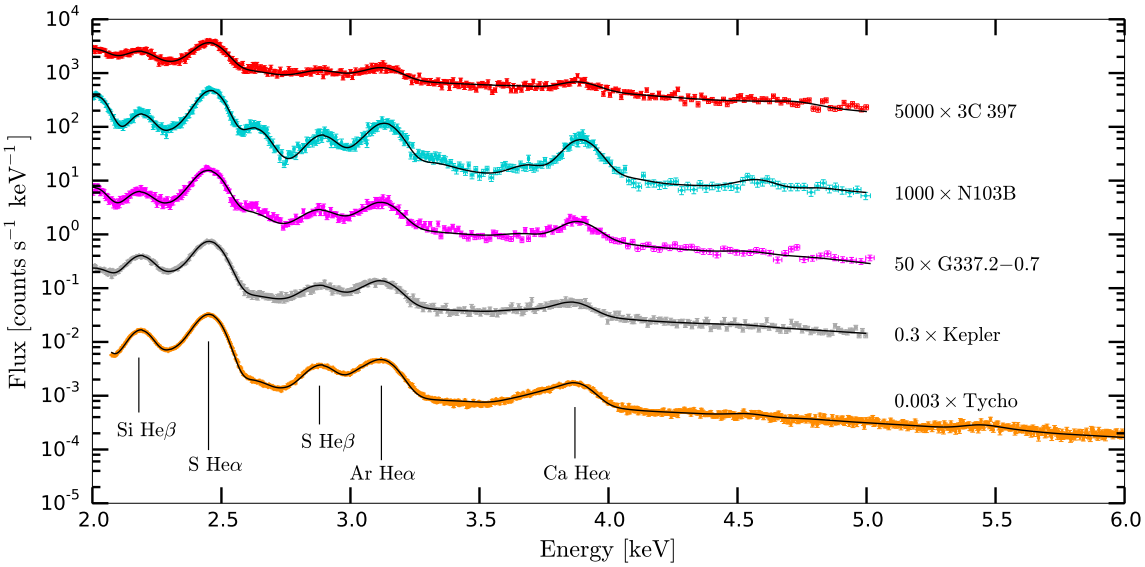

Figure 19: *Suzaku* XIS0 and XIS3 combined spectra of 3C 397, N103B, G337.2−0.7, Kepler and Tycho between 2.0 and 5.0 keV. The SNRs are sorted in decreasing order of Fe ionization state (Yamaguchi et al., 2014a). The most relevant atomic transitions are labeled. For Tycho, it is necessary to extend the upper energy limit from 5.0 to 6.0 keV in order to achieve a reduced chi-square $\chi^2/\nu < 2$.

Yamaguchi et al. (2014a) list 11 Type Ia SNRs with Fe Kα emission in the Milky Way and the Large Magellanic Cloud (LMC). We re-reduce and analyze all these *Suzaku* spectra, paying special attention to the emission lines from S, Ar, Ca, Cr, Mn, Fe, and Ni. We do not include Si in our analysis because of the well-known calibration problems around $\sim$1.5 keV in the *Suzaku* CCDs (https://heasarc.gsfc.nasa.gov/docs/suzaku/analysis/sical.html).

Table 3: Summary of the *Suzaku* spectral modeling for the SNRs shown in Figure 19. See Table 1 from Yamaguchi et al. (2014a) for a list of the observation IDs and dates corresponding to each SNR.

SNR	Exp. Time (ks)	$N_{\rm H}$ (10^{22} cm^{-2})	Continuum Model	Refs.[a]	M_{Ar}/M_S[b]	M_{Ca}/M_S[b]	M_{Cr}/M_{Fe}[b]
3C 397	104	3.00	Bremms. ($kT = 0.16$ keV[c])	1	$0.214^{+0.030}_{-0.026}$	$0.213^{+0.021}_{-0.034}$	$0.040^{+0.029}_{-0.016}$
N103B	224	0.34	Power law ($\Gamma = 3.70$)	2,3	$0.257^{+0.024}_{-0.035}$	$0.255^{+0.021}_{-0.036}$	$0.028^{+0.021}_{-0.014}$
G337.2−0.7	304	3.20	Power law ($\Gamma = 2.20$)	4	$0.214^{+0.016}_{-0.013}$	$0.169^{+0.016}_{-0.023}$	Undeterm.
Kepler	146	0.52	Power law ($\Gamma = 2.67$)	5,6,7	$0.279^{+0.010}_{-0.017}$	$0.283^{+0.016}_{-0.023}$	$0.008^{+0.007}_{-0.005}$
Tycho	313	0.60	Power law ($\Gamma = 2.54$)	8	$0.218^{+0.022}_{-0.010}$	$0.252^{+0.025}_{-0.011}$	$0.016^{+0.018}_{-0.005}$

[a]References consulted for the absorption and continuum components in the spectral fittings: (1) Safi-Harb et al. (2005), (2) Lewis et al. (2003), (3) Someya et al. (2014), (4) Rakowski et al. (2006), (5) Reynolds et al. (2007), (6) Patnaude et al. (2012), (7) Park et al. (2013), (8) Badenes et al. (2006).

[b]All the uncertainties are in the 90% confidence range ($\Delta\chi^2 = 2.706$). Note that the confidence intervals do not necessarily have to be symmetric (`https://heasarc.gsfc.nasa.gov/xanadu/xspec/manual/XSerror.html`).

[c]Best-fit parameter.

We merge the data from the two active front-illuminated CCDs (XIS0 and 3) to increase photon counts. The spectrum of each SNR is fit in the 2.0−5.0 keV energy range with a plane-parallel shock model (vvpshock, Borkowski et al., 2001) plus an additional component for the continuum (either bremsstrahlung or a power law), using the `XSPEC` software (Arnaud, 1996, version 12.9.0i, `https://heasarc.gsfc.nasa.gov/xanadu/xspec/manual/`) and the most recent non-equilibrium ionization atomic data from *AtomDB* (Foster et al., 2012, 2014). We fix the hydrogen column densities $N_{\rm H}$ and the continuum components to values previously reported for each SNR (see references in Table 3). We let the electron temperature T_e, the ionization time scale $n_e t$ (defined as the product of the electron density and the expansion age) and the abundances of the α-elements in the shock model vary until we get a valid fit, with a reduced chi-square $\chi^2/\nu < 2$ (where ν is the number of degrees of freedom). This allows us to derive confidence intervals for the different parameters. We convert these abundances retrieved by the best-fit spectral model into mass ratios using the Anders & Grevesse (1989) factors.

Our goal is to measure Ca/S mass ratios to better than $\sim$20% in order to compare with a grid of SN explosion models (where physically meaningful variations of $\rm M_{Ca}/M_S$ are of this order or larger). Only the five objects shown in Figure 19 pass this quality cut: 3C 397, G337.2−0.7, Kepler and Tycho in the Milky Way, and N103B in the LMC. The relevant parameters for the observations are listed in Table 3. Additionally, we determine Ar/S mass ratios for these SNRs.

As a sanity check, we also fit all spectra using two single-ionization timescale non-equilibrium ionization models (vvrnei, Hughes et al., 2000), and find mass ratios consistent with the values obtained with the plane-parallel shock models. For Tycho, we are unable to get a valid fit with a plane-parallel shock model, so we use two non-equilibrium ionization models in an enlarged energy window between 2.0 and 6.0 keV (See Figure 19). Only this spectral model can successfully fit the Ca Heα feature (see Badenes et al., 2006, for a discussion about this line in the spectrum of Tycho and the difficulties to reproduce it with explosion models). We follow the same procedure around the Fe Kα line (5.0−8.0 keV) for each SNR, but can confidently detect the Mn and Ni lines only for 3C 397, Kepler and Tycho (measurements reported in Yamaguchi et al., 2015), so we choose to determine the Cr/Fe

mass ratio (M_{Cr}/M_{Fe}) for all objects as a baseline measurement of Fe-peak ejecta.

The final Ar/S, Ca/S and Cr/Fe mass ratios are listed in Table 3. The relative errors in the inferred M_{Ca}/M_S are in the range of $\sim$5$-$16%, which allows for meaningful comparisons with explosion models. These are lower than the previous Fe-peak relative errors for 3C 397, Kepler and Tycho: $\sim$35$-$70% (M_{Mn}/M_{Cr}) and $\sim$28$-$65% (M_{Mn}/M_{Fe}, M_{Ni}/M_{Fe}). Hence, the mass ratios of intermediate-mass elements can be measured with better precision than those of Fe-peak elements. Prior measurements of M_{Ca}/M_S in the optical spectra of SNe Ia are based on tomography (e.g. 0.299 for SN 2002bo, Stehle et al. 2005; 0.029 for SN 2003du, Tanaka et al. 2011; between $0.250^{+0.088}_{-0.088}$ and $0.40^{+0.14}_{-0.14}$ for SN 1986G, Ashall et al. 2016), and strongly depend on the radiative transfer treatment and on the chosen explosion model. The error bars from these tomography estimates are either undetermined or higher ($\sim$35%) than our measured errors. It is worth mentioning that all these measurements, with the exception of SN 2003du, overlap the ones reported in this paper (see Figure 23).

Before doing a direct comparison between models and SNR observations, we must distinguish between dynamically old objects like 3C 397 and G337.2$-$0.7, which have likely thermalized the entire SN ejecta (Rakowski et al., 2006; Yamaguchi et al., 2015), and dynamically young objects like Kepler and Tycho, which probably have not (Badenes et al., 2006; Patnaude et al., 2012), with N103B being a transitional object between the two classes (Lewis et al., 2003; Williams et al., 2014). The X-ray spectra of dynamically young objects are only representative of the shocked material, not of the entire SN ejecta, and comparisons to bulk yields from SN explosion models should be done with some caution. However, the diagnostic Ca/S mass ratios in Kepler and Tycho are largely unaffected by this, since the vast majority of the explosive Si-burning material has already been shocked in these two objects (Badenes et al., 2006; Patnaude et al., 2012).

The M_{Ca}/M_S values measured in our SNRs span the range between 0.17 and 0.28. N103B has $M_{Ca}/M_S \approx 0.26$, between Tycho (0.25) and Kepler (0.28). This alone makes it challenging to invoke progenitor metallicity as the only source of neutronization in SN ejecta (e.g., Timmes et al., 2003), unless Kepler's progenitor was more metal-poor than most LMC stars, which seems unlikely given its measured Fe-peak mass ratios (Park et al., 2013) and location toward the Galactic center region. Therefore, our observations alone, without any compari-

son to models, indicate that progenitor metallicity is not the only source of neutronization in SN Ia progenitors.

III.3 INTERPRETATION

III.3.1 Comparison with explosion models

To interpret our measured mass ratios, we use the spherically symmetric SN Ia explosion models introduced in Yamaguchi et al. (2015), which are calculated with a version of the code described in Bravo & Martínez-Pinedo (2012), updated to account for an accurate coupling between hydrodynamics and nuclear reactions (Bravo et al., 2016). In this model grid, the M_{Ch} explosions are delayed detonations (Khokhlov, 1991) with a central density $\rho_c = 2\times10^9\,\mathrm{g\,cm^{-3}}$ and different deflagration-to-detonation densities (ρ_{DDT}): 3.9, 2.6, 1.3 and $1.0\times10^7\,\mathrm{g\,cm^{-3}}$, labeled as DDTa, DDTc, DDTe, and DDTf (see Badenes et al., 2003, 2005, 2008b). The sub-M_{Ch} models are central detonations of CO WDs with a core temperature $T_c = 10^8\,\mathrm{K}$ and masses $M_{WD} = 0.88, 0.97, 1.06$ and $1.15\,M_\odot$, similar to the models by Sim et al. (2010). Each model in the grid is calculated with five different values of the progenitor metallicity, $Z = 0.02, 0.18, 0.71, 1.8$ and $5.4\,Z_\odot$, taking $Z_\odot = 0.014$ (Asplund et al., 2009). This progenitor neutronization is set by increasing the abundance of ^{22}Ne in the pre-explosion WD according to the Timmes et al. (2003) metallicity relation. Additional neutronization from C simmering in M_{Ch} models with large convective cores ($\sim1\,M_\odot$) should behave in a similar way, i.e., increasing the value of η throughout the convective region of the pre-explosion WD (Martínez-Rodríguez et al., 2016). However, for simplicity, we have not included a separate enhancement of η due to simmering in this model grid. Because no simmering is included in our models, the level of neutronization in intermediate-mass elements is controlled exclusively by progenitor metallicity. The value of η in the inner $\sim0.2\,M_\odot$ of ejecta in the M_{Ch} models is further modified by n-NSE nucleosynthesis during the explosion (Iwamoto et al., 1999; Brachwitz et al., 2000). Although simplified, this model grid captures the basic phenomenology of neutronization in SN Ia progenitors.

The bulk Cr/Fe vs. Ca/S mass ratios in the models are shown in Figure 20, together with the values measured in the five SNRs in our sample. As expected from De et al. (2014), the Ca/S mass ratio in the models is a good tracer of progenitor neutronization (see also Figure 21). Models with different metallicities that burn Ca and S at similar temperatures have M_{Ca}/M_S values that can be discriminated by observations. This is because the main contribution to both elements comes from the isotopes ^{40}Ca and ^{32}S, whose abundances are in quasi-statistical equilibrium at the temperatures ($\simeq 4{\times}10^9$ K) at which ^{40}Ca is synthesized. In this regime, $M_{Ca}/M_S \propto X_\alpha^2$, where X_α is the abundance of alpha particles, which decreases as metallicity increases (see Figures 2 and 8 in Bravo, 2013). The DDT models with the lowest ρ_{DDT} (DDTe and f), which correspond to the low luminosity end of SNe Ia, show lower Ca/S mass ratios because they burn a larger mass of Ca at a lower density and temperature than their more energetic counterparts, which results in a lower Ca/S mass ratio. Figure 21 shows that, for a given metallicity, the M_{Ch} and sub-M_{Ch} models predict similar M_{Ca}/M_S values.

It is worth noting that the models in our grid span the observed Ca/S and Cr/Fe mass ratios for all the SNRs. Furthermore, the level of neutronization inferred from the closest equivalent progenitor metallicity (Z_{eq}) is rather high in all SNRs. When compared to the metallicity distribution functions (MDFs) in the Milky Way and the LMC (see Figure 22 and Section III.3.2), this suggests an additional source of neutronization in SN Ia ejecta. One possibility is carbon simmering. To quantify the increase in Z_{eq}, we need to consider some additional information about the objects under study. The properties of the Fe Kα emission analyzed by Yamaguchi et al. (2014a) rule out the M_{Ch} models with the lowest ρ_{DDT} (DDTe and f) for N103B, 3C 397, Kepler, and Tycho, and favor them for G337.2−0.7. These constraints are confirmed by detailed spectral modeling for Tycho, G337.2−0.7 and Kepler (Badenes et al., 2006; Rakowski et al., 2006; Patnaude et al., 2012), and by the light echo spectrum of Tycho (Krause et al., 2008). Once the ruled out M_{Ch} models are removed, we can better constrain the Z_{eq} values for each SNR from the Ca/S mass ratio: 5.4 $Z_\odot$ for 3C 397 and G337.2−0.7, 1.8 $Z_\odot$ for Tycho and N103B, and between 1.8 and 0.7 $Z_\odot$ for Kepler. These values are roughly the same for sub-M_{Ch} explosions, although the Cr/Fe mass ratio can rule out these models for 3C 397 (see also Yamaguchi et al., 2015). We note

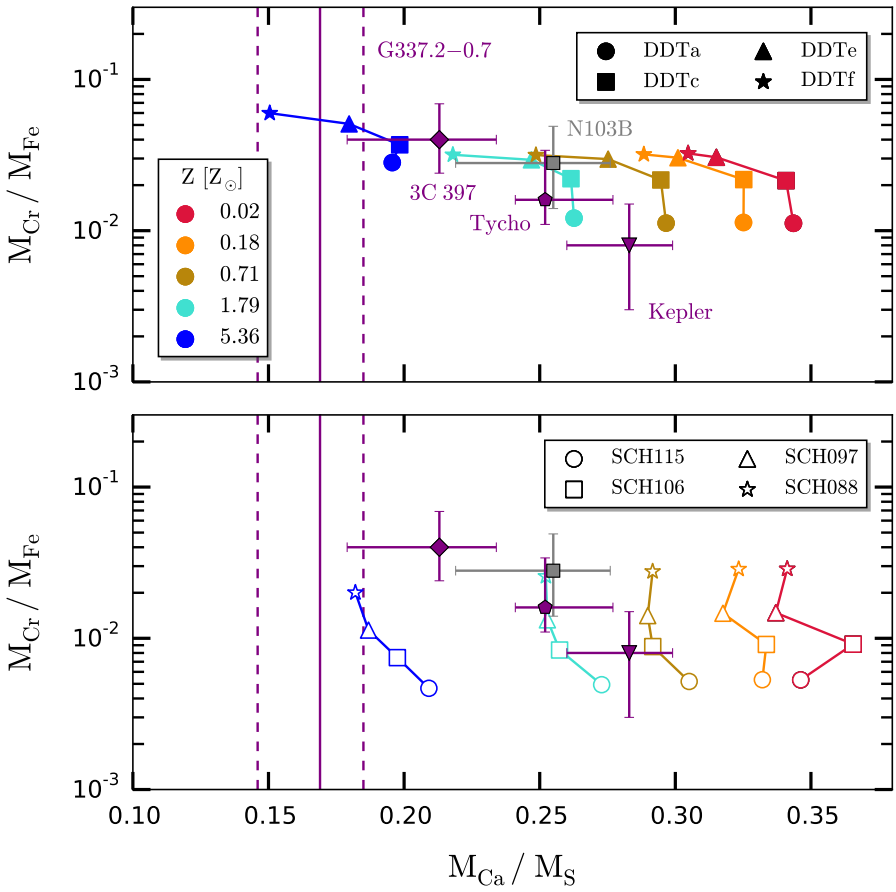

Figure 20: M_{Cr}/M_{Fe} vs. M_{Ca}/M_S for 3C 397, N103B, Kepler and Tycho (Table 3), compared with the theoretical predictions from SN Ia models (see Section III.3.1). The purple, vertical lines correspond to M_{Ca}/M_S for G337.2−0.7, whose M_{Cr}/M_{Fe} could not be determined. Top: M_{Ch} models. Bottom: sub-M_{Ch} models.

that Vink (2016) proposed a sub-M_{Ch} progenitor for Kepler based on the properties of its light curve, and our measured M_{Cr}/M_{Fe} is in good accordance with the sub-M_{Ch} models in our grid. These Z_{eq} results are in agreement with previous analyses based on emission lines from Fe-peak elements in Tycho, Kepler, and 3C 397 (Badenes et al., 2008a; Park et al., 2013; Yamaguchi et al., 2015), but they represent a much cleaner measurement of the pre-explosion neutronization in the progenitor, since the Ca/S mass ratio is not susceptible to

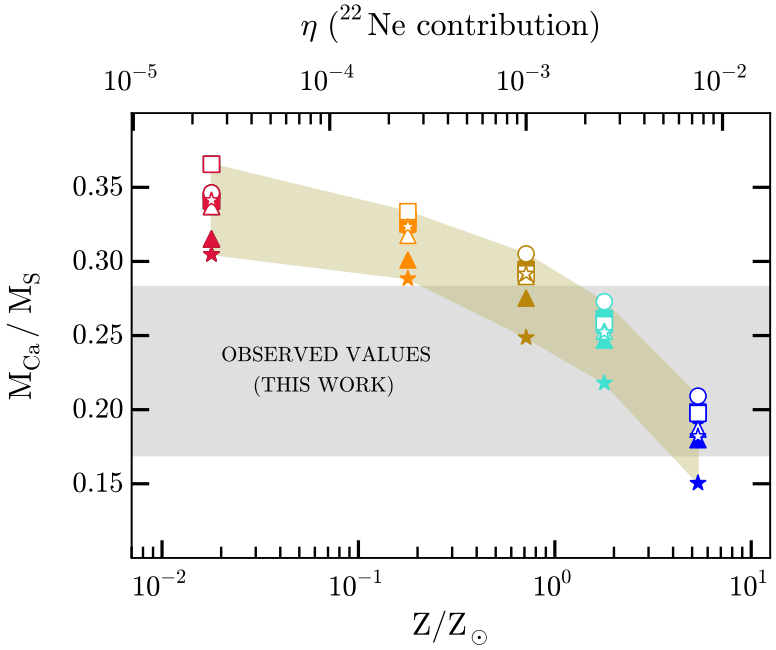

Figure 21: M_{Ca}/M_S vs. progenitor metallicity for the models depicted in Figure 20. Our measured mass ratios are shown as a gray, shaded strip, and the khaki region covers the theoretical predictions from the models. The neutron excess η is given above the panel. Here, $\eta = 0.1Z$, showing the ^{22}Ne contribution to the overall neutronization (Timmes et al., 2003), because our models do not include the effect of C simmering (Section III.3.1) and M_{Ca}/M_S is not affected by n-NSE (Section III.1). More neutron-rich progenitors have a lower M_{Ca}/M_S.

contamination from n-NSE material synthesized in the deepest layers of the WD (see Park et al., 2013, for a discussion).

III.3.2 Comparison with metallicity distribution functions

The significance of the high values of Z_{eq} that we infer from the X-ray spectra becomes apparent when we compare them to the MDFs of the underlying stellar populations. This is shown in Figure 22, where we take the MDF as a function of Galactocentric radius for

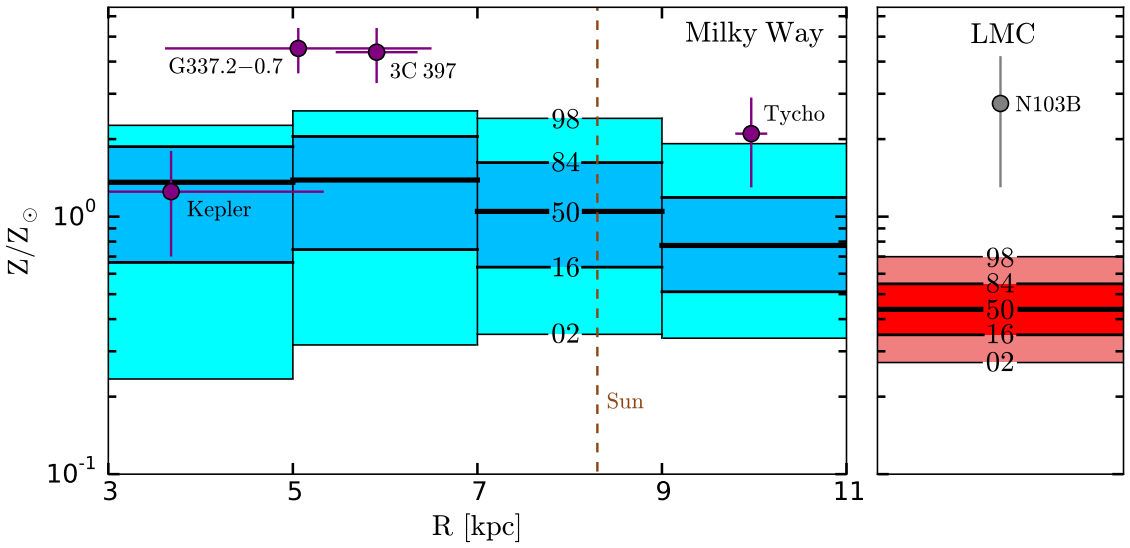

Figure 22: Comparison between the implied metallicities of the SNRs and the stellar metallicity distributions (numbers indicate percentiles) for the Milky Way (as a function of Galactocentric radius) and LMC disks. We consider a maximum height over the Milky Way disk $|z| = 0.6$ kpc, which encompasses the four Galactic SNRs. The solar Galactocentric distance (8.3 kpc; Gillessen et al., 2009) is shown as a dashed, brown line.

the Milky Way disk (Hayden et al., 2015) and the bulk MDF of the LMC (adapted from Choudhury et al., 2016). The Galactocentric radii of the Milky Way SNRs are calculated from their Galactic coordinates and the most recent estimates for their distances from the solar system: 6.5−9.5 kpc to 3C 397 (Leahy & Ranasinghe, 2016), 2.0−9.3 kpc to G337.2−0.7 (Rakowski et al., 2006), 3.0−6.4 kpc to Kepler (Reynoso & Goss, 1999; Sankrit et al., 2005) and 2.5−3.0 kpc to Tycho (Tian & Leahy, 2011). We linearly interpolate between our DDT models (upper panel of Figure 20) to find an approximate Z_{eq} range for each SNR, excluding the models that can be ruled out based on the Fe Kα emission. We note that the Z_{eq} values are similar in M_{Ch} and sub-M_{Ch} explosions (see Section III.3.1).

Our analysis indicates that progenitor metallicity can be ruled out as the only source of neutronization in 3C 397, G337.2−0.7, and N103B, which are many standard deviations

above the mean stellar metallicity of their environments in the Galaxy and the LMC (see Figure 22). Tycho is a $\sim 2\sigma$ outlier, and Kepler is the only object whose neutronization is compatible with the stellar metallicity distribution in its Galactic environment.

III.4 SENSITIVITY OF M_{CA}/M_S TO THE $^{12}C+^{16}O$ REACTION RATE

Because a grid of SN Ia explosion models is needed to translate our measured Ca/S mass ratios into equivalent progenitor metallicities, it is important to verify the sensitivity of this ratio to the details of explosive nucleosynthesis calculations. To this end, we compare our observed M_{Ca}/M_S to the predictions of six M_{Ch} (Iwamoto et al., 1999; Travaglio et al., 2004; Maeda et al., 2010; Travaglio et al., 2011; Blondin et al., 2013; Seitenzahl et al., 2013b) and two sub-M_{Ch} (Woosley & Weaver, 1994; Woosley & Kasen, 2011) SN Ia explosion model grids from the literature. Figure 23 shows that the multi-dimensional models, Travaglio et al. (2004, 2D and 3D), Maeda et al. (2010, 2D), Travaglio et al. (2011, 2D) and Seitenzahl et al. (2013b, 3D) predict a Ca/S mass ratio that is substantially ($\sim 50\%$) lower than both the models in our grid and the observations, unlike the spherically symmetric calculations in 1D (Woosley & Weaver, 1994; Iwamoto et al., 1999; Woosley & Kasen, 2011; Blondin et al., 2013).

Though there are likely additional differences due to the methods used in these computations, we identify the $^{12}C+^{16}O$ reaction rate as a significant source of the spread seen in Figure 23. A precise determination of the cross-section for this reaction remains elusive. This is largely because the cross-section at stellar energies is in a non-resonance region, where the cross-section is determined by the interference between several broad resonances. In addition, high energy tails of subthreshold levels whose properties are challenging to determine directly can also complicate the extrapolation of the data into the Gamow range (e.g., Bucher et al., 2015; Fang et al., 2017). At temperatures $\simeq 4\times10^9$ K, where the $^{12}C+^{16}O$ rate is most influent, the Gamow peak of this reaction is 7.7 ± 1.9 MeV. This rate impacts the Ca/S yield because of its relation with the abundance of alpha particles, $M_{Ca}/M_S \propto X_\alpha^2$.

Given these theoretical uncertainties, the reaction was not included in the model grid

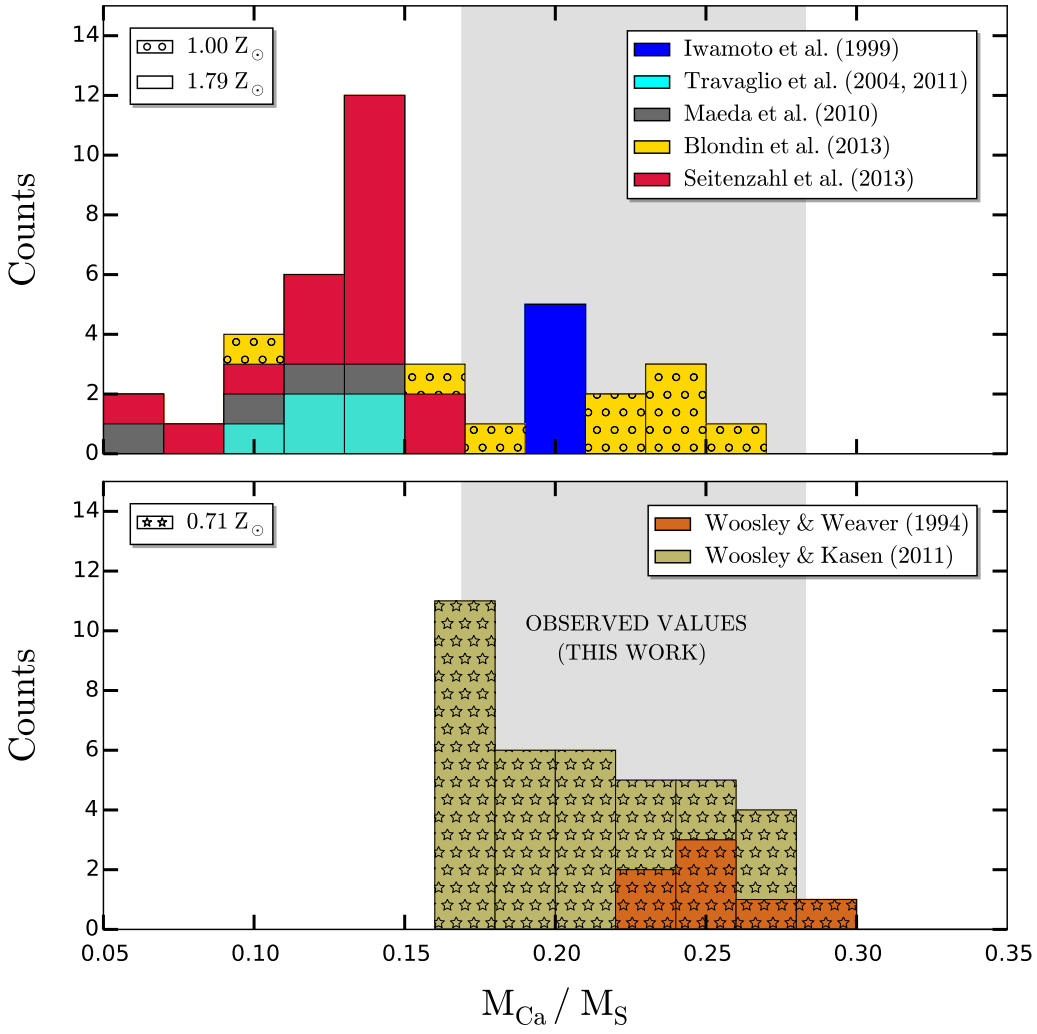

Figure 23: Histogram for the Ca/S mass ratio predicted by various model grids from the literature. Top: M_{Ch} models. Bottom: sub-M_{Ch} models. Our measured values are depicted as a gray, shaded region.

from Yamaguchi et al. (2015) shown in Figures 20 and 21. However, the results from that paper, which are based on the Fe-peak elements (M_{Ni}/M_{Fe}, M_{Mn}/M_{Fe}), remain valid. To prove this, we run an additional DDTc, 5.4-$Z_{\odot}$ model where the reaction is included (using the rate given by Caughlan & Fowler 1988) and show the effect on the total mass yields in Figure 24. The Fe-peak yields are insensitive to the $^{12}C+^{16}O$ rate, but the Ca and S yields

vary drastically. This could affect our inferred Z_{eq} values given the small error bars in our measurements (see Section III.2).

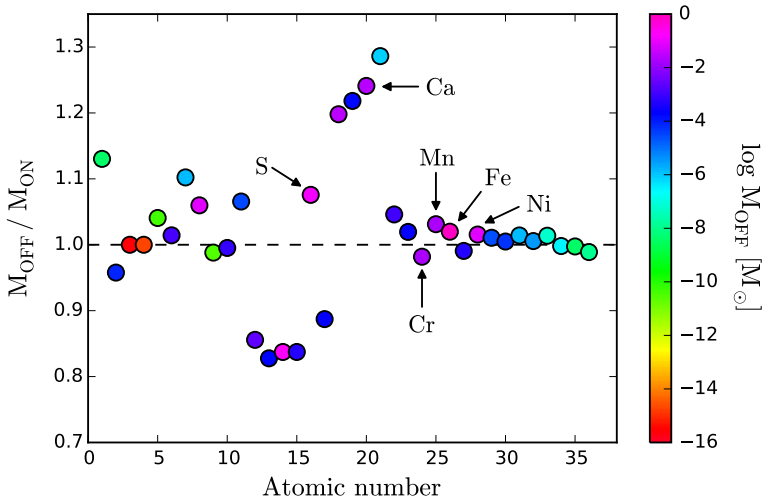

Figure 24: Total yields spanning from hydrogen ($Z_A = 1$) to krypton ($Z_A = 36$) for two DDTc, 5.4-$Z_\odot$ models. The vertical axis depicts the mass ratios of a model where the $^{12}C + ^{16}O$ reaction is fully suppressed, denoted by "off", and a model where the rate given by Caughlan & Fowler (1988) is considered, denoted by "on". The intermediate-mass elements show significant sensitivity to this rate, unlike the Fe-peak elements. The individual points are colored based on their mass abundances when the reaction is not included.

To study the effect of this reaction rate on the overall M_{Ca}/M_S yield, we run additional M_{Ch} and sub-M_{Ch} models. The M_{Ch} are calculated analogously to the ones in Section III.3.1, although with an increased central density $\rho_c = 3 \times 10^9\,g\,cm^{-3}$. The sub-$M_{Ch}$ are obtained with the methods used in Miles et al. (2016) and described in Townsley et al. (2016), applied in one dimension, and using the reaction networks provided by the Modules for Experiments in Stellar Astrophysics (`MESA`) for post-processing instead of `Torch` (Townsley et al., 2016). These two additional model grids give similar, though understandably not quite identical, yields for the same $^{12}C + ^{16}O$ rate. We introduce several attenuation factors ξ_{CO}: 0, 0.7 and 0.9 for the DDTs, and 0, 0.7, 0.9 and 0.99 for the sub-M_{Ch}. We use the rate given by $\lambda = (1 - \xi_{CO})\,\lambda_{CF88}$, where λ_{CF88} is the standard $^{12}C + ^{16}O$ rate (Caughlan & Fowler, 1988),

so $\xi_{CO} = 0, 1$ corresponds to null and full suppression, respectively.

Why does varying the $^{12}C + ^{16}O$ rate change the Ca/S mass ratio? First, consider the case where the $^{12}C + ^{16}O$ rate is zero. At oxygen burning temperatures, oxygen could react with itself to mainly produce $^{16}O(^{16}O,\alpha)^{28}Si$. We will refer to this as the "alpha-poor" branch since only one α-particle is produced. Alternatively, oxygen can photodisintegrate to produce carbon, $2(^{16}O) + 2\gamma \rightarrow 2(^{12}C) + 2\alpha$. If this carbon only recombines with the emitted α-particle to produce ^{16}O, then this equilibrium loop is not interesting for our purposes here. The other option is for carbon to burn with itself to mainly produce $^{12}C(^{12}C,\alpha)^{20}Ne$. Photodisintegration of ^{20}Ne then returns the nuclear flows to ^{16}O via $^{20}Ne(\gamma,\alpha)^{16}O$. The net flow of this oxygen cycle is $^{16}O(^{16}O,4\alpha)^{16}O$. We will refer to this as the "alpha-rich" branch since four α-particles are produced. The alpha-poor and alpha-rich branches compete with each other. Which branch dominates depends on the thermodynamic conditions and reaction rates. If the alpha-poor branch wins, then the ^{32}S and ^{40}Ca abundances will be low. If the alpha-rich branch wins, then the ^{32}S and ^{40}Ca abundances will be high.

Now consider the case where the $^{12}C + ^{16}O$ rate is nonzero. The $^{12}C + ^{16}O$ branching ratios are not important because the main products from this reaction (^{24}Mg ^{27}Al, and ^{27}Si) ultimately produce ^{28}Si. That is, the net nuclear flow is $^{12}C + ^{16}O \rightarrow ^{28}Si$. If ^{12}C burns only by reactions with ^{16}O, the reaction flow for oxygen photodisintegration is $^{16}O + \gamma \rightarrow ^{12}C + \alpha$, then $^{12}C + ^{16}O \rightarrow ^{28}Si$. This is the same single α-particle yield as the alpha-poor branch (Woosley et al., 1971). Thus, the net effect of a nonzero $^{12}C + ^{16}O$ rate is to assist the alpha-poor branch, to produce less α-particles.

De et al. (2014) and Miles et al. (2016) showed that the Ca/S mass ratio in SN Ia ejecta scales as the square of the α-particle abundance. Increasing the $^{12}C + ^{16}O$ rate (decreasing ξ_{CO}) suppresses the α-particle abundance, which in turn decreases M_{Ca}/M_S. There is less sensitivity to the $^{12}C + ^{16}O$ rate at higher metallicity (more ^{22}Ne) because the increased neutron richness opens additional channels for α-particles, so that the action of the $^{12}C + ^{16}O$ reaction to shift α-particle flows toward the alpha-poor branch is less important.

In Figure 25, we show how the various $^{12}C + ^{16}O$ rate multipliers affect the determination of Z_{eq} for 3C 397, Kepler and Tycho by analyzing M_{Ca}/M_S vs M_{Cr}/M_{Fe} and linearly interpolating within the model grids as done for Figure 22. We choose these remnants be-

cause our inferred Z_{eq} estimates agree with previous measurements based on Fe-peak nuclei, which are not affected by the $^{12}C+^{16}O$ rate (see the discussion in Section III.3.1). In order to recover Z_{eq} values that are consistent with the ones found by Yamaguchi et al. (2015), the suppression factor has to be at least of the order of $\xi_{CO} = 0.9$ (attenuation $\gtrsim 90\%$). We conclude that the $^{12}C+^{16}O$ rate is attenuated in nature, but we emphasize that a more in-depth analysis is required to get to the bottom of this newly identified problem in SN Ia nucleosynthesis. For the purposes of this work, we point out that the correspondence between M_{Ca}/M_S values and equivalent progenitor metallicities in our Figures 20, 21 and 22 is tentative and might need to be revised in the future. This certainly complicates our analysis, but it does not invalidate our main conclusions that (1) the neutronization in SN Ia ejecta appears to be high, given the values of M_{Ca}/M_S measured in G337.2−0.7 and 3C 397 and the dependence between M_{Ca}/M_S and neutronization identified by De et al. (2014), and (2) because the Ca/S mass ratio in SNR N103B in the LMC is comparable to that of Milky-Way-type Ia SNRs, it seems unlikely that progenitor metallicity alone can be responsible for this high neutronization.

III.5 CONCLUSIONS

We have inferred the neutronization in the ejecta of five Type Ia SNRs (3C 397, N103B, G337.2−0.7, Kepler and Tycho) from their X-ray spectra, using a new method based on the sensitivity of the Ca/S yield to η discussed in De et al. (2014). The neutronization inferred for N103B, in the LMC, is comparable to the values determined for Tycho and Kepler, in the Milky Way, which indicates that progenitor metallicity cannot be the only source of neutrons in SN Ia ejecta.

By comparing to a grid of SN Ia explosion models, we have translated our measured Ca/S mass ratios to equivalent progenitor metallicities, which can be compared to the MDFs in the Milky Way and the LMC. These comparisons rule out progenitor metallicity as the sole source of neutrons for 3C 397, G337.2−0.7, and N103B. This represents a conundrum for SN Ia progenitors. Since our measurements are not affected by n-NSE and progenitor

metallicity is discarded, the only possible source of neutronization left that we know can affect the whole ejecta is C simmering. Recent models of simmering by Martínez-Rodríguez et al. (2016) indicate that the highest level of neutronization is $\simeq 0.2\,Z_{\odot}$, which is too low to explain the observations. This implies that either there is a fourth, as yet unidentified, source of neutronization in SN Ia progenitors, or that these simmering models do not capture the full phenomenology of C simmering. Lately, Piersanti et al. (2017) have suggested that the simmering contribution to η is higher than that of Martínez-Rodríguez et al. (2016), but more work is needed to understand the differences between both analyses.

We have also identified an issue affecting most SN Ia nucleosynthesis calculations in the literature. The Ca/S mass ratio in the final yields is very sensitive to the precise value of the $^{12}\mathrm{C}+^{16}\mathrm{O}$ reaction rate (see Figure 24), with the most widely used rate value leading to Ca/S mass ratios that are too low to reproduce our measurements by a factor of ~ 2 (shown in Figure 23). Given the excellent correspondence between the SN Ia model grid used in this work, where this reaction rate is not included, and our $\mathrm{M_{Ca}/M_S}$ measurements, we conclude that the $^{12}\mathrm{C}+^{16}\mathrm{O}$ reaction rate must be suppressed in nature by a potentially large factor. A preliminary exploration of SN Ia nucleosynthesis calculations with varying degrees of suppression in the $^{12}\mathrm{C}+^{16}\mathrm{O}$ reaction, displayed in Figure 25, confirms this conclusion, but a more detailed analysis is needed to get to the bottom of this issue (e.g., Bucher et al., 2015; Fang et al., 2017). Until this study is completed, our estimates of Z_{eq} must be considered tentative, and will need to be revised.

We emphasize that our main results are not sensitive to these details. The values of $\mathrm{M_{Ca}/M_S}$ measured in our SNRs G337.2−0.7 and 3C 397 do require a high degree of neutronization in SN Ia ejecta, by virtue of the effect discovered by De et al. (2014). Most importantly, the fact that SNR N103B in the LMC shows a Ca/S mass ratio similar to those of Milky Way SNRs like Tycho strongly suggests that metallicity alone cannot be the origin of this high neutronization. Unless a new source of neutrons in SNe Ia is identified, the simplest explanation for this high neutronization is that a large fraction of SNe Ia in the local universe explode close to $\mathrm{M_{Ch}}$ after developing a large convective core through carbon simmering.

We are grateful to Michael Hayden for sharing his APOGEE data with which we gener-

ated the MDF for the Milky Way disk. We also thank Luc Déssart for sharing his supernova models with us, Peter Höflich for insightful discussions about the nucleosynthesis in these models, and Stan Woosley for his help to interpret his nucleosynthetic yields. H.M.-R., C.B., H.Y. and S.P. are funded by the NASA ADAP grant NNX15AM03G S01. H.M.-R. also acknowledges support from a PITT PACC Fellowship, and C.B. from the OCIW Distinguished Visitor program at the Carnegie Observatories. E.B. is supported by the MINECO-FEDER grant AYA2015-63588-P. This research has made use of NASA's Astrophysics Data System (ADS, http://adswww.harvard.edu/) and of the HEASARC spectral data base (http://heasarc.gsfc.nasa.gov/).

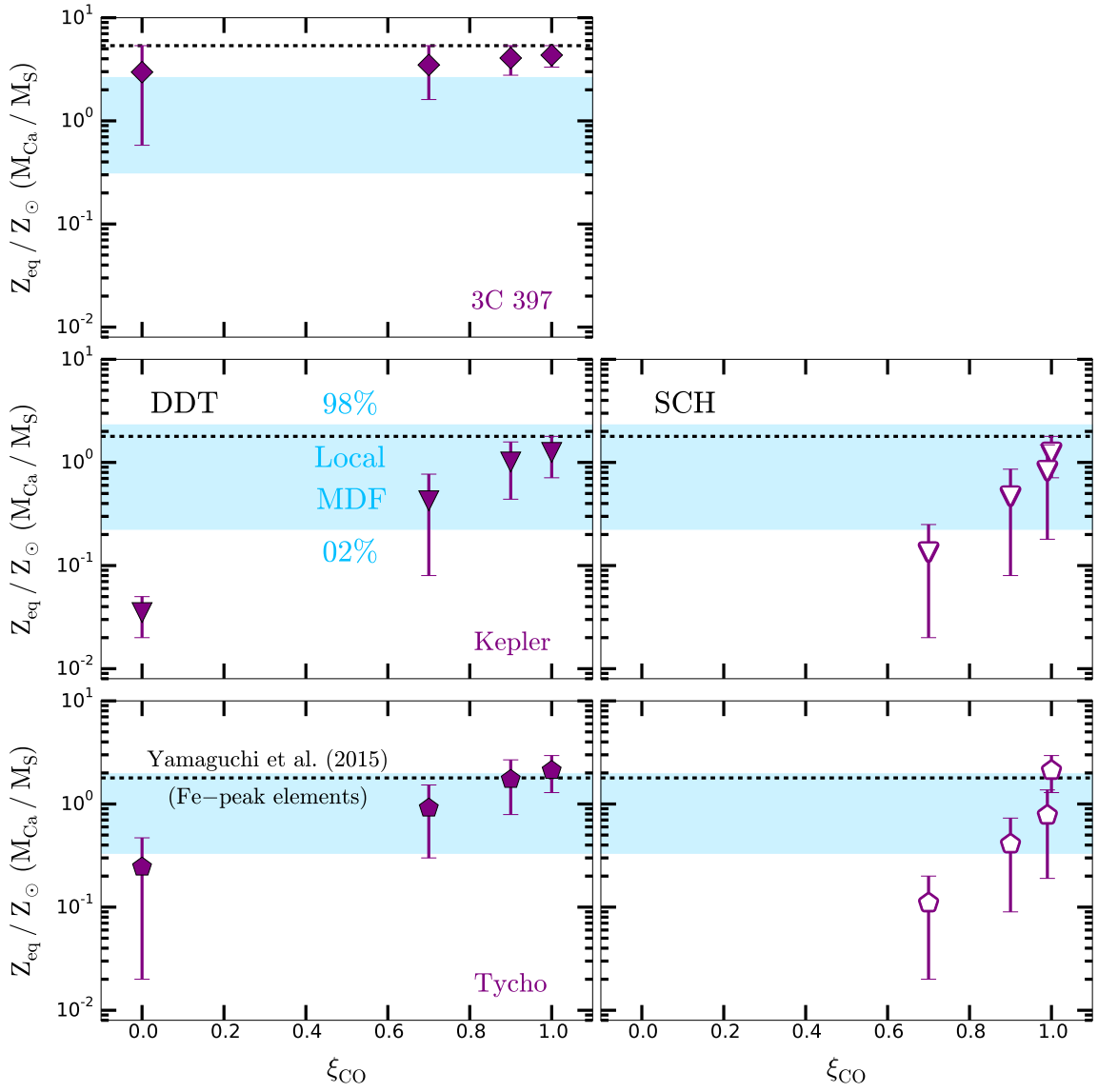

Figure 25: Effect of different attenuations factors ξ_{CO} acting over the $^{12}C+^{16}O$ reaction rate on the inferred equivalent metallicities Z_{eq} for 3C 397, Kepler and Tycho. Values shown for $\xi_{CO} = 1$ are the same as those interpolated from Figure 20 and displayed in Figure 22. The black, dashed lines depict the equivalent metallicities found by Yamaguchi et al. (2015), whereas the blue, shaded regions represent the local MDF for the Milky Way disk in the environment of each SNR (numbers indicate percentiles). Left: M_{Ch}-models. Right: sub-M_{Ch} models. We note that 3C 397 is not compatible with the latter. While the inferred neutron excess, Z_{eq}, is lower with the uncertain $^{12}C+^{16}O$ reaction included ($\xi_{CO} < 1$), 3C 397 still shows evidence of an elevated metallicity compared to the other remnants.

IV CHANDRASEKHAR AND SUB-CHANDRASEKHAR MODELS FOR THE X-RAY EMISSION OF TYPE IA SUPERNOVA REMNANTS (I): BULK PROPERTIES

Martínez-Rodríguez, H., Badenes, C., Lee, S.-H., et al. 2018, ApJ, 865, 1515

IV.1 INTRODUCTION

Type Ia supernovae (SNe Ia) are the thermonuclear explosions of white dwarf (WD) stars that are destabilized by mass accretion from a close binary companion. They are important for a wide range of topics in astrophysics, e.g. galactic chemical evolution (Kobayashi et al., 2006; Andrews et al., 2017; Prantzos et al., 2018), studies of dark energy (Riess et al., 1998; Perlmutter et al., 1999) and constraints on ΛCDM parameters (Betoule et al., 2014; Rest et al., 2014). Yet, basic aspects of SN Ia physics, such as the nature of their stellar progenitors and the triggering mechanism for the thermonuclear runaway, still remain obscure. Most proposed scenarios for the progenitor systems of SNe Ia fall into two broad categories: the single degenerate (SD), where the WD companion is a nondegenerate star, and the double degenerate (DD), where the WD companion is another WD (see Wang & Han, 2012; Maoz et al., 2014; Livio & Mazzali, 2018; Soker, 2018; Wang, 2018, for recent reviews).

In the SD scenario, the WD accretes material from its companion over a relatively long timescale ($t \sim 10^6$ years) and explodes when its mass approaches the Chandrasekhar limit $M_{Ch} \simeq 1.4\,M_\odot$ (Nomoto et al., 1984; Thielemann et al., 1986; Hachisu et al., 1996; Han & Podsiadlowski, 2004). Conversely, in most DD scenarios, the WD becomes unstable after a merger or a collision on a dynamical timescale (Iben & Tutukov, 1984) and explodes

with a mass that is not necessarily close to M_{Ch} (e.g., Raskin et al., 2009; van Kerkwijk et al., 2010; Kushnir et al., 2013). In theory, distinguishing between SD and DD systems should be feasible, given that some observational probes are sensitive to the duration of the accretion process or to the total mass prior to the explosion (e.g., Badenes et al., 2007, 2008a; Seitenzahl et al., 2013a; Margutti et al., 2014; Scalzo et al., 2014; Yamaguchi et al., 2015; Chomiuk et al., 2016; Martínez-Rodríguez et al., 2016).

Sub-Chandrasekhar models (e.g., Woosley & Weaver, 1994; Sim et al., 2010; Woosley & Kasen, 2011) are a particular subset of both SD and DD SN Ia progenitors. To first order, the mass of ^{56}Ni synthesized, and therefore the brightness of the supernova, is determined by the mass of the exploding WD. A sub-M_{Ch} WD cannot detonate spontaneously without some kind of external compression – double-detonations are frequently invoked (e.g., Shen et al., 2013; Shen & Bildsten, 2014; Shen & Moore, 2014; Shen et al., 2018). Here, a carbon-oxygen (C/O) WD accretes material from a companion and develops a helium-rich layer that eventually becomes unstable, ignites, and sends a shock wave into the core. This blast wave converges and creates another shock that triggers a carbon denotation, which explodes the WD. Violent mergers (e.g., Pakmor et al., 2012, 2013) are an alternative scenario where, right before the secondary WD is disrupted, carbon burning starts on the surface of the primary WD and a detonation propagates through the whole merger, triggering a thermonuclear runaway. Other studies present pure detonations of sub-M_{Ch} C/O WDs with different masses without addressing the question of how they were initiated. However, these studies are still able to reproduce many observables such as light curves, nickel ejecta masses, and isotopic mass ratios (Sim et al., 2010; Piro et al., 2014; Yamaguchi et al., 2015; Blondin et al., 2017; Martínez-Rodríguez et al., 2017; Goldstein & Kasen, 2018; Shen et al., 2018; Bravo et al., 2019).

After the light from the supernova (SN) fades away, the ejecta expand and cool down until their density becomes comparable to that of the ambient medium, either the interstellar medium (ISM) or a more or less extended circumstellar medium (CSM) modified by the SN progenitor. At this point, the supernova remnant (SNR) phase begins. The ejecta drive a blast wave into the ambient medium ("forward shock", FS), and the pressure gradient creates another wave back into the ejecta ("reverse shock", RS; McKee & Truelove, 1995;

Truelove & McKee, 1999).

The X-ray emission from young ($\sim$ a few 1000 years) SNRs is often-times dominated by strong emission lines from the shocked ejecta that can be used to probe the nucleosynthesis of the progenitor. These thermal ($\sim 10^7$ K) X-ray spectra are as diverse as their SN progenitors, and not even remnants of similar ages are alike. Their evolution and properties depend on various factors such as the structure and composition of the ejecta, the energy of the explosion, and the structure of the CSM that is left behind by the progenitor (e.g., Badenes et al., 2003, 2007; Patnaude et al., 2012, 2017; Woods et al., 2017, 2018).

Therefore, young SNRs offer unique insights into both the supernova explosion and the structure of the ambient medium. They are excellent laboratories to study the SN phenomenon (e.g., Badenes et al., 2005, 2006, 2008b; Badenes, 2010; Vink, 2012; Lee et al., 2013, 2014, 2015; Slane et al., 2014; Patnaude et al., 2015). The X-ray spectra of SNRs, unlike the optical spectra of SNe Ia, allow us to explore these issues without having to consider the complexities of radiative transfer (e.g., Stehle et al., 2005; Tanaka et al., 2011; Ashall et al., 2016; Wilk et al., 2018), because the plasma is at low enough density to be optically thin to its own radiation.

It is known that M_{Ch} models interacting with a uniform ambient medium can successfully reproduce the bulk properties of SNRs, such as ionization timescales (Badenes et al., 2007), Fe Kα centroid energies, Fe Kα luminosities (Yamaguchi et al., 2014a), and radii (Patnaude & Badenes, 2017). However, there has been no exploration of the parameter space associated with the evolution of sub-M_{Ch} explosion models during the SNR stage for various dynamical ages. Here, we develop the first model grid of sub-M_{Ch} explosions in the SNR phase. We compare the bulk spectral and dynamical properties of M_{Ch} and sub-M_{Ch} models to the observed characteristics of Galactic and Magellanic Cloud Ia SNRs.

This paper is organized as follows. In Section IV.2, we describe our hydrodynamical SNR models and the derivation of synthetic X-ray spectra. In Section IV.3, we compare the bulk properties predicted by our model grid with observational data of Type Ia SNRs. Finally, in Section IV.4, we summarize our results and outline future analyses derived from our work.

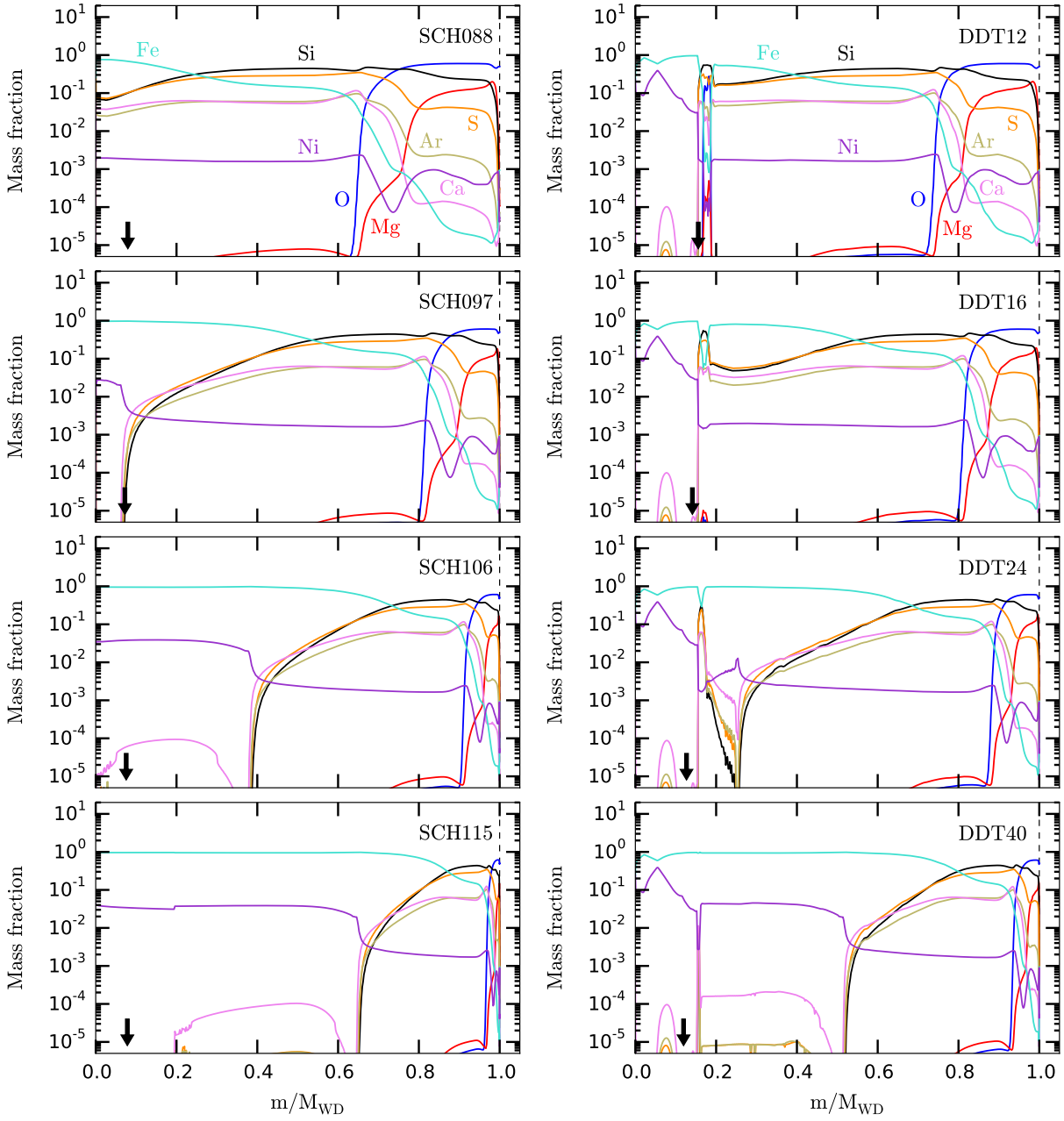

Figure 26: Chemical composition for our SN Ia models listed in Table 4. The vertical, dashed lines indicate the outer surface of each ejecta model. The arrows depict the locations of the RS at 538 years for $\rho_{\rm amb} = 2 \times 10^{-24}\,{\rm g\,cm^{-3}}$ (see the discussion in Section IV.2.3).

IV.2 METHOD

IV.2.1 Supernova explosion models

We use the spherically symmetric M_{Ch} and sub-M_{Ch} explosion models introduced in Yamaguchi et al. (2015), Martínez-Rodríguez et al. (2017) and McWilliam et al. (2018), which are calculated with a version of the code described in Bravo & Martínez-Pinedo (2012), updated to account for an accurate coupling between hydrodynamics and nuclear reactions (Bravo et al., 2016, 2019). The M_{Ch} models are delayed detonations (Khokhlov, 1991) with a central density $\rho_c = 3 \times 10^9\,\mathrm{g\,cm^{-3}}$, deflagration-to-detonation densities $\rho_{DDT}\,[10^7\,\mathrm{g\,cm^{-3}}] = 1.2, 1.6, 2.4, 4.0$ and kinetic energies $E_k\,[10^{51}\,\mathrm{erg}] = 1.18, 1.31, 1.43, 1.49$. They are similar to the models DDTe, DDTd, DDTb, and DDTa ($\rho_{DDT}\,[10^7\,\mathrm{g\,cm^{-3}}] = 1.3, 1.5, 2.6, 3.9$) by Badenes et al. (2003, 2005, 2006, 2008b). We label these explosions as DDT12, DDT16, DDT24, and DDT40.

The sub-M_{Ch} models are central detonations of C/O WDs with a core temperature $T_c\,[\mathrm{K}] = 10^8$, masses $M_{WD}\,[M_\odot] = 0.88, 0.97, 1.06, 1.15$, and kinetic energies $E_k\,[10^{51}\,\mathrm{erg}] = 0.92, 1.15, 1.33, 1.46$, similar to the models by Sim et al. (2010). We label these explosions as SCH088, SCH097, SCH106, and SCH115. For both sets of models, the progenitor metallicity is $Z = 0.009$ ($0.64\,Z_\odot$ taking $Z_\odot = 0.014$, Asplund et al. 2009). We choose this value because it is close to the metallicity $Z = 0.01$ employed by Badenes et al. (2003, 2005, 2006, 2008b) in their M_{Ch} progenitors. The intermediate-mass elements (Si, S, Ar, Ca) are produced in the outer region of the exploding WDs, whereas the iron-peak elements (Cr, Mn, Fe, Ni) are synthesized in the inner layers. Table 4 presents the total yields for some representative elements in these M_{Ch} and sub-M_{Ch} models. Figure 26 shows the chemical profiles as a function of the enclosed mass for each model.

Table 4: Total yields for the sub-M_{Ch} and M_{Ch} progenitor models. See Bravo et al. (2019) for details and extended yields

Progen.	M_C ($M_\odot$)	M_O ($M_\odot$)	M_{Ne} ($M_\odot$)	M_{Mg} ($M_\odot$)	M_{Si} ($M_\odot$)	M_S ($M_\odot$)	M_{Ar} ($M_\odot$)	M_{Ca} ($M_\odot$)	M_{Cr} ($M_\odot$)	M_{Mn} ($M_\odot$)	M_{Fe} ($M_\odot$)	M_{Ni} ($M_\odot$)
SCH088	3.95E-03	1.40E-01	2.54E-03	1.99E-02	2.79E-01	1.66E-01	3.70E-02	3.72E-02	6.90E-03	2.68E-03	1.82E-01	1.19E-03
SCH097	1.62E-03	7.66E-02	8.24E-04	7.80E-03	2.09E-01	1.36E-01	3.26E-02	3.52E-02	1.12E-02	4.24E-03	4.50E-01	3.18E-03
SCH106	6.91E-04	3.74E-02	2.80E-04	2.61E-03	1.38E-01	9.62E-02	2.39E-02	2.63E-02	9.11E-03	3.46E-03	7.01E-01	1.54E-02
SCH115	2.75E-04	1.47E-02	8.99E-05	6.34E-04	7.66E-02	5.66E-02	1.47E-02	1.66E-02	6.31E-03	2.40E-03	9.25E-01	2.71E-02
DDT12	4.88E-03	1.75E-01	3.88E-03	2.64E-02	3.84E-01	2.34E-01	5.29E-02	5.32E-02	1.50E-02	7.12E-03	3.84E-01	3.15E-02
DDT16	2.52E-03	1.19E-01	1.83E-03	1.55E-02	3.05E-01	1.98E-01	4.79E-02	5.20E-02	2.02E-02	8.76E-03	5.70E-01	3.16E-02
DDT24	1.26E-03	7.15E-02	7.06E-04	7.26E-03	2.10E-01	1.42E-01	3.54E-02	3.98E-02	2.20E-02	1.00E-02	8.00E-01	3.23E-02
DDT40	5.33E-04	3.80E-02	2.62E-04	2.88E-03	1.35E-01	9.43E-02	2.38E-02	2.66E-02	1.59E-02	7.51E-03	9.69E-01	5.03E-02

IV.2.2 Supernova remnant models

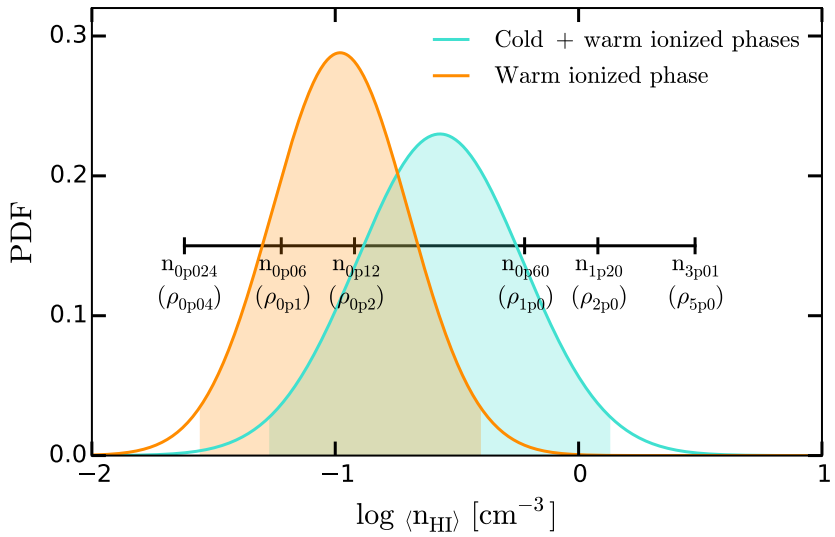

Figure 27: Log-normal probability distribution functions (PDFs) for the diffuse gas in the Milky Way (Berkhuijsen & Fletcher, 2008). The shaded contours represent the 2σ regions for each PDF. The six $n_{\rm amb}$ values used in this work $(0.024, 0.06, 0.12, 0.60, 1.20, 3.01\,{\rm cm}^{-3})$ are depicted along a black, horizontal line.

We study the time evolution of these SN Ia models with a self-consistent treatment of the nonequilibrium ionization (NEI) conditions in young SNRs performed by the cosmic ray-hydro-NEI code, hereafter `ChN` (Ellison et al., 2007; Patnaude et al., 2009; Ellison et al., 2010; Patnaude et al., 2010; Castro et al., 2012; Lee et al., 2012, 2014, 2015). `ChN` is a one-dimensional Lagrangian hydrodynamics code based on the multidimensional code `VH-1` (e.g., Blondin & Lufkin, 1993). `ChN` simultaneously calculates the thermal and nonthermal emission at the FS and RS in the expanding SNR models. It couples hydrodynamics, NEI calculations, plasma emissivities, time-dependent photoionization, radiative cooling, forbidden-line emission, and diffusive shock acceleration, though we do not include diffusive shock acceleration in our calculations. `ChN` is a tested, flexible code that has successfully been used to model SNRs in several settings (e.g. Slane et al., 2014; Patnaude et al., 2015).

Young Ia SNRs are in NEI because, at the low densities involved ($n \sim 1\,{\rm cm}^{-3}$), not enough

time has elapsed since the ejecta were shocked to equilibrate the ionization and recombination rates (Itoh, 1977; Badenes, 2010). Consequently, these NEI plasmas are underionized when compared to collisional ionization equilibrium plasmas (Vink, 2012). The shock formation and initial plasma heating do not stem from Coulomb interactions, but from fluctuating electric and magnetic fields in these so-called collisionless shocks (Vink, 2012). In the ISM, the mean free path and the typical ages for particle-to-particle interactions are larger than those of SNRs ($\approx 10^2 - 10^3$ years, $\approx 1 - 10$ pc).

The efficiency of electron heating at the shock transition, i.e., the value of $\beta = T_e/T_i$ at the shock, is not well determined (see, e.g., Borkowski et al., 2001). In principle, the value of β can range between $\beta = \beta_{\rm min} = m_e/m_i$ and full equilibration ($\beta = 1$), with partial equilibration being the most likely situation ($\beta_{\rm min} < \beta < 1$, Borkowski et al., 2001; Ghavamian et al., 2007; Yamaguchi et al., 2014b). Here we set $\beta = \beta_{\rm min}$ for illustration purposes, even though previous studies (e.g., Badenes et al., 2005, 2006; Yamaguchi et al., 2014a) have shown that β has an important effect on the Fe Kα luminosities. This can be critical when trying to fit an SNR spectrum with a specific model, but here we are just interested in the bulk properties of the models, and we defer detailed fits to future work.

We consider uniform ambient media composed of hydrogen ($\rho_{\rm amb} = m_H\, n_{\rm amb}$, e.g. Badenes et al., 2003, 2006, 2008b; Patnaude & Badenes, 2017) with a range of densities: $\rho_{\rm amb}\,[10^{-24}\,{\rm g\,cm^{-3}}] = 0.04, 0.1, 0.2, 1.0, 2.0, 5.0 \equiv n_{\rm amb}\,[{\rm cm^{-3}}] = 0.024, 0.06, 0.12, 0.60, 1.20, 3.01$. We label each SNR model from the SN model and ambient medium density, e.g. SCH115_0p04, SCH115_0p1, SCH115_0p2, SCH115_1p0, SCH115_2p0, and SCH115_5p0. We have chosen these ambient densities to be in the same range considered by Patnaude et al. (2015). The three highest densities were used in the studies by Patnaude et al. (2012) and Yamaguchi et al. (2014a), so we will be able to compare our results to theirs. This makes a total of 48 SNR models that we evolve up to an expansion age of 5000 years. For each SNR model, we record a total of 30 time epochs, starting at 105 years. The time bins are linearly spaced at young ages and smoothly become logarithmically spaced at late ages. We also record 30 Lagrangian profiles in linearly spaced time bins for each model.

Our choice of ambient medium densities is motivated by observations of the ISM in the Milky Way. Interstellar gas can be found in five different phases (Ferrière, 1998, 2001):

molecular ($T_{mol} \sim 10 - 20$ K, $n_{mol} \sim 10^2 - 10^6$ cm^{-3}), cold neutral ($T_{cold} \sim 50 - 100$ K, $n_{cold} \sim 20 - 50$ cm^{-3}), warm neutral ($T_{warm,n} \sim 6000 - 10000$ K, $n_{warm,n} \sim 0.2 - 0.5$ cm^{-3}), warm ionized ($T_{warm,i} \sim 8000$ K, $n_{warm,i} \sim 0.2 - 0.5$ cm^{-3}), and hot ionized ($T_{hot} \sim 10^6$ K, $n_{hot} \sim 0.0065$ cm^{-3}). Among these, the warm ionized phase has the highest filling factor and therefore is the most likely environment for Type Ia SNRs. Wolfire et al. (2003) gives a mean value for the neutral hydrogen density in the Galactic disk $\langle n_{HI} \rangle = 0.57$ cm^{-3}. More recently, Berkhuijsen & Fletcher (2008) fit log-normal distributions to the diffuse gas in the MW centered on $\langle n_{HI} \rangle \approx 0.3$ cm^{-3} (cold and warm ionized) and $\langle n_{HI} \rangle \approx 0.1$ cm^{-3} (warm ionized). We compare these distributions to our uniform density values in Figure 27.

Figure 28 shows the profile time evolution for a fiducial model, explosion progenitor SCH115 with an ambient density $\rho_{\rm amb} = 2 \times 10^{-24}\,{\rm g\,cm^{-3}}$. The profiles for 186 (navy), 518 (crimson), and 1016 (turquoise) years show the RS propagation toward the center of the SNR. After reaching the center, the RS bounces back and moves outwards into the previously shocked ejecta, creating more reflected shocks when it reaches the contact discontinuity (CD). This effect can be seen in the first and the second panel of Figure 28 (T_e versus M, ρ versus M) around $M \sim 0.05\,M_\odot$ and $M \sim 20\,M_\odot$ at 5000 years (brown).

T_e increases with time in the inner layers after they are swept by the RS. As the SNR expands, the density ρ of the shocked ejecta and ISM decreases steadily, and therefore the electron density n_e diminishes with time. In `ChN`, the unshocked plasma is assumed to be 10% singly ionized.

The salient features in the evolution of this particular SNR model are representative of the entire grid. The ejecta with the highest ionization state are always found close to the contact discontinuity (CD), since they were shocked at an earlier age and higher density. Because this is also the densest region at all times, it has the highest emission measure and thus will dominate the spatially integrated X-ray emission. However, since the chemical composition of SN Ia ejecta is markedly stratified, it is often the case that different chemical elements sample different parts of the SNR structure, and therefore show different ionization timescales and electron temperatures (see the discussions in Badenes et al., 2003, 2005). This feature of the models is in good agreement with observations of young SNRs (e.g. Badenes et al., 2007).

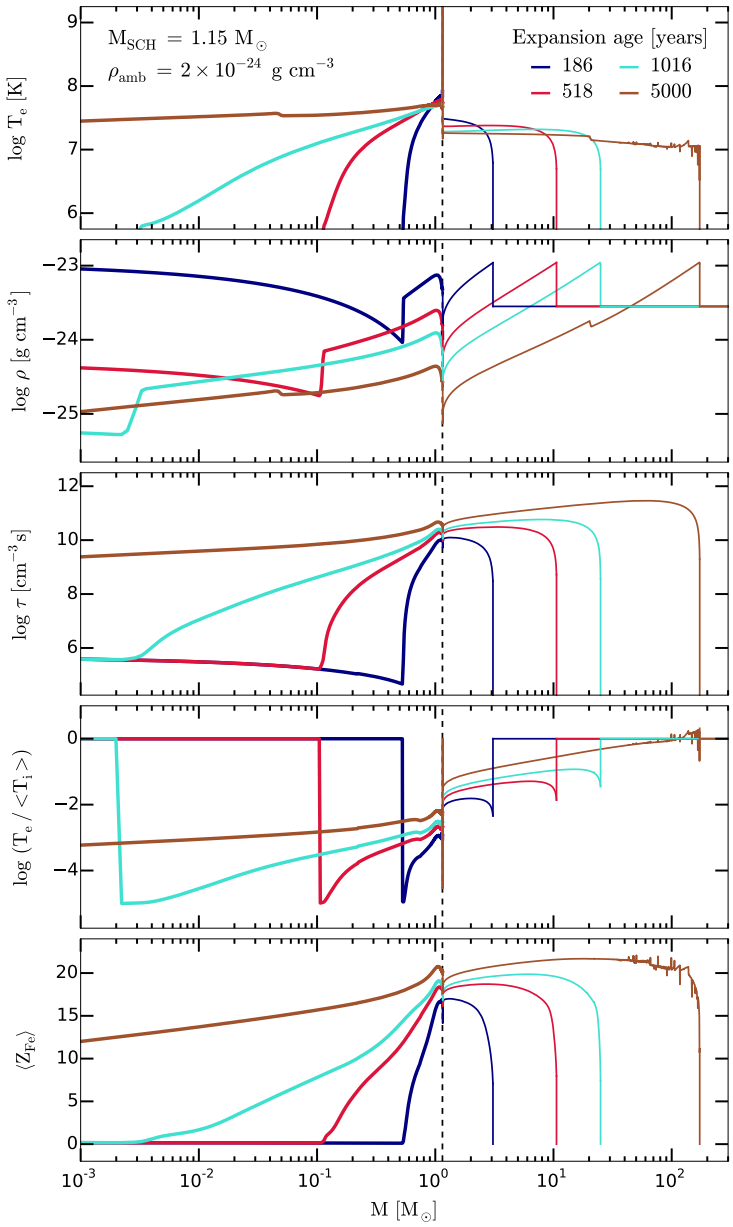

Figure 28: Time evolution of the electron temperature T_e, density ρ, ionization timescale $\tau = n_e t$, average efficiency of post-shock equilibration $T_e/\langle T_i \rangle$ and average iron effective charge state $\langle z_{\rm Fe} \rangle$ profiles as a function of the enclosed mass for model SCH115_2p0. The CD between the ejecta (thick lines) and the ambient medium swept up by the FS (thin lines) is depicted as a dashed, black vertical line, located at $1.15\,M_\odot$. The spatial location of the RS can be appreciated in the navy ($\sim 0.55\,M_\odot$), the crimson ($\sim 0.1\,M_\odot$) and the turquoise ($\sim 0.002\,M_\odot$) profiles.

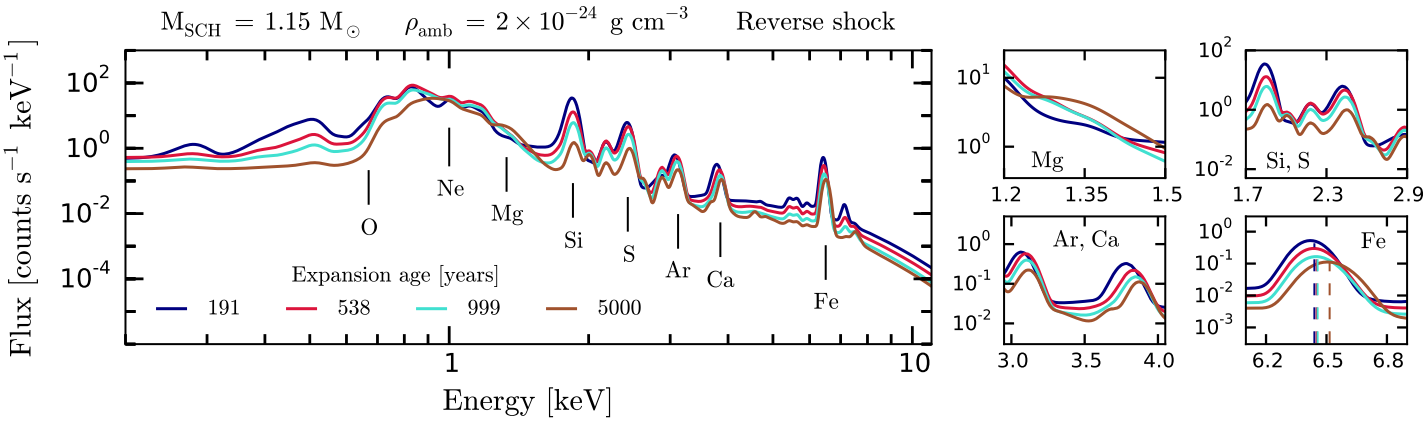

Figure 29: Integrated RS synthetic spectra normalized to $D = 10$ kpc for the model shown in Figure 28 at the nearest time snapshots (see the explanation in the text). The relevant atomic transitions are labeled. The zoomed boxes depict different energy regions: Mg (up left), Si, S (up right), Ar, Ca (low left), and Fe (low right). The latter shows the time evolution of the Fe Kα centroid energy (dashed, vertical lines).

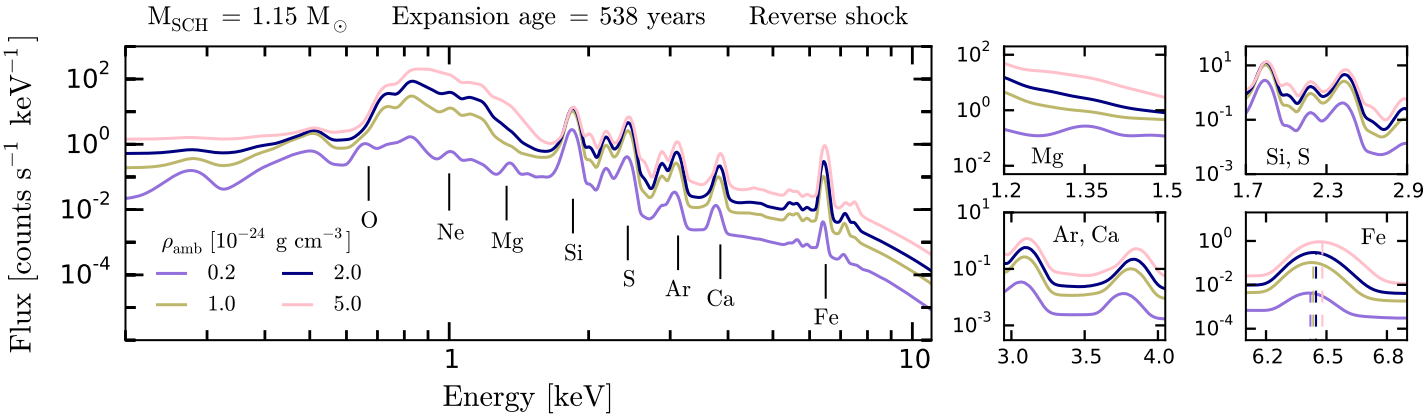

Figure 30: Integrated RS synthetic spectra normalized to $D = 10$ kpc for model SCH115, for the four highest ambient densities (ρ_{0p2}, ρ_{1p0}, ρ_{2p0}, ρ_{5p0}) and a fixed expansion age of 538 years. The zoomed boxes are identical to those of Figure 29.

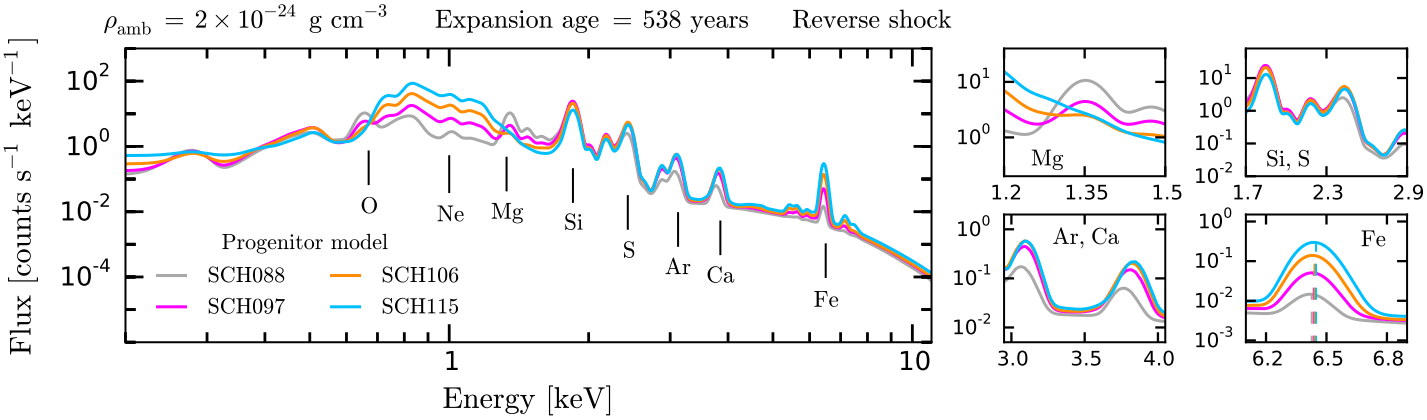

Figure 31: Integrated RS synthetic spectra normalized to $D = 10$ kpc for models SCH088, SCH097, SCH106, and SCH115 at a fixed expansion age of 538 years and a fixed ambient density $\rho_{amb} = 2 \times 10^{-24}\,\mathrm{g\,cm^{-3}}$. The zoomed boxes are identical to those of Figure 29.

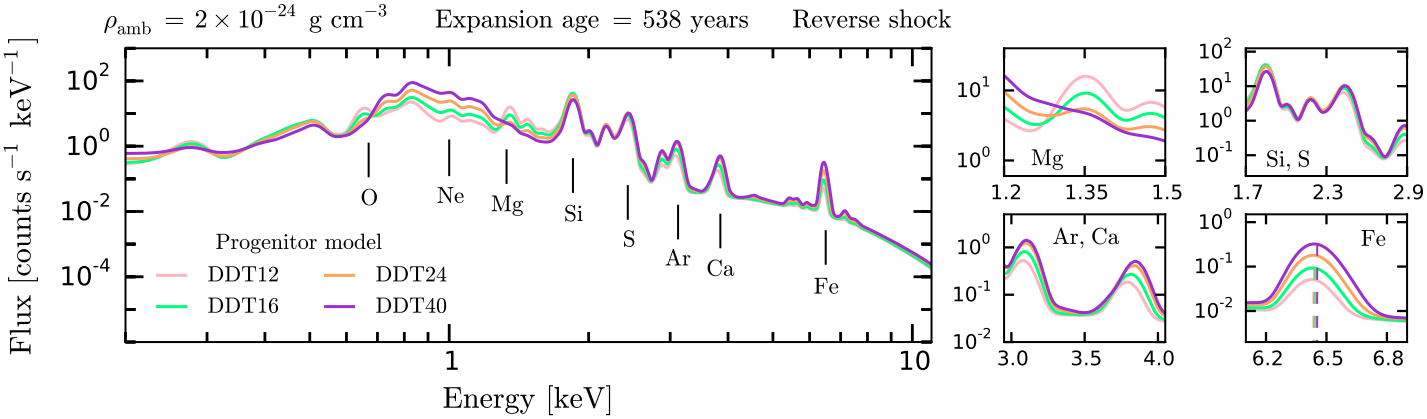

Figure 32: Integrated RS synthetic spectra normalized to $D = 10$ kpc for models DDT12, DDT16, DDT24, and DDT40 at a fixed expansion age of 538 years and a fixed ambient density $\rho_{amb} = 2 \times 10^{-24}\,\mathrm{g\,cm^{-3}}$. The zoomed boxes are identical to those of Figure 29.

IV.2.3 Synthetic spectra

Our ejecta models determine the masses, chemical abundances, and initial velocities for each mass layer. We consider 19 elements: H, He, C, N, O, Ne, Na, Mg, Al, Si, P, S, Ar, Ca, Ti, Cr, Mn, Fe, and Ni, with a total of 297 ions. For each ion species I corresponding to an element X, we calculate the differential emission measure (DEM) in 51 equally log-spaced T_e bins between 10^4 and 10^9 K, normalized to a distance of $D = 10$ kpc (Badenes et al., 2003, 2006):

$$(\mathrm{DEM})_{\mathrm{I,X}} = \mathrm{n_I\, n_e} \times \frac{\mathrm{dV}}{\mathrm{dT_e}} \times \frac{1}{4\pi \mathrm{D[cm]}^2} \times \frac{10^{-14}}{\mathrm{angr(X)}} \tag{2}$$

where n_I , n_e are the ion and electron densities, dV is the volume element for each layer, angr(X) are the `XSPEC` (Arnaud, 1996) default conversion factors for the solar abundances (Anders & Grevesse, 1989) and 10^{-14} is a normalization applied to the emissivities in `XSPEC`. We couple these DEMs to the atomic emissivity code `PyAtomDB` (`AtomDB` version 3.0.9; see, e.g., Foster et al., 2012, 2014) in order to calculate the emitted flux for each model at a given photon energy. We separate the RS and the FS contribution and generate nonconvolved photon spectra in 10000 equally spaced bins of size 1.2 eV between 0.095 and 12.094 keV. Thermal broadening and line splitting due to bulk motions are ignored in this version of the synthetic spectra, but we plan to include them in future versions.

We generate synthetic spectra for both RS and FS convolved with the *Suzaku* spectral and ancillary responses (Mitsuda et al., 2007). We choose *Suzaku* over *Chandra* or *XMM–Newton* for illustration purposes, given its superior spectral resolution around the Kα transitions from Fe-peak elements ($\approx 5.5 - 8.0$ keV). For simplicity, we do not include the effect of interstellar absorption (relevant below ~ 1 keV). In any case, most Ia SNRs have column densities smaller than $10^{22}\,\mathrm{cm}^{-2}$ (e.g., Lewis et al., 2003; Warren & Hughes, 2004; Badenes et al., 2006; Reynolds et al., 2007; Kosenko et al., 2010; Yamaguchi et al., 2014b). All the convolved and nonconvolved spectra are publicly available in a repository (`https://github.com/hector-mr`).

Table 5: Data corresponding to the Ia SNRs in our sample.

Name	$E_{\mathrm{Fe_{K\alpha}}}$[a] eV	$F_{\mathrm{Fe_{K\alpha}}}$[a] ($10^{-5}$ ph cm^{-2} s^{-1})	Distance (kpc)	$L_{\mathrm{Fe_{K\alpha}}}$ (10^{40} ph s^{-1})	Radius[b] (pc)	Age (years)	References[c]
Kepler	6438 ± 1	34.6 ± 0.2	$3.0 - 6.4$	91 ± 66	2.3 ± 0.9	414	1, 2, 3, 4
3C 397	6556^{+4}_{-3}	13.7 ± 0.4	$6.5 - 9.5$	105 ± 39	5.3 ± 0.5	$1350 - 5300$	5, 6
Tycho	6431 ± 1	61.0 ± 0.4	$2.5 - 3.0$	55 ± 10	3.3 ± 0.3	446	7, 8
RCW 86	6408^{+4}_{-5}	14.0 ± 0.7	2.5	10.5 ± 0.5	16	1833	9, 10, 11
SN 1006	6429 ± 10	2.55 ± 0.43	2.2	1.5 ± 0.3	10	1012	12
G337.2−0.7	6505^{+26}_{-31}	0.21 ± 0.06	$2.0 - 9.3$	0.8 ± 1.1	4.9 ± 3.2	$5000 - 7000$	13
G344.7−0.1	6463^{+9}_{-10}	4.03 ± 0.33	14	95 ± 8	16	$3000 - 6000$	14
G352.7−0.1	6443^{+8}_{-12}	0.82 ± 0.08	7.5	5.5 ± 0.5	6	~ 1600	15, 16
N103B	6545 ± 6	2.15 ± 0.10	50[d]	643 ± 30	3.6	~ 860	17, 18, 19
0509−67.5	6425^{+14}_{-15}	0.32 ± 0.04	50[d]	96 ± 12	3.6	~ 400	18, 20, 21
0519−69.0	6498^{+6}_{-8}	0.93 ± 0.05	50[d]	278 ± 15	4.0	~ 600	18, 21, 22
G1.9+0.3	6444	-	~ 8.5	1	~ 2.0	$\sim$150	23, 24
DEM L71	6494 ± 58	-	50[d]	26^{+8}_{-9}	8.6	~ 4700	25, 26, 27

[a]Centroid energies and fluxes from Yamaguchi et al. (2014a), except for G1.9+0.3 (Borkowski et al., 2013) and DEM L71 (Maggi et al., 2016), who report luminosities.
[b]For remnants with distance uncertainties, we calculate their radii using the angular diameters listed in Table 1 from Yamaguchi et al. (2014a).
[c]Representative references: (1) Reynoso & Goss (1999); (2) Sankrit et al. (2005); (3) Reynolds et al. (2007); (4) Park et al. (2013); (5) Safi-Harb et al. (2005); (6) Leahy & Ranasinghe (2016); (7) Badenes et al. (2006); (8) Tian & Leahy (2011); (9) Williams et al. (2011); (10) Yamaguchi et al. (2012a); (11) Castro et al. (2013); (12) Yamaguchi et al. (2008); (13) Rakowski et al. (2006); (14) Yamaguchi et al. (2012b); (15) Giacani et al. (2009); (16) Pannuti et al. (2014); (17) Lewis et al. (2003); (18) Rest et al. (2005); (19) Williams et al. (2014); (20) Warren & Hughes (2004); (21) Rest et al. (2008b); (22) Kosenko et al. (2010); (23) Reynolds et al. (2008); (24) Borkowski et al. (2013); (25) Hughes et al. (2003); (26) van der Heyden et al. (2003); (27) Maggi et al. (2016).
[b]Distance to the Large Magellanic Cloud (LMC) from Pietrzyński et al. (2013).

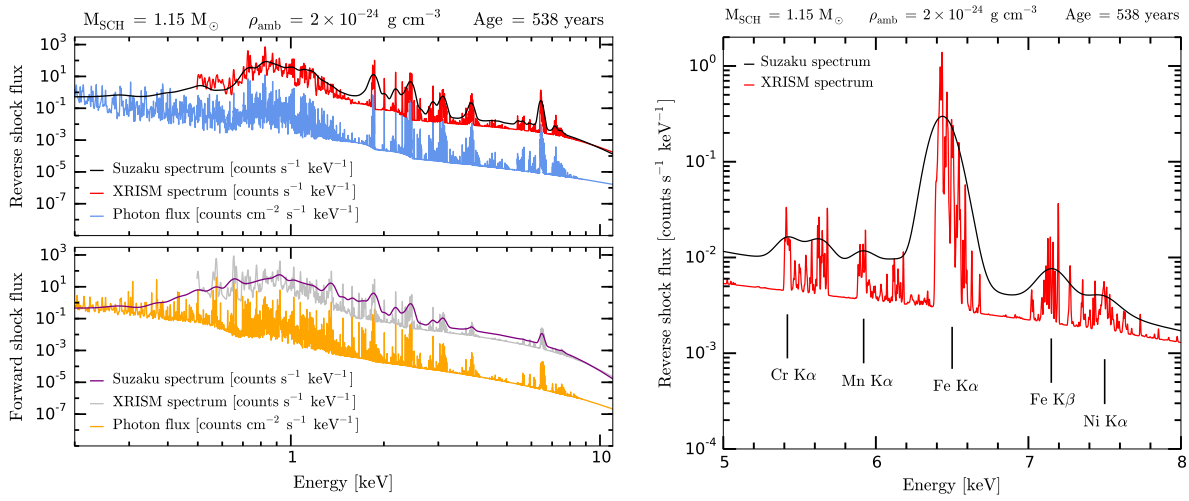

Figure 33: Left: Photon, *Suzaku* and *XRISM* spectra for model SCH115_2p0 at a fixed expansion age of 538 years (Top: Reverse shock. Bottom: Forward shock). Right: Zoomed-in reverse shock spectra around the Fe Kα complex. The relevant atomic transitions are labeled.

Figure 29 shows the time evolution of the X-ray flux from the RS for the fiducial model shown in Figure 28. We do not show the thermal spectrum from the FS because it is very weak or absent in many young Type Ia SNRs, often being replaced by nonthermal synchrotron emission (e.g., Warren & Hughes, 2004; Warren et al., 2005; Cassam-Chenaï et al., 2008). While the `ChN` code has the capability to model the modification of the FS dynamics and spectrum due to particle acceleration processes (e.g., Slane et al., 2014), this falls outside the scope of the present work. The thermal RS flux shown in Figure 29 decreases with time because the ejecta density decreases steadily, and the emission measure scales as n_e^2. This effect usually dominates over the steady increase in T_e due to electron-ion collisions in the shocked plasma (see Figure 28), which tends to increase the emitted flux. The centroids of the Kα transitions move to higher energies with time, especially for Ca, Fe, and Ni, because those elements have a large range of charge states. For elements with lower atomic numbers, like Si and S, the centroid energies saturate when the He-like ions become dominant, and then the Lyα transitions from H-like ions begin to appear. For this fiducial

model, the spectrum at 5000 years (brown) shows a Ti Kα feature at ≈ 4.5 keV.

Figure 30 shows the effect of varying the ambient medium density on the RS spectra for the same explosion model (SCH115) at a fixed expansion age of 538 years. Higher $\rho_{\rm amb}$ translate into higher ejecta densities due to a slower ejecta expansion. This yields higher fluxes and centroid energies for all transitions due to the increased rate of ionizing collisions. As $\rho_{\rm amb}$ increases, the Fe L-shell transitions dominate the flux around ~ 1 keV. Figures 31 and 32 show the RS spectra for all sub-$M_{\rm Ch}$ and $M_{\rm Ch}$ progenitor models with the same $\rho_{\rm amb}$ ($2 \times 10^{-24}\,{\rm g\,cm^{-3}}$) and expansion age (538 years). The differences between the models are largest in the bands dominated by the Fe L-shell and K-shell transitions. This is due to the different distribution of Fe-peak elements in the inner ejecta region for different models. In sub-$M_{\rm Ch}$ models with larger masses and $M_{\rm Ch}$ models with higher DDT transition densities, the Fe-peak elements extend further out in Lagrangian mass coordinate (see Figure 26). This translates into very different shocked masses of each element at a given age and ambient medium density for different explosion models, and therefore into large differences in the X-ray spectra. For Si and S, on the other hand, most of the ejected mass is already shocked at 538 years in all models ($M_{\rm shocked} = 0.81, 0.90, 0.98, 1.06\,M_\odot$ for models SCH088_2p0, SCH097_2p0, SCH106_2p0, SCH115_2p0, and $M_{\rm shocked} = 1.16, 1.18, 1.20, 1.21\,M_\odot$ for models DDT12_2p0, DDT16_2p0, DDT24_2p0, DDT40_2p0, shown in Figure 26), which translates into a smaller dynamic range of X-ray emitting masses and therefore smaller differences for the corresponding lines in the spectra. Elements like Mg and O are also fully shocked at this age, but their spectral blends show larger variations than those of Si and S because the dynamic range in ejected masses is much larger (see Table 4).

Our spectral models can also be convolved with the response matrices for future facilities, like the X-Ray Imaging and Spectroscopy Mission (*XRISM*, a.k.a. X-Ray Astronomy Recovery Mission, *XARM*, Tashiro et al., 2018) or *Athena* (Nandra et al., 2013). The left panel of Figure 33 shows the RS and FS spectra for model SCH115_2p0 at 538 years, unconvolved (photon flux) and after convolution with both *Suzaku* and *XRISM* responses. It is worth noting that *XRISM* will not be able to separate the FS and RS for the remnants in our sample. The improved energy resolution of *XRISM* reveals a wealth of transitions that cannot be seen with *Suzaku*, as shown in the right panel of Figure 33. There are two

transitions at ≈ 5.4 and ≈ 5.65 keV in both the *Suzaku* and the *XRISM* synthetic spectrum that do not appear in real *Suzaku* observations. We defer this to a future study.

The one-dimensional nature of our models deserves some comments. Multidimensional hydrodynamics coupled with NEI calculations (Warren & Blondin, 2013; Orlando et al., 2016) are computationally expensive, and do not allow to produce extensive model grids for an exhaustive exploration of parameter space like the one we present here. The results from Warren & Blondin (2013), who studied the impact of clumping and Rayleigh-Taylor instabilities in the morphology and ionization (but not emitted spectra) of Type Ia SNRs in 3D, do not show major deviations from one-dimensional calculations.

IV.3 DISCUSSION

IV.3.1 Type Ia SNRs: Bulk properties

Here we describe the bulk properties (expansion age, radius, Fe Kα centroid, and Fe Kα luminosity) of our M_{Ch} and sub-M_{Ch} models and compare them with the available observational data for Ia SNRs. We use the Fe Kα blend because it is sensitive to the electron temperature and ionization timescale in SNRs, with the centroid energy being a strong function of mean charge state (Vink, 2012; Yamaguchi et al., 2014a,b). This results in a clear division between Ia SNRs, which tend to interact with a low-density ambient medium, and core collapse (CC) SNRs, which often evolve in the high density CSM left behind by their massive and short-lived progenitors (first noted by Yamaguchi et al. 2014b, see also Patnaude et al. 2015; Patnaude & Badenes 2017). In their analysis, Yamaguchi et al. (2014a) already found that the bulk properties of the SNRs identified as Ia in their sample (those with Fe Kα centroid energies below 6.55 keV) were well reproduced by the M_{Ch} uniform ambient medium models of Badenes et al. (2003, 2005). Here, we perform a more detailed comparison to our models, which also assume a uniform ambient medium, but are based on an updated code and atomic data, and include both M_{Ch} and sub-M_{Ch} progenitors. We also comment briefly on some individual objects of interest.

We calculate the Fe Kα centroid energy $E_{\mathrm{Fe_{K\alpha}}}$ and luminosity $L_{\mathrm{Fe_{K\alpha}}}$ for each model as

$$E_{\mathrm{Fe_{K\alpha}}} = \frac{\int_{E_{\mathrm{min}}}^{E_{\mathrm{max}}} (F \times E)\, dE}{\int_{E_{\mathrm{min}}}^{E_{\mathrm{max}}} F\, dE} = \frac{\sum_{i\subseteq} F_i \times E_i \times dE_i}{\sum_{i\subseteq} F_i \times dE_i} \tag{3}$$

$$F_{\mathrm{Fe_{K\alpha}}} = \int_{E_{\mathrm{min}}}^{E_{\mathrm{max}}} F\, dE = \sum_{i\subseteq} F_i \times dE_i \tag{4}$$

$$L_{\mathrm{Fe_{K\alpha}}} = 4\pi D[\mathrm{cm}]^2 \times F_{\mathrm{Fe_{K\alpha}}} \tag{5}$$

where F is the differential flux from the nonconvolved spectrum after continuum subtraction, dE is the constant (1.2 eV) energy step, and $E_{\mathrm{min}} - E_{\mathrm{max}}$ is an energy interval that covers the entire Fe Kα complex (6.3 − 6.9 keV). We only compute these numbers when the Fe Kα emission is clearly above the continuum.

Table 5 summarizes the relevant observational properties of the 13 Type Ia SNRs in our sample. The data are taken from Yamaguchi et al. (2014a) (*Suzaku* observations). We also include the *Chandra* measurements for G1.9+0.3 (Borkowski et al., 2013) and the *XMM–Newton* results for DEM L71 (Maggi et al., 2016). The contours in Figures 34−37 show the parameter space spanned by our models, with symbols indicating the observed properties of individual SNRs. We display $L_{\mathrm{Fe_{K\alpha}}}$ versus $E_{\mathrm{Fe_{K\alpha}}}$ (Figure 34), $E_{\mathrm{Fe_{K\alpha}}}$ versus FS radius (R_{FS}, Figure 35), $E_{\mathrm{Fe_{K\alpha}}}$ versus expansion age (Figure 36), and R_{FS} versus expansion age (Figure 37).

The main features of the models shown in these plots merit some comments. In Figures 34−36, for the models with ρ_{1p0}, ρ_{2p0} and ρ_{5p0}, $E_{\mathrm{Fe_{K\alpha}}}$ decreases for a short time $\approx 1000-2000$ years after the explosion instead of increasing monotonically with time. This is due to the reheating of the shocked ejecta after the RS bounces at the SNR center. The reshocked material becomes denser and hotter, and therefore more luminous. This results in a lower luminosity-weighted ionization state for the shocked ejecta, which prior to RS bounce was dominated by the dense, highly ionized material close to the CD. As time goes on and the

entire ejecta is reshocked, the material close to the CD dominates the spectrum again, and the ionization state continues to increase monotonically. The strength of this feature is due to the spherical symmetry of our models, at least to some extent, but we expect a qualitatively similar (if weaker) effect in reality. We note that, although our model predictions are qualitatively similar to those from Badenes et al. (2003, 2005, 2006), Yamaguchi et al. (2014a) and Patnaude et al. (2015), there are small deviations – for instance, we predict a slightly higher $E_{\mathrm{Fe_{K\alpha}}}$ for the same ambient medium density and age (~ 6.6 keV versus ~ 6.5 keV). This is likely due to differences in the hydrodynamic code, atomic data, and explosion models. In addition, Patnaude et al. (2015) stopped their calculations when the RS first reached the center of the SNR, while we continue ours until the models reach an age of 5000 years.

Figures 34–37 show that the parameter space covered by our spherically symmetric, uniform ambient medium models is in good agreement with the observed data. While there are exceptions, which we discuss in detail below, it is clear that our models are a good first approximation to interpret the bulk dynamics of real Type Ia SNRs, and can be used to infer their fundamental physical properties. For example, denser ambient media and more energetic progenitor models predict higher $E_{\mathrm{Fe_{K\alpha}}}$ and $L_{\mathrm{Fe_{K\alpha}}}$ at a given expansion age, as seen in Figure 34. Thus, the SNRs with the highest $L_{\mathrm{Fe_{K\alpha}}}$, like 0519–69.0 and 0509–67.5, are only compatible with the brightest, most Fe-rich progenitor models (SCH106, SCH115, DDT16, and DDT24). The Fe Kα emission from SNR N103B, in particular, can only be reproduced by model DDT40 at the highest ambient medium density. As shown in Figures 35 and 37, R_{FS} has a weak dependence on the ejecta mass, but it is quite sensitive to the ambient density because $R_{\mathrm{FS}} \propto M^{1/3}\rho^{-1/3}$ (McKee & Truelove, 1995). Therefore, objects surrounded by low-density media (e.g. RCW 86, SN 1006, and G344.7–0.1) clearly stand apart from those evolving in high density media (e.g. 3C 397, N103B, and Kepler): the former have large R_{FS} and low $E_{\mathrm{Fe_{K\alpha}}}$ centroids, while the latter have small R_{FS} and high $E_{\mathrm{Fe_{K\alpha}}}$. We note that the ages of these remnants differ from one another. In general, the densities we infer from simple comparisons to our models are in good agreement with detailed studies of individual objects. For instance, Someya et al. (2014) and Williams et al. (2014) determined $n_{\mathrm{amb}} \gtrsim 2.0\,\mathrm{cm^{-3}}$ for N103B, and Leahy & Ranasinghe (2016) found $n_{\mathrm{amb}} \sim 2-5\,\mathrm{cm^{-3}}$ for

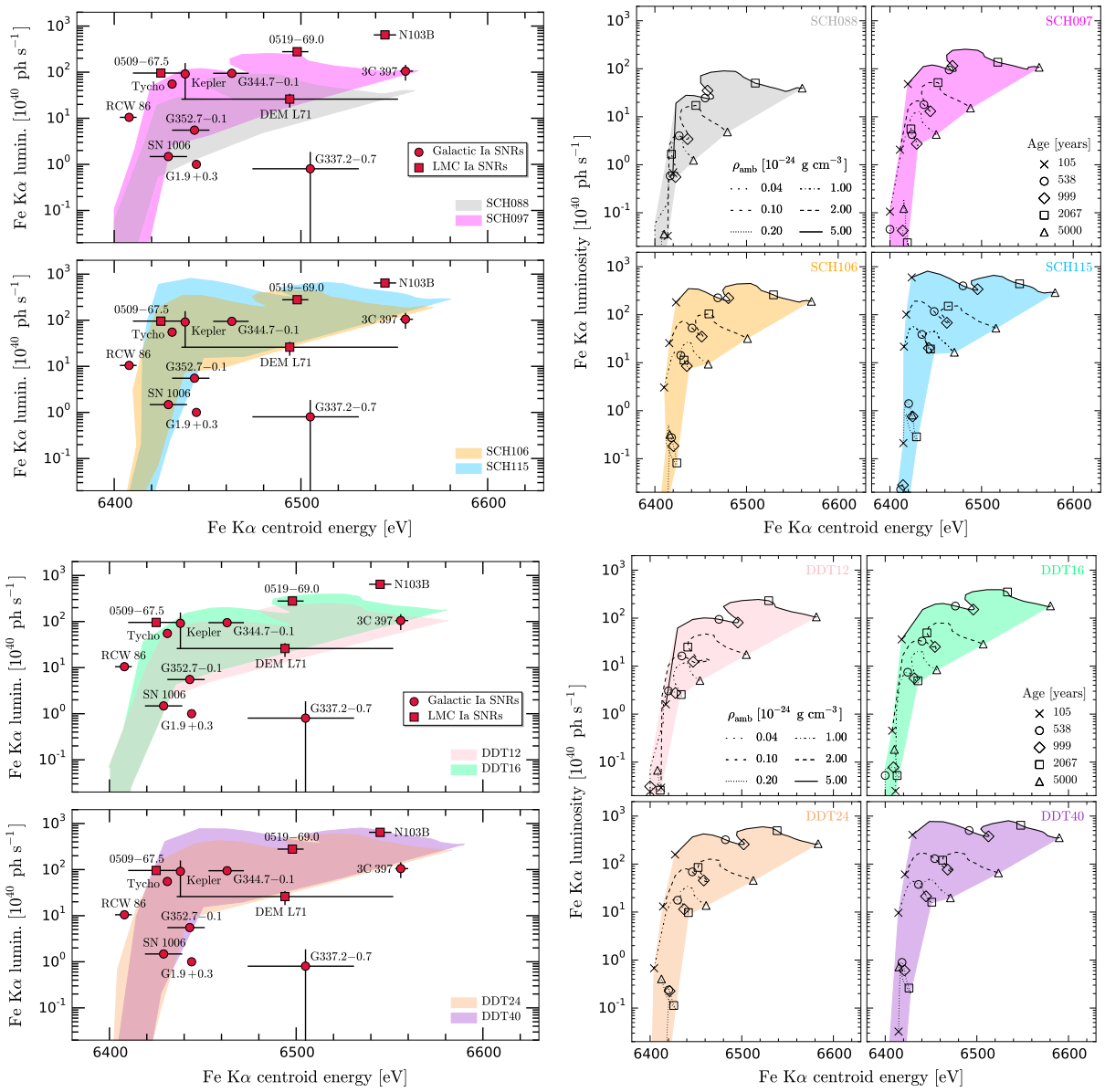

Figure 34: Left: Centroid energies and line luminosities of Fe Kα emission from various Type Ia SNRs in our Galaxy (circles) and the LMC (squares). The shaded regions depict the Fe Kα centroids and luminosities predicted by our theoretical sub-M_{Ch} and M_{Ch} models with various uniform ISM densities (SCH088: gray; SCH097: magenta; SCH106: orange; SCH115: blue; DDT12: pink; DDT16: green; DDT24: light brown; DDT40: purple). Right: Individual tracks for each model. The $L_{\mathrm{Fe_{K\alpha}}} - E_{\mathrm{Fe_{K\alpha}}}$ tracks corresponding to the two lowest ambient densities (ρ_{0p04}, ρ_{0p1}) do not appear in the plots because their $L_{\mathrm{Fe_{K\alpha}}}$ values are considerably small.

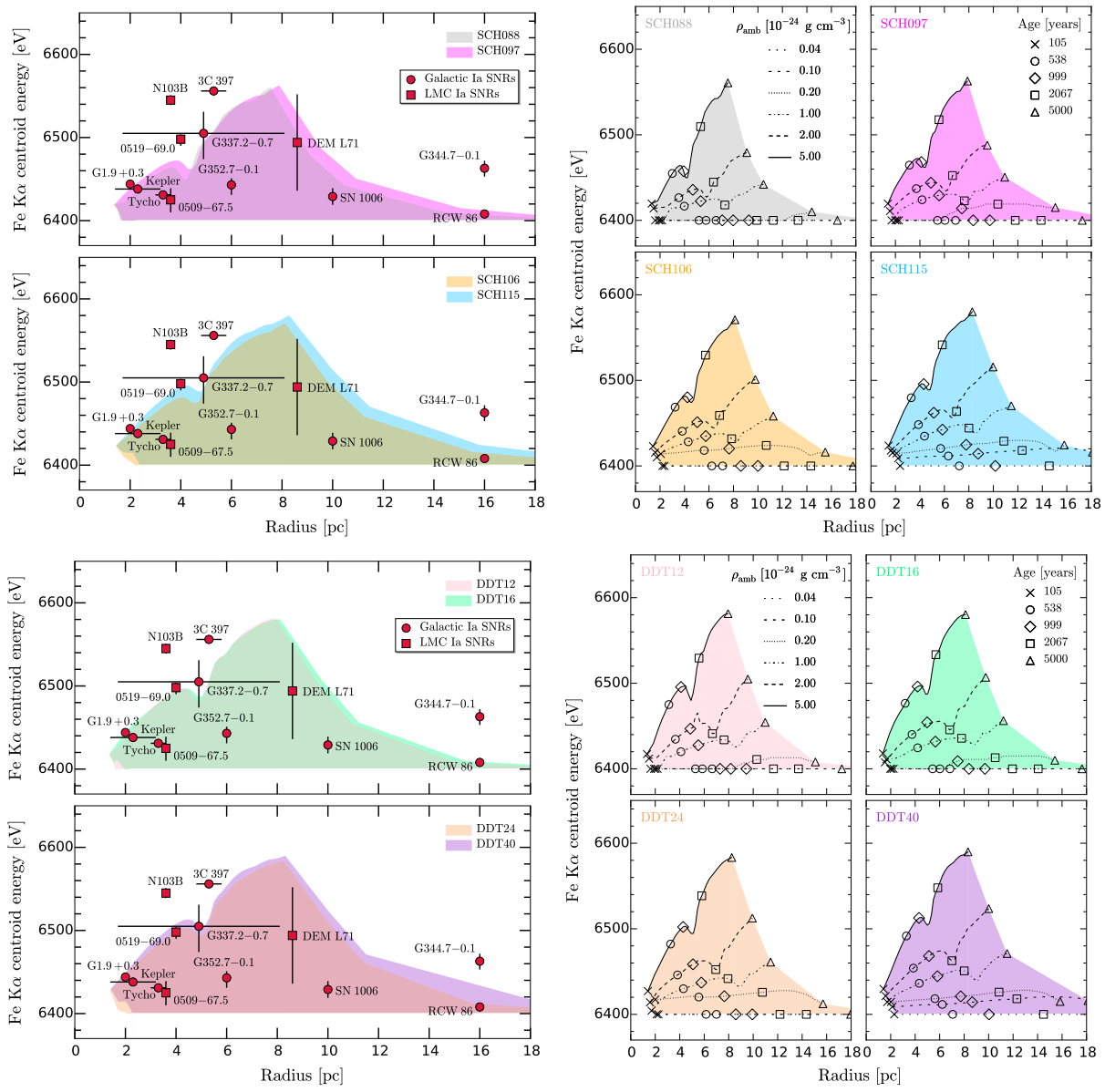

Figure 35: Fe Kα centroid energy versus forward shock radius for the Type Ia SNRs in our sample. The shaded regions correspond to the models shown in Figure 34.

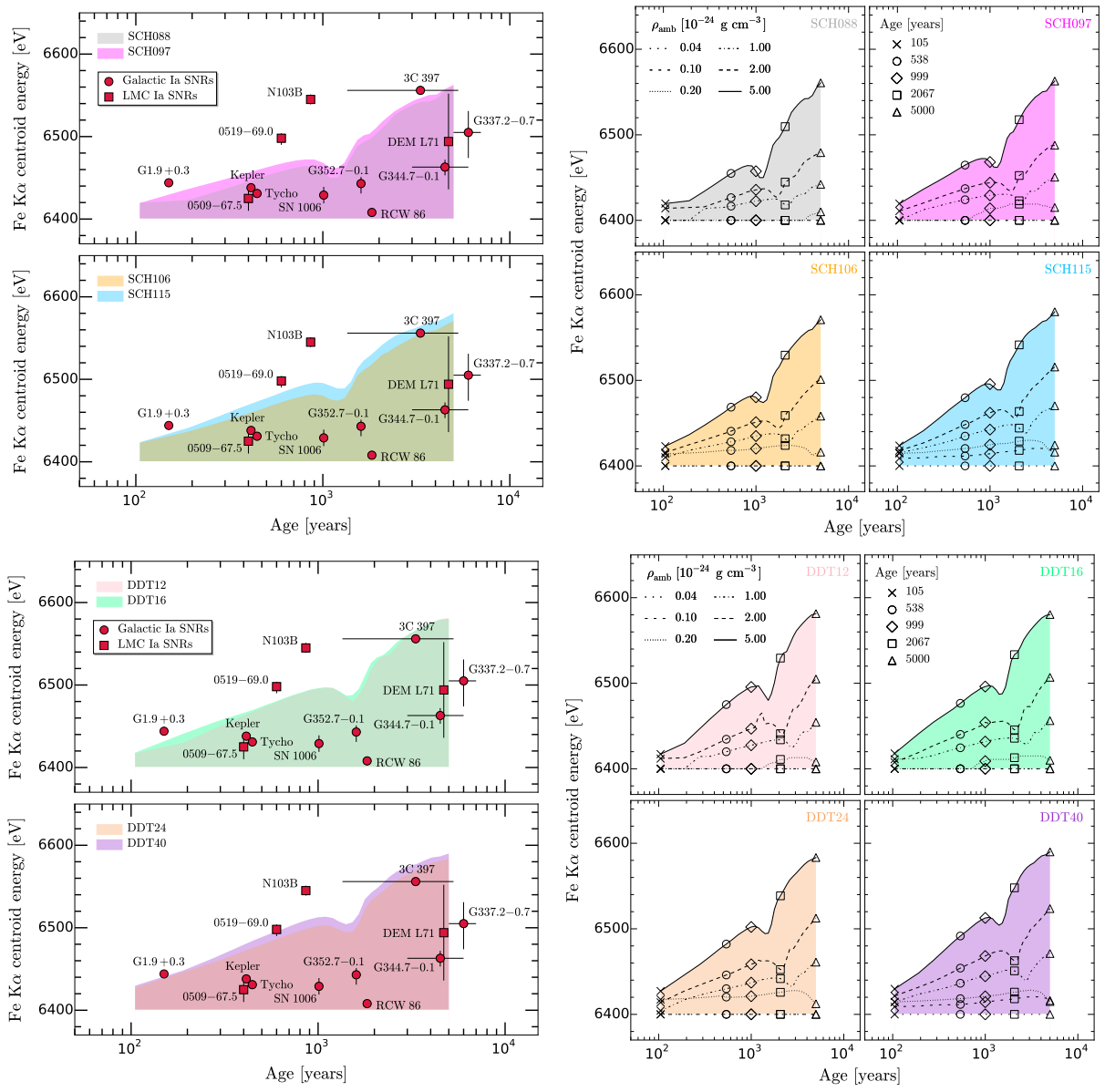

Figure 36: Fe Kα centroid energy versus expansion age for the Type Ia SNRs in our sample. The shaded regions correspond to the models shown in Figures 34 and 35.

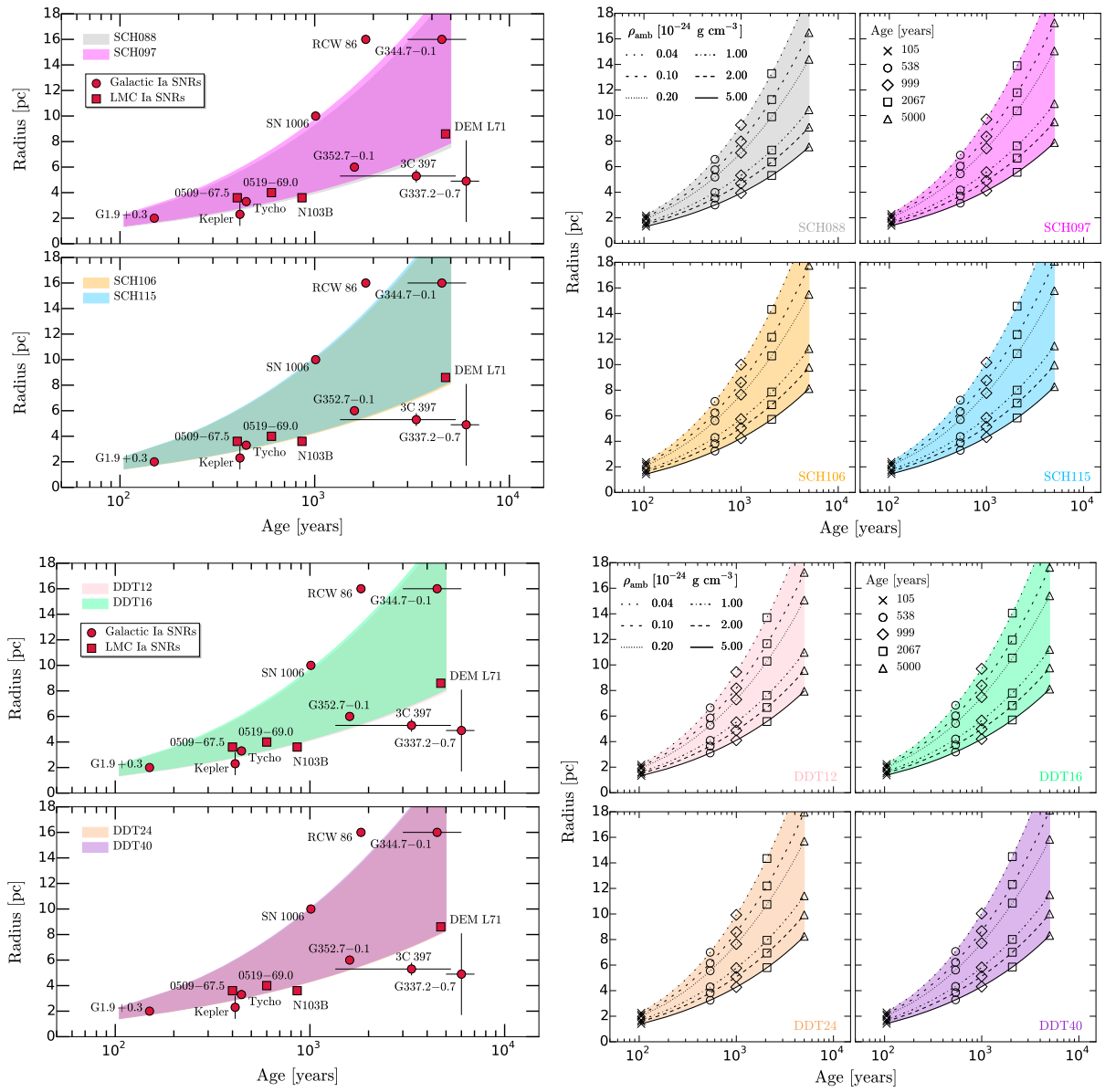

Figure 37: Forward shock radius versus expansion age for the Type Ia SNRs in our sample. The shaded regions correspond to the models shown in Figures 34, 35 and 36.

3C 397, which are close to the highest value of $\rho_{\rm amb}$ in our grid ($n_{\rm amb} = 3.01\,{\rm cm}^{-3}$).

For all the observables shown in Figures 34−37, the main sources of variation in the models are the ambient density and the expansion age. This implies that the details of the energetics and chemical composition in the supernova model, and in particular whether the progenitor was $\rm M_{Ch}$ or sub-$\rm M_{Ch}$, are not the main drivers for the bulk dynamics of Type Ia SNRs. This does not imply that our SNR models do not have the power to discriminate Type Ia SN explosion properties - detailed fits to the X-ray spectra of individual objects have shown that they can do this very well (e.g., Badenes et al., 2006, 2008a; Patnaude et al., 2012). However, the bulk SNR properties *on their own* are not very sensitive to the explosion properties, especially for objects whose expansion ages or distances are not well determined. To discriminate explosion properties, additional information needs to be taken into account, like specific line flux ratios (e.g. Si Kα / Fe Kα, S Kα / Fe Kα, and Ar Kα / Fe Kα), which can distinguish $\rm M_{Ch}$ from sub-$\rm M_{Ch}$ progenitors, or even better, detailed fits to the entire X-ray spectrum, which can reveal a wealth of information about the explosion (e.g., Badenes et al., 2006, 2008a; Patnaude et al., 2012). We defer these applications of our models to future work.

To evaluate the degree to which a particular model works well for a given SNR, it is important to examine *all* its bulk properties at the same time. By doing this, we can single out individual objects whose bulk dynamics cannot be reproduced by our models, modulo any uncertainties in the expansion age and distance. Not surprisingly, the SNR that shows the largest deviation from our models is RCW 86. This remnant is known to be expanding into a low-density cavity, presumably excavated by a fast, sustained outflow from the SN progenitor (Badenes et al., 2007; Williams et al., 2011; Broersen et al., 2014), and therefore its $R_{\rm FS}$ is too large for its expansion age and $E_{\rm Fe_{K\alpha}}$. In addition, its classification as a Type Ia SNR is still under debate (Gvaramadze et al., 2017). The Galactic SNR G344.7−0.1 also shows a similar deviation, albeit less strong, but this might be related to an overestimated distance and $R_{\rm FS}$ (Yamaguchi et al., 2012b, and references therein).

Among the objects interacting with low-density media, the size of SN 1006 is compatible with our lowest-density models, which agrees with the value $n_{\rm amb} \sim 0.03\,{\rm cm}^{-3}$ found by Yamaguchi et al. (2008), and its $E_{\rm Fe_{K\alpha}}$ and $L_{\rm Fe_{K\alpha}}$ are within the parameter space covered by

the models. We examine the case of SN 1006 in more detail in Section IV.3.2. Among the objects interacting with high density media, 3C 397 and N103B have $E_{\mathrm{Fe_{K\alpha}}}$ values that are too high for their physical sizes and expansion ages. This has been pointed out by Patnaude & Badenes (2017), and could be due to some sort of interaction with dense material, possibly (but not necessarily) a CSM modified by the SN progenitor (Safi-Harb et al., 2005; Williams et al., 2014; Li et al., 2017). Remarkably, the bulk dynamics of the Kepler SNR, which is often invoked as an example of CSM interaction in Type Ia SNRs (e.g., Reynolds et al., 2007; Chiotellis et al., 2012; Burkey et al., 2013) are compatible with a uniform ambient medium interaction, although a detailed spectral analysis suggests the presence of a small cavity around its progenitor system (Patnaude et al., 2012). Finally, the Galactic SNR G337.2−0.7 appears to be underluminous for its relatively high $E_{\mathrm{Fe_{K\alpha}}}$, but this could be due to the large uncertainty in its distance (Rakowski et al., 2006).

We summarize our comparisons between models and data in Figure 38, which shows $L_{\mathrm{Fe_{K\alpha}}}$, R_{FS} and expansion age for our $\mathrm{M_{Ch}}$ and sub-$\mathrm{M_{Ch}}$ models and for the SNRs as a function of $E_{\mathrm{Fe_{K\alpha}}}$, the only property that can be determined from the observations alone. We re-emphasize that our uniform ambient medium, spherically symmetric models, can reproduce the bulk dynamics of most Type Ia SNRs quite well. This suggests that, unlike CC SN progenitors, most Type Ia SN progenitors do not strongly modify their circumstellar environments, as previously noted by Badenes et al. (2007), Yamaguchi et al. (2014a), Patnaude & Badenes (2017), and other authors. This conclusion is in good agreement with the (hitherto unsuccessful) attempts to detect prompt X-ray and radio emission from extragalactic Type Ia SNe (Margutti et al., 2014; Chomiuk et al., 2016), but we note that SNR studies probe spatial and temporal scales ($\sim$ pc and $\sim 10^5$ years, Patnaude & Badenes, 2017) that are more relevant for the pre-SN evolution of Type Ia progenitor models. In this sense, the lack of a strongly modified CSM sets Type Ia SNRs clearly apart from CC SNRs (Yamaguchi et al., 2014a), which we also include in Figure 38 for comparison. The only two SNRs with well-determined properties that are clearly incompatible with our uniform ambient medium models are RCW 86 and N103B. These SNRs are probably expanding into some sort of modified CSM. In the case of RCW 86, the modification is very strong, and clearly due to the formation of a large cavity by the progenitor. In the case of N103B (and

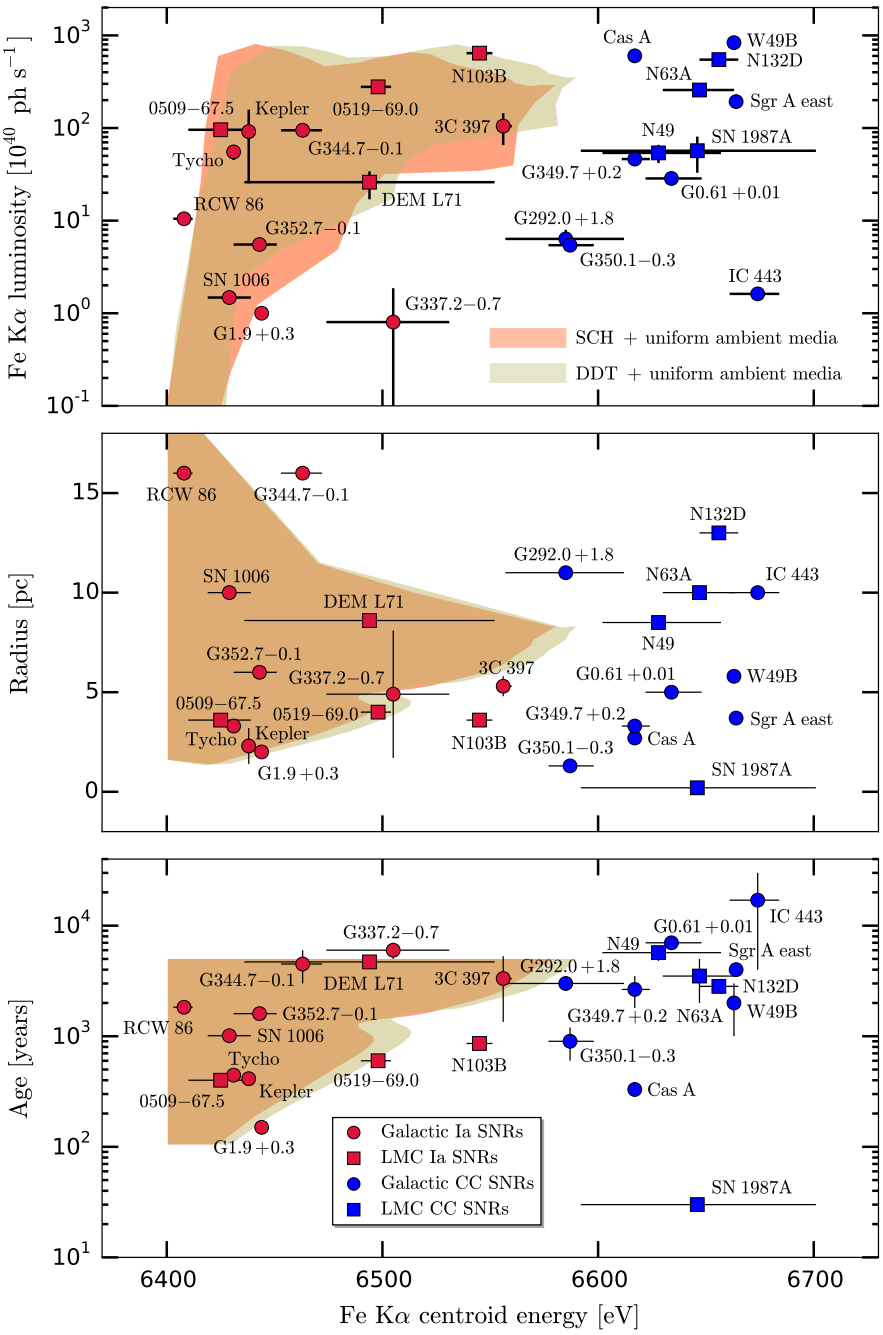

Figure 38: Fe Kα luminosity, radius and expansion age as a function of the Fe Kα centroid energy for Ia (red) and CC (blue) SNRs (Lovchinsky et al., 2011; Vogt & Dopita, 2011; Park et al., 2012; Tian & Leahy, 2014; Yamaguchi et al., 2014a, and references therein). For a more updated sample and further discussion, see Maggi & Acero (2017). The shaded regions depict the predictions from our theoretical M_{Ch} (khaki) and sub-M_{Ch} (dark orange) models with uniform ISM densities.

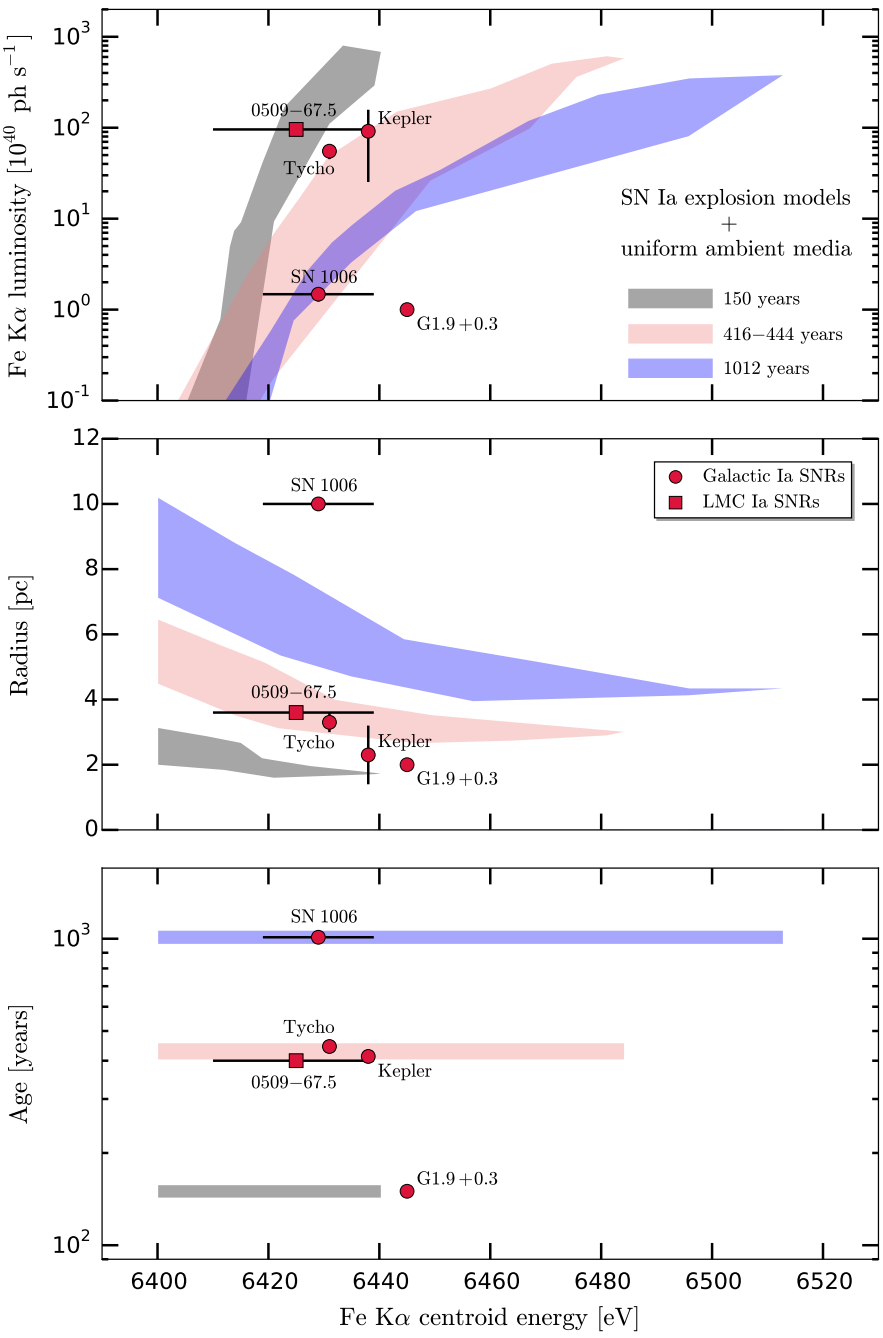

Figure 39: Fe Kα luminosity, radius and expansion age as a function of the Fe Kα centroid energy for G1.9+0.3, 0509−67.5, Kepler, Tycho, and SN 1006. The shaded regions depict the predictions from our theoretical M_{Ch} and sub-M_{Ch} models with uniform ISM densities for different expansion ages: 150 (black), 416−444 (light coral), and 1012 (blue) years.

perhaps also 3C 397), the modification could be due to some dense material left behind by the progenitor, but detailed models with nonuniform ambient media are required to verify or rule out this claim. In any case, it is clear from Figure 38 that the modification of the CSM by the progenitor in N103B must be much weaker than what is seen around typical CC SNRs.

IV.3.2 Type Ia SNRs: Remnants with well-determined expansion ages

A reduced subset of Type Ia SNRs have well-determined ages, either because they are associated with historical SNe (Kepler, Tycho, and SN 1006 have ages of 414, 446, and 1012 years, respectively), because they have well-observed light echoes (0509−67.5 has an age of $\sim$ 400 years, Rest et al., 2008b), or because their dynamics put very strong constraints on their age (G1.9+0.3 has an age of $\sim$ 150 years, Reynolds et al., 2008; Carlton et al., 2011; De Horta et al., 2014; Sarbadhicary et al., 2017). These objects are particularly valuable benchmarks for our models, because their known ages remove an important source of uncertainty in the interpretation of their bulk dynamics.

We perform more detailed comparisons for this set of objects by taking our models at 150 years (G1.9+0.3), 416−444 years (0509−67.5, Kepler, and Tycho) and 1012 years (SN 1006). Figure 39 shows the same quantities as Figure 38, but here we display the parameter space covered by our M_{Ch} and sub-M_{Ch} models at all densities for each of the three age ranges mentioned above. The models at 416−444 years can reproduce the observed properties of Kepler, Tycho, and 0509−67.5 quite well, even with the added constraints from the known expansion ages, but we stress that detailed fits to the entire X-ray spectra might reveal additional information (see Patnaude et al. 2012 for Kepler, Slane et al. 2014 for Tycho). In any case, we can say that the bulk dynamics of these three objects disfavor variations from a uniform medium interaction as large as those seen in typical CC SNRs. We note that we have made no attempt to quantify the extent of the deviation from a uniform ambient medium that could be accommodated while still yielding results that are consistent with the observations, as it is beyond the scope of the present work.

For SN 1006, $R_{\rm FS}$, $E_{\rm Fe K\alpha}$, and $L_{\rm Fe K\alpha}$ are well reproduced by our models at 1012 years;

though, given its surrounding ambient density and physical size, $E_{\mathrm{Fe_{K\alpha}}}$ is larger than can be explained by a uniform ambient medium interaction. For G1.9+0.3, R_{FS} and $L_{\mathrm{Fe_{K\alpha}}}$ are close to the values predicted by our models at 150 years, but $E_{\mathrm{Fe_{K\alpha}}}$ is too high to be reconciled with a uniform ambient medium interaction. In both cases, the bulk properties of the SNRs might indicate an early interaction with some sort of modified CSM. For SN 1006, this might be a low-density cavity, perhaps smaller in size than the SNR. For G1.9+0.3, a thin, dense shell that changed the ionization state without strongly affecting the dynamics might have been involved, as suggested by Chakraborti et al. (2016). In both cases, a detailed exploration of the parameter space for CSM interaction in Type Ia SNRs is required to confirm or rule out specific scenarios.

IV.4 CONCLUSIONS

We have presented a new grid of one-dimensional models for young SNRs arising from the interaction between Type Ia explosions with different $\mathrm{M_{Ch}}$ and sub-$\mathrm{M_{Ch}}$ progenitors and a uniform ambient medium. We have generated synthetic X-ray spectra for each model at different expansion ages, separating the reverse and forward shock contributions. Our model spectra are publicly available, and can easily be convolved with the spectral responses of current and future X-ray missions like *Chandra*, *XRISM*, and *Athena*. We have studied the bulk spectral and dynamical properties of our models (Fe Kα centroid energies and luminosities, radii, and expansion ages), and have found that they provide an excellent match to the observations of most known Type Ia SNRs, indicating that the majority of SN Ia progenitors do not seem to substantially modify their surroundings on scales of a few parsecs, at least in comparison with CC SN progenitors. In our models, the ambient medium density and expansion age are the main contributors to the diversity of the bulk SNR properties, but detailed fits to X-ray spectra can discriminate progenitor properties. We have also identified a few objects that cannot be easily reproduced by SNR models with a uniform ambient medium interaction, notably RCW 86, which is known to be a cavity explosion, and N103B, which is probably interacting with dense material of some sort. A

detailed exploration of the parameter space for CSM interaction in Type Ia SNRs is required to gain further insight from these objects.

Support for this work has been provided by the Chandra Theory award TM8-19004X. H.M.-R., C.B., and S.P. are funded by the NASA ADAP grant NNX15AM03G S01. H.M.-R. also acknowledges support from a PITT PACC and a Zaccheus Daniel Predoctoral Fellowship. D.J.P. acknowledges support from the Chandra Theory Program NASA/TM6-17003X and the NASA contract NAS8-03060. S.-H.L. is supported by the Kyoto University Foundation (grant No. 203180500017). E.B. acknowledges funding from the MINECO-FEDER grant AYA2015-63588-P. The authors wish to thank the Lorentz Center and the organizers and participants of the workshop "Observational Signatures of Type Ia Supernova Progenitors (III)" for stimulating discussions that helped finish this work. We also thank Karin Sandstrom and Rachel Bezanson for assistance with references regarding the Galactic hydrogen density probability distribution function. This research has made extensive use of NASA's Astrophysics Data System (ADS, http://adswww.harvard.edu/).

V CONCLUSIONS

I will employ the word "we" as opposed to "I" to discuss the results of my PhD in order to give justice to my collaborators, without whom this research would have not been carried out until the end.

We have studied several key aspects of the models and observations of SNe Ia and their SNRs. We have focused on the neutronization processes in SN Ia progenitors and on the X-ray bulk properties of Ia SNRs.

Using the `MESA` stellar evolution code, we calculated a grid of carbon simmering models in the SD channel with different accretion rates, WD masses and WD central temperatures that predict a roughly uniform, low simmering floor independent of progenitor metallicity. We showed that this would hinder the observational detection of neutron-rich Ia ejecta coming from simmering for metallicities $\gtrsim 1/3\, Z_{\odot}$, which makes Ia SNRs in the Large Magellanic Cloud an ideal target given the intrinsically low metallicities in the disk of this galaxy ($\approx 0.2 - 0.6\, Z_{\odot}$).

We reduced the *Suzaku* X-ray spectra of Ia SNRs and modeled their X-ray emission using the `XSPEC` code in order to retrieve elemental mass ratios. We analyzed the 3−5 keV range in order to measure $\mathrm{M_{Ca}/M_S}$ for the remnants in our sample, as it is linearly proportional to the neutron excess in the ejecta, is only affected by the progenitor's metallicity and simmering, and the S and Ca Kα lines are bright enough in most remnants. We got sufficiently low uncertainties to establish meaningful comparisons with Ia nucleosynthesis models for five remnants: Tycho, Kepler, 3C 397 and G337.2−0.7 in the Milky Way, and N103B in the Large Magellanic Cloud. We concluded that, when compared to the metallicity distribution functions of both galaxies, 3C 397, G337.2−0.7 and N103B are outliers, having an extremely high neutron-rich content in their ejecta. Discarding progenitor metallicity,

carbon simmering is the only known process that could explain these results. However, our simmering predictions are unable to account for these measurements, so either there is a fourth unidentified source of neutronization in SN Ia progenitors (in addition to progenitor metallicity, simmering and the n-NSE burning regime), or our models cannot fully describe simmering. The most straightforward explanation for this extremely neutron-rich material in SN Ia ejecta is that a non-negligible fraction of SNe Ia explode as near-M_{Ch} events.

We ran hydrodynamical models of expanding Ia SNRs into a uniform, undisturbed ambient medium during the adiabatic and the Sedov phases using the `ChN` code. Our model grid comprises different M_{Ch} and sub-M_{Ch} progenitors, ambient densities and expansion ages. From the code output, we generated synthetic X-ray spectra by means of the `PyAtomDB` emissivity code and reconciled these predictions with measurements from real *Suzaku* X-ray spectra. We focused on the bulk properties: Fe Kα centroid energy and luminosity, radius, and expansion age. We found that the bulk properties of most Ia SNRs can be described by our uniform ambient models, suggesting that SN Ia progenitors, when compared to CC progenitors, do not strongly modify their surrounding medium on scales of a few pc. In addition, we showed that the expansion age and ambient density have the strongest influence on the variation of the bulk properties.

Our work has shed some light on a few key aspects of a very complex problem. Future studies can take advantage of our analysis and help solve the Type Ia SN progenitor problem. Our follow-up paper on carbon simmering (Schwab et al., 2017) demonstrated that the current understanding of convective mixing in one-dimensional models has room for improvement, and also, that it has a strong impact on the increase in the neutron excess during simmering. Our *Suzaku* measurements of the neutron excess in Type Ia SNRs and our synthetic X-ray spectra generated using *XRISM* response files showed that future X-ray missions are needed to improve the quality of the available data, and therefore, our understanding about the progenitors of SNe Ia. Furthermore, the extreme wealth of our grid of synthetic X-ray spectra allows for thorough comparisons with real observations of Type Ia SNRs, far beyond our preliminary analysis of the bulk properties. By means of these research projects, we might soon be able to fully understand how neutron-rich isotopes are created during SN Ia nucleosynthesis and to elucidate where SNe Ia specifically come from.

APPENDIX

A.1 MODIFICATIONS TO MESA AND KEY WEAK REACTIONS

In this appendix, we describe our use and extension of MESA's on-the-fly weak rates capabilities.[1] An accurate treatment of the key weak reaction rates is necessary to resolve the effects of the Urca process and to include the effects of neutronization due to the electron-capture reactions during simmering. In order to illustrate their importance, Figure 40 shows the differences between our work and a MESA calculation which does not include these choices and changes.

A.1.1 Weak rates for $A = 23$, 24, and 25

Coarse tabulations of weak rates can severely underestimate cooling by the Urca process (e.g., Toki et al., 2013; Paxton et al., 2015). To circumvent this limitation, we use MESA's capability to calculate weak reaction rates on-the-fly. We use input nuclear data drawn from the MESA test suite problem 8.8M_urca, which includes Urca-process cooling by the ^{25}Mg–^{25}Na and ^{23}Na–^{23}Ne Urca pairs. This choice allows us to include the significant and often neglected effects of local Urca process cooling via these isotopes (see Section II.2.2). As indicated in Figure 40, the decrease in temperature associated with the Urca-process cooling is not seen in a calculation that does not make use of the on-the-fly rates.

The Urca-process cooling leads to an increase in the maximum central density reached

[1] We incorporate fixes that correct errors present in Paxton et al. (2015), as documented in the published erratum (Paxton et al., 2016).

(see Figure 6). In some cases, this approaches or exceeds the threshold density for electron capture on ^{24}Mg. Therefore, we include weak reactions involving ^{24}Mg and its daughters using input nuclear data drawn from the `MESA` test suite problem `wd_aic`.

The ^{23}Na(e$^-$, ν_e)^{23}Ne reaction plays a key role during the simmering phase (see Section II.2.1). As the convection zone grows, it eventually spans many density scale heights, with electron captures favored in regions above the threshold density and beta decays favored in regions below it. While the convective zone remains fully mixed, the overall neutronization is determined by the mass-weighted average of the reaction rates across the convection zone. Interpolation in the coarse `weaklib` tables leads to a systematic underestimate of the ^{23}Ne beta-decay rates. Figure 40 shows that a calculation using the on-the-fly rates exhibits less neutronization once the outer edge of the convection zone grows beyond the threshold density of ^{23}Na.

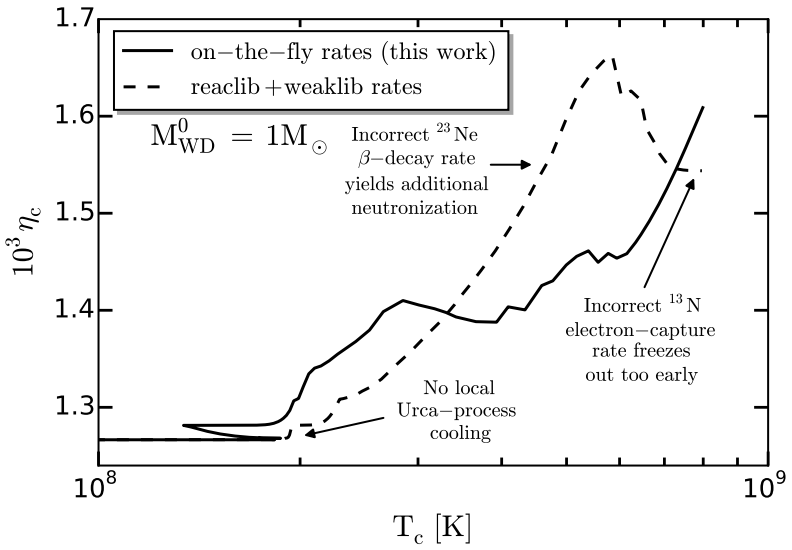

Figure 40: Neutron excess as a function of central temperature for the fiducial model discussed Section II.4.1 with (black line) and without the use of the extended on-the-fly rates capabilities (dashed line).

A.1.2 Rate of electron capture on ^{13}N

In an unmodified version of MESA r7624, the reaction linking ^{13}N to ^{13}C (`r_n13_wk_c13`) is drawn from JINA reaclib (Cyburt et al., 2010). This reaction rate includes only positron emission and does not include the electron-capture reaction $^{13}\mathrm{N}(\mathrm{e}^-,\nu_\mathrm{e})^{13}\mathrm{C}$. At the characteristic simmering densities ($\rho \sim 10^9$ g cm^{-3}), the electron capture rate is ~ 10 s^{-1}, a factor of $\sim 10^4$ more rapid than the positron emission rate. If the proper rate is not included, late in the simmering phase, ^{13}N to ^{13}C will freeze out. This is illustrated on the right in Figure 40, where the neutronization ceases to increase when MESA's default `r_n13_wk_c13` rate is used.

The on-the-fly reaction rate framework described in Paxton et al. (2015) is limited to transitions with $Q < 0$, where Q is the energy difference (including rest mass) between the two states. The energy difference between the ground states of ^{13}N and ^{13}C is $Q = 2.22$ MeV so, in order to incorporate this rate, we extend the on-the-fly weak rate implementation in MESA to include rates with $Q > 0$. In the notation of Paxton et al. (2015), the rate for such a transition can be written as

$$\lambda_{ij} = \frac{\ln 2}{(ft)_{ij}} \frac{\exp(\pi\alpha Z)}{(m_\mathrm{e}c^2)^5} \int_{m_\mathrm{e}c^2}^{\infty} \frac{E_\mathrm{e}^2 (E_\mathrm{e} + Q_{ij})^2}{1 + \exp[\beta(E_\mathrm{e} - \mu_\mathrm{e})]} dE_\mathrm{e} \ . \tag{6}$$

This integral can also be rewritten in terms of Fermi-Dirac integrals as in Schwab et al. (2015), and as such, the extension is straightforward. A patch demonstrating this implementation will be made available along with the inlists used in this work.

We include the effects of two electron-capture transitions, drawing nuclear energy levels from Ajzenberg-Selove (1991) and (ft)-values from the recent experimental results of Zegers et al. (2008). These values are shown in Table 6.

A.2 CONVERGENCE OF THE MESA MODELS AND OVERSHOOTING

In this appendix, we address the numerical convergence of our models and the effects of overshooting. During the phase where the WD mass is in excess of $1.3 M_\odot$, which includes

Table 6: The transitions used in the on-the-fly $^{13}\mathrm{N}(\mathrm{e}^{-},\nu_{\mathrm{e}})^{13}\mathrm{C}$ rate calculation. E_{i} and E_{f} are respectively the excitation energies (in MeV) of the initial and final states, relative to the ground state. J_{i}^{π} and J_{f}^{π} are the spins and parities of the initial and final states. (ft) is the comparative half-life in seconds.

E_{i}	J_{i}^{π}	E_{f}	J_{f}^{π}	$\log(ft)$
0.000	$1/2^{-}$	0.000	$1/2^{-}$	3.665
0.000	$1/2^{-}$	3.685	$3/2^{-}$	3.460

both the local Urca-process cooling and simmering phases, the default spatial resolution of our models is specified by the control

```
mesh_delta_coeff = 1.0     .
```

The default temporal resolution of our models is specified by imposing a maximum allowed fractional change in the central density and temperature per timestep, via the controls

```
delta_lgRho_cntr_hard_limit = 1d-3
delta_lgT_cntr_hard_limit = 3d-3     .
```

In order to confirm that our results are robust, we repeated our fiducial calculation, but used these controls to increase the spatial resolution by a factor of ≈ 6 and the temporal resolution by a factor of ≈ 3. Figure 41 compares our fiducial model (Section II.4.1) to this model with increased temporal and spatial resolution. The most conspicuous differences occur for T_{c} between 3×10^{8} K and 6×10^{8} K. It is primarily during this phase that the convective Urca-process is occurring. As mentioned in Section II.2.2, limitations imposed by the 1D mixing length theory of convection prevent fully consistent modeling of this phase. Thus, the fine details of the observed behavior during this phase are unlikely to be physically meaningful. As simmering nears its end and the heating timescale falls, the Urca-process reactions begin to freeze out. Once this occurs, the models return to a smooth evolution and to good agreement with each other.

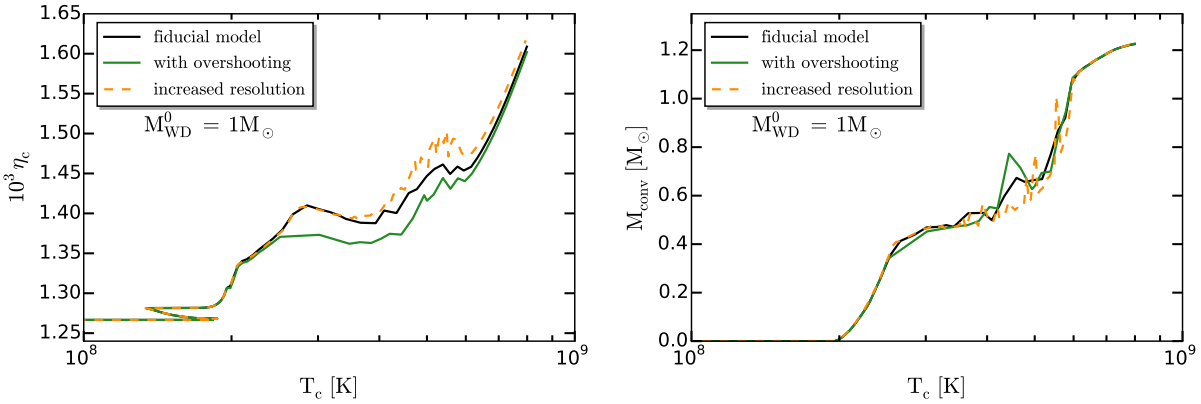

Figure 41: Comparison of results from the fiducial model (black curve), a model with overshooting (green curve) and a model with increased spatial and temporal resolution (dashed, orange curve). Left: Central neutron excess. Right: Mass of the convective core. The primary differences occur for T_c between 3×10^8 K and 6×10^8 K. During this phase, our limited treatment of the convective Urca-process makes fine details of the models unlikely to be physically meaningful. By the end of the evolution, the models return to a smooth evolution and to good agreement with each other.

Table 7: Comparison of results from the fiducial model (top), a different run with overshooting (middle) and a model with increased spatial and temporal resolution (bottom). The number of cells at the end of the run and the total number of time steps are shown in the last two columns.

Descrip.	$\log T_{\rm c}^{\rm sim}$ [K]	$\log \rho_{\rm c}^{\rm sim}$ [g cm^{-3}]	$\Delta {\rm t}^{\rm sim}$ [kyr]	t [Myr]	$\log \rho_{\rm c}$ [g cm^{-3}]	$M_{\rm WD}$ [$M_\odot$]	$M_{\rm conv}$ [$M_\odot$]	$10^3 \eta_{\rm c}$	$10^3(\eta_{\rm c} - \eta_{\rm c,0})$	# Zones	Time steps
Fiducial	8.29	9.61	30.2	3.86	9.52	1.386	1.225	1.61	0.34	1149	1677
Oversh.	8.29	9.61	29.6	3.86	9.52	1.386	1.227	1.60	0.34	1144	1640
Incr. res.	8.29	9.61	31.0	3.86	9.53	1.386	1.225	1.62	0.35	7235	5343

The models shown in the body of the paper use the Schwarzschild convective criterion and no overshooting. Figure 41 also shows the results of our fiducial model with overshooting at the outer boundary of the central convective zone, added by means of the controls

```
overshoot_f_above_burn_z_core = 0.010
overshoot_f0_above_burn_z_core = 0.005  .
```

Again, the primary differences occur for $T_{\rm c}$ between 3×10^8 K and 6×10^8 K, but the model returns to good agreement with the fiducial model by the end of simmering. In Table A.2 we compare the values of the quantities of interest at the end of simmering (the same quantities compiled in Tables 8–10) for our fiducial model, the model with increased resolution, and the model including the effects of overshooting. We find sub-to-few per cent level agreement in all quantities of interest, giving us confidence that our results are robust.

Table 8: Results for the models without cooling.

Z	$M^0_{\rm WD}$	$\dot{M}$	$\log T_{\rm c}^{\rm sim}$	$\log \rho_{\rm c}^{\rm sim}$	$\Delta {\rm t}^{\rm sim}$	t	$\log \rho_{\rm c}$	$M_{\rm WD}$	$M_{\rm conv}$	$10^3\eta_{\rm c}$	$10^3(\eta_{\rm c}-\eta_{\rm c,0})$
$[Z_\odot]$	$[M_\odot]$	$[M_\odot\,{\rm yr}^{-1}]$	[K]	$[{\rm g\,cm}^{-3}]$	[kyr]	[Myr]	$[{\rm g\,cm}^{-3}]$	$[M_\odot]$	$[M_\odot]$		
0.01	0.7	10^{-6}	8.43	9.38	4.76	0.680	9.33	1.380	1.178	0.34	0.33
0.01	0.85	10^{-6}	8.43	9.38	4.49	0.529	9.33	1.380	1.182	0.34	0.32
0.01	1.0	10^{-6}	8.43	9.38	4.72	0.379	9.33	1.380	1.183	0.33	0.31
0.01	0.7	10^{-7}	8.36	9.50	32.5	6.84	9.41	1.384	1.246	0.33	0.32
0.01	0.85	10^{-7}	8.35	9.49	35.1	5.34	9.41	1.384	1.251	0.33	0.32
0.01	1.0	10^{-7}	8.36	9.50	33.6	3.84	9.41	1.384	1.251	0.33	0.31
0.01	0.7	5×10^{-8}	8.32	9.56	56.0	13.7	9.46	1.387	1.256	0.34	0.32
0.01	0.85	5×10^{-8}	8.33	9.56	49.3	10.7	9.46	1.387	1.257	0.33	0.32
0.01	1.0	5×10^{-8}	8.32	9.56	52.7	7.73	9.45	1.386	1.259	0.33	0.31
0.10	0.7	10^{-6}	8.42	9.39	4.56	0.681	9.34	1.381	1.175	0.45	0.32
0.10	0.85	10^{-6}	8.42	9.39	4.47	0.531	9.34	1.381	1.177	0.45	0.32
0.10	1.0	10^{-6}	8.42	9.39	4.56	0.380	9.35	1.381	1.176	0.44	0.31
0.10	0.7	10^{-7}	8.34	9.54	29.2	6.86	9.44	1.386	1.242	0.45	0.32
0.10	0.85	10^{-7}	8.34	9.54	29.2	5.35	9.44	1.386	1.242	0.45	0.32
0.10	1.0	10^{-7}	8.33	9.53	31.5	3.85	9.44	1.386	1.242	0.44	0.31

Table 8: Results for the models without cooling (continued).

Z	$M^0_{\rm WD}$	$\dot{M}$	$\log T_{\rm c}^{\rm sim}$	$\log \rho_{\rm c}^{\rm sim}$	$\Delta {\rm t}^{\rm sim}$	t	$\log \rho_{\rm c}$	$M_{\rm WD}$	$M_{\rm conv}$	$10^3\eta_{\rm c}$	$10^3(\eta_{\rm c}-\eta_{\rm c,0})$
$[Z_\odot]$	$[M_\odot]$	$[M_\odot\,{\rm yr}^{-1}]$	[K]	$[{\rm g\,cm}^{-3}]$	[kyr]	[Myr]	$[{\rm g\,cm}^{-3}]$	$[M_\odot]$	$[M_\odot]$		
0.10	0.7	5×10^{-8}	8.30	9.60	49.5	13.8	9.49	1.388	1.249	0.46	0.33
0.10	0.85	5×10^{-8}	8.30	9.59	55.9	10.8	9.49	1.388	1.250	0.46	0.33
0.10	1.0	5×10^{-8}	8.30	9.60	50.2	7.75	9.49	1.388	1.253	0.46	0.33
0.33	0.7	10^{-6}	8.41	9.40	4.53	0.681	9.35	1.381	1.173	0.73	0.31
0.33	0.85	10^{-6}	8.41	9.40	4.59	0.531	9.36	1.381	1.170	0.73	0.31
0.33	1.0	10^{-6}	8.41	9.40	4.77	0.380	9.36	1.380	1.173	0.73	0.31
0.33	0.7	10^{-7}	8.33	9.55	29.3	6.86	9.46	1.386	1.238	0.73	0.31
0.33	0.85	10^{-7}	8.32	9.55	32.5	5.36	9.46	1.386	1.240	0.73	0.31
0.33	1.0	10^{-7}	8.32	9.55	31.8	3.85	9.46	1.386	1.242	0.73	0.31
0.33	0.7	5×10^{-8}	8.29	9.61	55.9	13.8	9.50	1.388	1.246	0.74	0.32
0.33	0.85	5×10^{-8}	8.29	9.61	54.2	10.8	9.50	1.388	1.245	0.75	0.32
0.33	1.0	5×10^{-8}	8.29	9.61	55.1	7.75	9.51	1.388	1.249	0.74	0.32
1.00	0.7	10^{-6}	8.39	9.45	4.50	0.681	9.40	1.381	1.160	1.58	0.31
1.00	0.85	10^{-6}	8.40	9.46	4.24	0.531	9.41	1.381	1.159	1.57	0.30
1.00	1.0	10^{-6}	8.40	9.46	4.17	0.381	9.41	1.381	1.163	1.57	0.30
1.00	0.7	10^{-7}	8.29	9.61	29.4	6.86	9.52	1.386	1.225	1.61	0.35

Table 8: Results for the models without cooling (continued).

Z	$M^0_{\rm WD}$	$\dot{M}$	$\log T_{\rm c}^{\rm sim}$	$\log \rho_{\rm c}^{\rm sim}$	$\Delta {\rm t}^{\rm sim}$	t	$\log \rho_{\rm c}$	$M_{\rm WD}$	$M_{\rm conv}$	$10^3 \eta_{\rm c}$	$10^3(\eta_{\rm c} - \eta_{\rm c,0})$
$[Z_\odot]$	$[M_\odot]$	$[M_\odot\,{\rm yr}^{-1}]$	[K]	$[{\rm g\,cm}^{-3}]$	[kyr]	[Myr]	$[{\rm g\,cm}^{-3}]$	$[M_\odot]$	$[M_\odot]$		
1.00	0.85	10^{-7}	8.29	9.61	29.8	5.36	9.52	1.386	1.223	1.61	0.34
1.00	1.0	10^{-7}	8.29	9.61	30.2	3.86	9.52	1.386	1.225	1.61	0.34
1.00	0.7	5×10^{-8}	Convection zone splits during simmering								
1.00	0.85	5×10^{-8}	Convection zone splits during simmering								
1.00	1.0	5×10^{-8}	Convection zone splits during simmering								
2.79	0.7	10^{-6}	8.37	9.55	3.33	0.679	9.49	1.379	1.131	3.86	0.34
2.79	0.85	10^{-6}	8.37	9.55	3.64	0.529	9.49	1.379	1.136	3.86	0.34
2.79	1.0	10^{-6}	8.37	9.55	3.62	0.378	9.49	1.378	1.136	3.86	0.34
2.79	0.7	10^{-7}	Convection zone splits during simmering								
2.79	0.85	10^{-7}	Convection zone splits during simmering								
2.79	1.0	10^{-7}	Convection zone splits during simmering								
2.79	0.7	5×10^{-8}	Convection zone splits during simmering								
2.79	0.85	5×10^{-8}	Convection zone splits during simmering								
2.79	1.0	5×10^{-8}	Convection zone splits during simmering								

Table 9: Results for the models with a cooling age of 1 Gyr.

Z	$M^0_{\rm WD}$	$\dot{M}$	$\log T_{\rm c}^{\rm sim}$	$\log \rho_{\rm c}^{\rm sim}$	$\Delta {\rm t}^{\rm sim}$	t	$\log \rho_{\rm c}$	$M_{\rm WD}$	$M_{\rm conv}$	$10^3\eta_{\rm c}$	$10^3(\eta_{\rm c}-\eta_{\rm c,0})$
$[Z_\odot]$	$[M_\odot]$	$[M_\odot\,{\rm yr}^{-1}]$	[K]	$[{\rm g\,cm}^{-3}]$	[kyr]	[Myr]	$[{\rm g\,cm}^{-3}]$	$[M_\odot]$	$[M_\odot]$		
0.01	0.7	10^{-6}				Off-center carbon ignition					
0.01	0.85	10^{-6}				Off-center carbon ignition					
0.01	1.0	10^{-6}				Off-center carbon ignition					
0.01	0.7	10^{-7}	8.36	9.50	32.5	6.84	9.41	1.384	1.248	0.33	0.32
0.01	0.85	10^{-7}	8.36	9.50	33.8	5.34	9.41	1.384	1.250	0.33	0.31
0.01	1.0	10^{-7}	8.35	9.57	17.0	3.87	9.46	1.387	1.242	0.33	0.31
0.01	0.7	5×10^{-8}	8.32	9.56	55.2	13.7	9.46	1.387	1.256	0.34	0.32
0.01	0.85	5×10^{-8}	8.32	9.56	52.4	10.7	9.46	1.387	1.257	0.33	0.32
0.01	1.0	5×10^{-8}	8.32	9.57	46.2	7.72	9.46	1.387	1.258	0.33	0.31
0.10	0.7	10^{-6}				Off-center carbon ignition					
0.10	0.85	10^{-6}				Off-center carbon ignition					
0.10	1.0	10^{-6}				Off-center carbon ignition					
0.10	0.7	10^{-7}	8.33	9.53	31.6	6.85	9.44	1.386	1.242	0.45	0.32
0.10	0.85	10^{-7}	8.34	9.54	29.0	5.36	9.44	1.386	1.243	0.45	0.32
0.10	1.0	10^{-7}	8.32	9.58	21.2	3.87	9.48	1.387	1.238	0.45	0.32

Table 9: Results for the models with a cooling age of 1 Gyr (continued).

Z	$M^0_{\rm WD}$	$\dot{M}$	$\log T_{\rm c}^{\rm sim}$	$\log \rho_{\rm c}^{\rm sim}$	$\Delta {\rm t}^{\rm sim}$	t	$\log \rho_{\rm c}$	$M_{\rm WD}$	$M_{\rm conv}$	$10^3\eta_{\rm c}$	$10^3(\eta_{\rm c}-\eta_{\rm c,0})$
$[Z_\odot]$	$[M_\odot]$	$[M_\odot\,{\rm yr}^{-1}]$	[K]	$[{\rm g\,cm}^{-3}]$	[kyr]	[Myr]	$[{\rm g\,cm}^{-3}]$	$[M_\odot]$	$[M_\odot]$		
0.10	0.7	5×10^{-8}	8.30	9.59	52.7	13.8	9.49	1.388	1.250	0.46	0.33
0.10	0.85	5×10^{-8}	8.30	9.59	52.1	10.8	9.49	1.388	1.250	0.46	0.33
0.10	1.0	5×10^{-8}	8.29	9.60	52.1	7.76	9.50	1.388	1.252	0.46	0.33
0.33	0.7	10^{-6}				Off-center carbon ignition					
0.33	0.85	10^{-6}				Off-center carbon ignition					
0.33	1.0	10^{-6}				Off-center carbon ignition					
0.33	0.7	10^{-7}	8.33	9.55	30.3	6.86	9.46	1.386	1.238	0.73	0.31
0.33	0.85	10^{-7}	8.32	9.55	31.9	5.35	9.46	1.386	1.238	0.73	0.31
0.33	1.0	10^{-7}	8.32	9.61	18.6	3.87	9.50	1.388	1.233	0.74	0.32
0.33	0.7	5×10^{-8}	8.29	9.61	52.7	13.8	9.51	1.388	1.247	0.75	0.32
0.33	0.85	5×10^{-8}	8.29	9.61	49.2	10.8	9.51	1.388	1.249	0.75	0.33
0.33	1.0	5×10^{-8}	8.28	9.61	52.7	7.76	9.51	1.388	1.246	0.75	0.33
1.00	0.7	10^{-6}				Off-center carbon ignition					
1.00	0.85	10^{-6}				Off-center carbon ignition					
1.00	1.0	10^{-6}				Off-center carbon ignition					
1.00	0.7	10^{-7}	8.30	9.62	27.3	6.86	9.52	1.386	1.223	1.62	0.35

Table 9: Results for the models with a cooling age of 1 Gyr (continued).

Z	$M^0_{\rm WD}$	$\dot{M}$	$\log T_{\rm c}^{\rm sim}$	$\log \rho_{\rm c}^{\rm sim}$	$\Delta {\rm t}^{\rm sim}$	t	$\log \rho_{\rm c}$	$M_{\rm WD}$	$M_{\rm conv}$	$10^3\eta_{\rm c}$	$10^3(\eta_{\rm c}-\eta_{\rm c,0})$
$[Z_\odot]$	$[M_\odot]$	$[M_\odot\,{\rm yr}^{-1}]$	[K]	$[{\rm g\,cm}^{-3}]$	[kyr]	[Myr]	$[{\rm g\,cm}^{-3}]$	$[M_\odot]$	$[M_\odot]$		
1.00	0.85	10^{-7}	8.29	9.62	28.4	5.36	9.52	1.386	1.222	1.61	0.35
1.00	1.0	10^{-7}	8.29	9.65	21.3	3.87	9.55	1.387	1.221	1.63	0.36
1.00	0.7	5×10^{-8}	Convection zone splits during simmering								
1.00	0.85	5×10^{-8}	Convection zone splits during simmering								
1.00	1.0	5×10^{-8}	Convection zone splits during simmering								
2.79	0.7	10^{-6}	Off-center carbon ignition								
2.79	0.85	10^{-6}	Off-center carbon ignition								
2.79	1.0	10^{-6}	Off-center carbon ignition								
2.79	0.7	10^{-7}	Convection zone splits during simmering								
2.79	0.85	10^{-7}	Convection zone splits during simmering								
2.79	1.0	10^{-7}	Convection zone splits during simmering								
2.79	0.7	5×10^{-8}	Convection zone splits during simmering								
2.79	0.85	5×10^{-8}	Convection zone splits during simmering								
2.79	1.0	5×10^{-8}	Convection zone splits during simmering								

Table 10: Results for the models with a cooling age of 10 Gyr.

Z	$M^0_{\rm WD}$	$\dot{M}$	$\log T_{\rm c}^{\rm sim}$	$\log \rho_{\rm c}^{\rm sim}$	$\Delta {\rm t}^{\rm sim}$	t	$\log \rho_{\rm c}$	$M_{\rm WD}$	$M_{\rm conv}$	$10^3\eta_{\rm c}$	$10^3(\eta_{\rm c}-\eta_{\rm c,0})$
$[Z_\odot]$	$[M_\odot]$	$[M_\odot\,{\rm yr}^{-1}]$	[K]	$[{\rm g\,cm}^{-3}]$	[kyr]	[Myr]	$[{\rm g\,cm}^{-3}]$	$[M_\odot]$	$[M_\odot]$		
0.01	0.7	10^{-6}				Off-center carbon ignition					
0.01	0.85	10^{-6}				Off-center carbon ignition					
0.01	1.0	10^{-6}				Off-center carbon ignition					
0.01	0.7	10^{-7}	8.36	9.50	34.2	6.84	9.41	1.384	1.247	0.33	0.32
0.01	0.85	10^{-7}	8.35	9.51	31.2	5.34	9.41	1.384	1.249	0.33	0.32
0.01	1.0	10^{-7}	8.31	9.73	3.79	3.91	9.60	1.393	1.211	0.42	0.40
0.01	0.7	5×10^{-8}	8.32	9.56	52.6	13.7	9.46	1.387	1.255	0.34	0.32
0.01	0.85	5×10^{-8}	8.33	9.56	51.6	10.7	9.46	1.387	1.259	0.33	0.32
0.01	1.0	5×10^{-8}	8.31	9.60	40.2	7.76	9.49	1.388	1.252	0.33	0.32
0.10	0.7	10^{-6}				Off-center carbon ignition					
0.10	0.85	10^{-6}				Off-center carbon ignition					
0.10	1.0	10^{-6}				Off-center carbon ignition					
0.10	0.7	10^{-7}	8.33	9.53	31.8	6.83	9.44	1.386	1.242	0.45	0.32
0.10	0.85	10^{-7}	8.33	9.54	31.4	5.36	9.45	1.386	1.244	0.45	0.32
0.10	1.0	10^{-7}	8.29	9.72	5.10	3.92	9.60	1.392	1.207	0.54	0.41

Table 10: Results for the models with a cooling age of 10 Gyr (continued).

Z	$M^0_{\rm WD}$	$\dot{M}$	$\log T_{\rm c}^{\rm sim}$	$\log \rho_{\rm c}^{\rm sim}$	$\Delta {\rm t}^{\rm sim}$	t	$\log \rho_{\rm c}$	$M_{\rm WD}$	$M_{\rm conv}$	$10^3\eta_{\rm c}$	$10^3(\eta_{\rm c}-\eta_{\rm c,0})$
$[Z_\odot]$	$[M_\odot]$	$[M_\odot\,{\rm yr}^{-1}]$	[K]	$[{\rm g\,cm}^{-3}]$	[kyr]	[Myr]	$[{\rm g\,cm}^{-3}]$	$[M_\odot]$	$[M_\odot]$		
0.10	0.7	5×10^{-8}	8.30	9.59	50.8	13.8	9.49	1.388	1.248	0.46	0.33
0.10	0.85	5×10^{-8}	8.30	9.59	52.9	10.8	9.49	1.388	1.250	0.45	0.32
0.10	1.0	5×10^{-8}	8.30	9.60	50.6	7.70	9.50	1.388	1.252	0.46	0.33
0.33	0.7	10^{-6}	Off-center carbon ignition								
0.33	0.85	10^{-6}	Off-center carbon ignition								
0.33	1.0	10^{-6}	Off-center carbon ignition								
0.33	0.7	10^{-7}	8.33	9.55	29.6	6.86	9.46	1.386	1.238	0.73	0.31
0.33	0.85	10^{-7}	8.33	9.56	28.2	5.36	9.46	1.386	1.239	0.73	0.31
0.33	1.0	10^{-7}	8.28	9.73	6.12	3.92	9.60	1.392	1.206	0.84	0.41
0.33	0.7	5×10^{-8}	8.29	9.61	51.4	13.8	9.50	1.388	1.247	0.75	0.32
0.33	0.85	5×10^{-8}	8.29	9.61	55.6	10.7	9.51	1.388	1.247	0.75	0.33
0.33	1.0	5×10^{-8}	8.27	9.63	47.7	7.77	9.53	1.389	1.246	0.76	0.33
1.00	0.7	10^{-6}	Off-center carbon ignition								
1.00	0.85	10^{-6}	Off-center carbon ignition								
1.00	1.0	10^{-6}	Off-center carbon ignition								
1.00	0.7	10^{-7}	8.29	9.62	28.2	6.86	9.52	1.387	1.223	1.62	0.35

Table 10: Results for the models with a cooling age of 10 Gyr (continued).

Z	$M^0_{\rm WD}$	$\dot{M}$	$\log T_{\rm c}^{\rm sim}$	$\log \rho_{\rm c}^{\rm sim}$	$\Delta {\rm t}^{\rm sim}$	t	$\log \rho_{\rm c}$	$M_{\rm WD}$	$M_{\rm conv}$	$10^3\eta_{\rm c}$	$10^3(\eta_{\rm c}-\eta_{\rm c,0})$
$[Z_\odot]$	$[M_\odot]$	$[M_\odot\,{\rm yr}^{-1}]$	[K]	$[{\rm g\,cm}^{-3}]$	[kyr]	[Myr]	$[{\rm g\,cm}^{-3}]$	$[M_\odot]$	$[M_\odot]$		
1.00	0.85	10^{-7}	8.29	9.61	30.1	5.36	9.53	1.386	1.226	1.62	0.35
1.00	1.0	10^{-7}	8.21	9.72	18.4	3.89	9.62	1.390	1.200	1.72	0.45
1.00	0.7	5×10^{-8}	Convection zone splits during simmering								
1.00	0.85	5×10^{-8}	Convection zone splits during simmering								
1.00	1.0	5×10^{-8}	8.25	9.67	54.0	7.76	9.57	1.388	1.235	1.64	0.38
2.79	0.7	10^{-6}	Off-center carbon ignition								
2.79	0.85	10^{-6}	Off-center carbon ignition								
2.79	1.0	10^{-6}	Off-center carbon ignition								
2.79	0.7	10^{-7}	Convection zone splits during simmering								
2.79	0.85	10^{-7}	Convection zone splits during simmering								
2.79	1.0	10^{-7}	8.16	9.72	21.8	3.83	9.62	1.383	1.200	4.03	0.51
2.79	0.7	5×10^{-8}	Convection zone splits during simmering								
2.79	0.85	5×10^{-8}	Convection zone splits during simmering								
2.79	1.0	5×10^{-8}	Convection zone splits during simmering								

BIBLIOGRAPHY

Ajzenberg-Selove, F. 1991, Nuclear Physics A, 523, 1

Aldering, G., Adam, G., Antilogus, P., et al. 2002, in Proc. SPIE, Vol. 4836, Survey and Other Telescope Technologies and Discoveries, ed. J. A. Tyson & S. Wolff, 61–72

Althaus, L. G., & Benvenuto, O. G. 1997, ApJ, 477, 313

Althaus, L. G., Córsico, A. H., Isern, J., & García-Berro, E. 2010, A&A Rev., 18, 471

Anders, E., & Grevesse, N. 1989, Geochim. Cosmochim. Acta, 53, 197

Anderson, J. P., González-Gaitán, S., Hamuy, M., et al. 2014, ApJ, 786, 67

Andrews, B. H., Weinberg, D. H., Schönrich, R., & Johnson, J. A. 2017, ApJ, 835, 224

Arcavi, I., Howell, D. A., Kasen, D., et al. 2017, Nature, 551, 210

Arnaud, K. A. 1996, in Astronomical Society of the Pacific Conference Series, Vol. 101, Astronomical Data Analysis Software and Systems V, ed. G. H. Jacoby & J. Barnes, 17

Arnett, D. 1996, Supernovae and Nucleosynthesis: An Investigation of the History of Matter from the Big Bang to the Present

Arnett, W. D. 1982, ApJ, 253, 785

Ashall, C., Mazzali, P. A., Pian, E., & James, P. A. 2016, MNRAS, 463, 1891

Asplund, M., Grevesse, N., Sauval, A. J., & Scott, P. 2009, ARA&A, 47, 481

Badenes, C. 2010, Proceedings of the National Academy of Science, 107, 7141

Badenes, C., Borkowski, K. J., & Bravo, E. 2005, ApJ, 624, 198

Badenes, C., Borkowski, K. J., Hughes, J. P., Hwang, U., & Bravo, E. 2006, ApJ, 645, 1373

Badenes, C., Bravo, E., Borkowski, K. J., & Domínguez, I. 2003, ApJ, 593, 358

Badenes, C., Bravo, E., & Hughes, J. P. 2008a, ApJ, 680, L33

Badenes, C., Hughes, J. P., Bravo, E., & Langer, N. 2007, ApJ, 662, 472

Badenes, C., Hughes, J. P., Cassam-Chenaï, G., & Bravo, E. 2008b, ApJ, 680, 1149

Badenes, C., & Maoz, D. 2012, ApJ, 749, L11

Barkat, Z., & Wheeler, J. C. 1990, ApJ, 355, 602

Berkhuijsen, E. M., & Fletcher, A. 2008, MNRAS, 390, L19

Bersten, M. C., & Mazzali, P. A. 2017, Light Curves of Type I Supernovae, ed. A. W. Alsabti & P. Murdin, 723

Betoule, M., Kessler, R., Guy, J., et al. 2014, A&A, 568, A22

Blondin, J. M., & Lufkin, E. A. 1993, ApJS, 88, 589

Blondin, S., Dessart, L., Hillier, D. J., & Khokhlov, A. M. 2013, MNRAS, 429, 2127

—. 2017, MNRAS, 470, 157

Bloom, J. S., Kasen, D., Shen, K. J., et al. 2012, ApJ, 744, L17

Borkowski, K. J., Lyerly, W. J., & Reynolds, S. P. 2001, ApJ, 548, 820

Borkowski, K. J., Reynolds, S. P., Hwang, U., et al. 2013, ApJ, 771, L9

Botyánszki, J., & Kasen, D. 2017, ApJ, 845, 176

Brachwitz, F., Dean, D. J., Hix, W. R., et al. 2000, ApJ, 536, 934

Bravo, E. 2013, A&A, 550, A24

Bravo, E., Badenes, C., & Martínez-Rodríguez, H. 2019, MNRAS, 482, 4346

Bravo, E., Domínguez, I., Badenes, C., Piersanti, L., & Straniero, O. 2010, ApJ, 711, L66

Bravo, E., Gil-Pons, P., Gutiérrez, J. L., & Doherty, C. L. 2016, A&A, 589, A38

Bravo, E., & Martínez-Pinedo, G. 2012, Phys. Rev. C, 85, 055805

Broersen, S., Chiotellis, A., Vink, J., & Bamba, A. 2014, MNRAS, 441, 3040

Brooks, J., Schwab, J., Bildsten, L., Quataert, E., & Paxton, B. 2017, ApJ, 843, 151

Bruenn, S. W. 1973, ApJ, 183, L125

Bucher, B., Tang, X. D., Fang, X., et al. 2015, Physical Review Letters, 114, 251102

Burkey, M. T., Reynolds, S. P., Borkowski, K. J., & Blondin, J. M. 2013, ApJ, 764, 63

Carlton, A. K., Borkowski, K. J., Reynolds, S. P., et al. 2011, ApJ, 737, L22

Carroll, S. M. 2004, Spacetime and geometry. An introduction to general relativity

Cassam-Chenaï, G., Hughes, J. P., Reynoso, E. M., Badenes, C., & Moffett, D. 2008, ApJ, 680, 1180

Castro, D., Lopez, L. A., Slane, P. O., et al. 2013, ApJ, 779, 49

Castro, D., Slane, P., Ellison, D. C., & Patnaude, D. J. 2012, ApJ, 756, 88

Caughlan, G. R., & Fowler, W. A. 1988, Atomic Data and Nuclear Data Tables, 40, 283

Chakraborti, S., Childs, F., & Soderberg, A. 2016, ApJ, 819, 37

Chamulak, D. A., Brown, E. F., Timmes, F. X., & Dupczak, K. 2008, ApJ, 677, 160

Chen, X., Han, Z., & Meng, X. 2014, MNRAS, 438, 3358

Chiotellis, A., Schure, K. M., & Vink, J. 2012, A&A, 537, A139

Chomiuk, L., Soderberg, A. M., Chevalier, R. A., et al. 2016, ApJ, 821, 119

Choudhury, S., Subramaniam, A., & Cole, A. A. 2016, MNRAS, 455, 1855

Clifford, F. E., & Tayler, R. J. 1965, MmRAS, 69, 21

Colgate, S. A., & McKee, C. 1969, ApJ, 157, 623

Cyburt, R. H., Amthor, A. M., Ferguson, R., et al. 2010, ApJS, 189, 240

Dalla Vecchia, C., & Schaye, J. 2012, MNRAS, 426, 140

De, S., Timmes, F. X., Brown, E. F., et al. 2014, ApJ, 787, 149

De Horta, A. Y., Filipovic, M. D., Crawford, E. J., et al. 2014, Serbian Astronomical Journal, 189, 41

Deloye, C. J., & Bildsten, L. 2002, ApJ, 580, 1077

Denissenkov, P. A., Truran, J. W., Herwig, F., et al. 2015, MNRAS, 447, 2696

Driebe, T., Schoenberner, D., Bloecker, T., & Herwig, F. 1998, A&A, 339, 123

Dwarkadas, V. V., & Chevalier, R. A. 1998, ApJ, 497, 807

Ellison, D. C., Patnaude, D. J., Slane, P., Blasi, P., & Gabici, S. 2007, ApJ, 661, 879

Ellison, D. C., Patnaude, D. J., Slane, P., & Raymond, J. 2010, ApJ, 712, 287

Fang, X., Tan, W. P., Beard, M., et al. 2017, Phys. Rev. C, 96, 045804

Farmer, R., Fields, C. E., Petermann, I., et al. 2016, ApJS, 227, 22

Ferrière, K. 1998, ApJ, 497, 759

Ferrière, K. M. 2001, Reviews of Modern Physics, 73, 1031

Fields, C. E., Farmer, R., Petermann, I., Iliadis, C., & Timmes, F. X. 2016, ApJ, 823, 46

Fields, C. E., Timmes, F. X., Farmer, R., et al. 2018, ApJS, 234, 19

Filippenko, A. V. 1997, ARA&A, 35, 309

Foster, A., Smith, R. K., Yamaguchi, H., Ji, L., & Wilms, J. 2014, in American Astronomical Society Meeting Abstracts, Vol. 223, American Astronomical Society Meeting Abstracts #223, 232.03

Foster, A. R., Ji, L., Smith, R. K., & Brickhouse, N. S. 2012, ApJ, 756, 128

Gal-Yam, A. 2012, Science, 337, 927

—. 2017, Observational and Physical Classification of Supernovae, ed. A. W. Alsabti & P. Murdin, 195

Galbany, L., Hamuy, M., Phillips, M. M., et al. 2016, AJ, 151, 33

Gamow, G., & Schoenberg, M. 1941, Physical Review, 59, 539

García-Berro, E., Althaus, L. G., Córsico, A. H., & Isern, J. 2008, ApJ, 677, 473

Ghavamian, P., Laming, J. M., & Rakowski, C. E. 2007, ApJ, 654, L69

Giacani, E., Smith, M. J. S., Dubner, G., et al. 2009, A&A, 507, 841

Gillessen, S., Eisenhauer, F., Trippe, S., et al. 2009, ApJ, 692, 1075

Goldstein, D. A., & Kasen, D. 2018, ApJ, 852, L33

Guillochon, J., Parrent, J., Kelley, L. Z., & Margutti, R. 2017, ApJ, 835, 64

Gvaramadze, V. V., Langer, N., Fossati, L., et al. 2017, Nature Astronomy, 1, 0116

Hachisu, I., Kato, M., & Nomoto, K. 1996, ApJ, 470, L97

Han, Z., & Podsiadlowski, P. 2004, MNRAS, 350, 1301

Hartmann, D., Woosley, S. E., & El Eid, M. F. 1985, ApJ, 297, 837

Haungs, A. 2015, Physics Procedia, 61, 425

Hawley, W. P., Athanassiadou, T., & Timmes, F. X. 2012, ApJ, 759, 39

Hayden, M. R., Bovy, J., Holtzman, J. A., et al. 2015, ApJ, 808, 132

Hillas, A. M. 2005, Journal of Physics G Nuclear Physics, 31, R95

Hillebrandt, W., & Niemeyer, J. C. 2000, ARA&A, 38, 191

Hopkins, P. F., Kereš, D., Oñorbe, J., et al. 2014, MNRAS, 445, 581

Horvath, J. E., & Valentim, R. 2017, The Masses of Neutron Stars, ed. A. W. Alsabti & P. Murdin, 1317

Howell, D. A. 2011, Nature Communications, 2, 350

—. 2017, Superluminous Supernovae, ed. A. W. Alsabti & P. Murdin, 431

Hoyle, F., & Fowler, W. A. 1960, ApJ, 132, 565

Hughes, J. P., Ghavamian, P., Rakowski, C. E., & Slane, P. O. 2003, ApJ, 582, L95

Hughes, J. P., Rakowski, C. E., & Decourchelle, A. 2000, ApJ, 543, L61

Iben, Jr., I. 1978, ApJ, 219, 213

Iben, Jr., I., & Tutukov, A. V. 1984, ApJS, 54, 335

Itoh, H. 1977, PASJ, 29, 813

Iwamoto, K., Brachwitz, F., Nomoto, K., et al. 1999, ApJS, 125, 439

Izzard, R. G., Ramirez-Ruiz, E., & Tout, C. A. 2004, MNRAS, 348, 1215

Jackson, A. P., Calder, A. C., Townsley, D. M., et al. 2010, ApJ, 720, 99

Janka, H.-T. 2012, Annual Review of Nuclear and Particle Science, 62, 407

Jerkstrand, A., Smartt, S. J., Inserra, C., et al. 2017, ApJ, 835, 13

Kalirai, J. S., Hansen, B. M. S., Kelson, D. D., et al. 2008, ApJ, 676, 594

Kalirai, J. S., Marigo, P., & Tremblay, P.-E. 2014, ApJ, 782, 17

Kalirai, J. S., Richer, H. B., Reitzel, D., et al. 2005, ApJ, 618, L123

Kalirai, J. S., Saul Davis, D., Richer, H. B., et al. 2009, ApJ, 705, 408

Kaneko, Y., Ramirez-Ruiz, E., Granot, J., et al. 2007, ApJ, 654, 385

Kasen, D. 2010, ApJ, 708, 1025

Kerzendorf, W. E., Childress, M., Scharwächter, J., Do, T., & Schmidt, B. P. 2014, ApJ, 782, 27

Kerzendorf, W. E., Schmidt, B. P., Asplund, M., et al. 2009, ApJ, 701, 1665

Kerzendorf, W. E., Schmidt, B. P., Laird, J. B., Podsiadlowski, P., & Bessell, M. S. 2012, ApJ, 759, 7

Kerzendorf, W. E., Strampelli, G., Shen, K. J., et al. 2017, ArXiv e-prints, arXiv:1709.06566

Khokhlov, A. M. 1991, A&A, 245, 114

Kobayashi, C., Umeda, H., Nomoto, K., Tominaga, N., & Ohkubo, T. 2006, ApJ, 653, 1145

Kosenko, D., Helder, E. A., & Vink, J. 2010, A&A, 519, A11

Krause, O., Tanaka, M., Usuda, T., et al. 2008, Nature, 456, 617

Kushnir, D., Katz, B., Dong, S., Livne, E., & Fernández, R. 2013, ApJ, 778, L37

Leahy, D. A., & Ranasinghe, S. 2016, ApJ, 817, 74

Lee, S.-H., Ellison, D. C., & Nagataki, S. 2012, ApJ, 750, 156

Lee, S.-H., Patnaude, D. J., Ellison, D. C., Nagataki, S., & Slane, P. O. 2014, ApJ, 791, 97

Lee, S.-H., Patnaude, D. J., Raymond, J. C., et al. 2015, ApJ, 806, 71

Lee, S.-H., Slane, P. O., Ellison, D. C., Nagataki, S., & Patnaude, D. J. 2013, ApJ, 767, 20

Lesaffre, P., Han, Z., Tout, C. A., Podsiadlowski, P., & Martin, R. G. 2006, MNRAS, 368, 187

Lesaffre, P., Podsiadlowski, P., & Tout, C. A. 2005, MNRAS, 356, 131

Lewis, K. T., Burrows, D. N., Hughes, J. P., et al. 2003, ApJ, 582, 770

Li, C.-J., Chu, Y.-H., Gruendl, R. A., et al. 2017, ApJ, 836, 85

Li, X.-D., & van den Heuvel, E. P. J. 1997, A&A, 322, L9

Limongi, M., & Chieffi, A. 2003, ApJ, 592, 404

Liu, Z.-W., Pakmor, R., Röpke, F. K., et al. 2013a, A&A, 554, A109

Liu, Z.-W., Pakmor, R., Seitenzahl, I. R., et al. 2013b, ApJ, 774, 37

Livio, M., & Mazzali, P. 2018, Phys. Rep., 736, 1

Lorén-Aguilar, P., Isern, J., & García-Berro, E. 2009, A&A, 500, 1193

Lovchinsky, I., Slane, P., Gaensler, B. M., et al. 2011, ApJ, 731, 70

Maeda, K., Röpke, F. K., Fink, M., et al. 2010, ApJ, 712, 624

Maggi, P., & Acero, F. 2017, A&A, 597, A65

Maggi, P., Haberl, F., Kavanagh, P. J., et al. 2016, A&A, 585, A162

Maguire, K., Sim, S. A., Shingles, L., et al. 2018, MNRAS, 477, 3567

Maoz, D., & Graur, O. 2017, ApJ, 848, 25

Maoz, D., Mannucci, F., & Brandt, T. D. 2012, MNRAS, 426, 3282

Maoz, D., Mannucci, F., & Nelemans, G. 2014, ARA&A, 52, 107

Margutti, R., Parrent, J., Kamble, A., et al. 2014, ApJ, 790, 52

Marion, G. H., Brown, P. J., Vinkó, J., et al. 2016, ApJ, 820, 92

Marquardt, K. S., Sim, S. A., Ruiter, A. J., et al. 2015, A&A, 580, A118

Martínez-Rodríguez, H., Piro, A. L., Schwab, J., & Badenes, C. 2016, ApJ, 825, 57

Martínez-Rodríguez, H., Badenes, C., Yamaguchi, H., et al. 2017, ApJ, 843, 35

Martínez-Rodríguez, H., Badenes, C., Lee, S.-H., et al. 2018, ApJ, 865, 151

Matteucci, F., Panagia, N., Pipino, A., et al. 2006, MNRAS, 372, 265

Matteucci, F., Spitoni, E., Recchi, S., & Valiante, R. 2009, A&A, 501, 531

Matteucci, F., & Tornambe, A. 1987, A&A, 185, 51

Mazzali, P. A., Kawabata, K. S., Maeda, K., et al. 2005a, Science, 308, 1284

Mazzali, P. A., Benetti, S., Altavilla, G., et al. 2005b, ApJ, 623, L37

Mazzali, P. A., Sullivan, M., Filippenko, A. V., et al. 2015, MNRAS, 450, 2631

McKee, C. F., & Truelove, J. K. 1995, Phys. Rep., 256, 157

McWilliam, A., Piro, A. L., Badenes, C., & Bravo, E. 2018, ApJ, 857, 97

Miles, B. J., van Rossum, D. R., Townsley, D. M., et al. 2016, ApJ, 824, 59

Minkowski, R. 1941, PASP, 53, 224

Mitsuda, K., Bautz, M., Inoue, H., et al. 2007, PASJ, 59, S1

Modjaz, M., Blondin, S., Kirshner, R. P., et al. 2014, AJ, 147, 99

Moreno-Raya, M. E., Mollá, M., López-Sánchez, Á. R., et al. 2016, ApJ, 818, L19

Moriya, T. J., Pruzhinskaya, M. V., Ergon, M., & Blinnikov, S. I. 2016, MNRAS, 455, 423

Morozova, V., Piro, A. L., Renzo, M., et al. 2015, ApJ, 814, 63

Nadyozhin, D. K., & Yudin, A. V. 2004, Astronomy Letters, 30, 634

Nandra, K., Barret, D., Barcons, X., et al. 2013, ArXiv e-prints, arXiv:1306.2307

Nicholl, M., Berger, E., Smartt, S. J., et al. 2016, ApJ, 826, 39

Nomoto, K. 1982, ApJ, 253, 798

Nomoto, K., & Hashimoto, M. 1988, Phys. Rep., 163, 13

Nomoto, K., Kobayashi, C., & Tominaga, N. 2013, ARA&A, 51, 457

Nomoto, K., Thielemann, F.-K., & Yokoi, K. 1984, ApJ, 286, 644

Nordström, B., Mayor, M., Andersen, J., et al. 2004, A&A, 418, 989

O'Connor, E. 2017, The Core-Collapse Supernova-Black Hole Connection, ed. A. W. Alsabti & P. Murdin, 1555

Ofek, E. O., Sullivan, M., Shaviv, N. J., et al. 2014, ApJ, 789, 104

Orlando, S., Miceli, M., Pumo, M. L., & Bocchino, F. 2016, ApJ, 822, 22

Paczyński, B. 1972, Astrophys. Lett., 11, 53

—. 1973, Acta Astron., 23, 1

Pakmor, R., Edelmann, P., Röpke, F. K., & Hillebrandt, W. 2012, MNRAS, 424, 2222

Pakmor, R., Kromer, M., Taubenberger, S., & Springel, V. 2013, ApJ, 770, L8

Pan, K.-C., Ricker, P. M., & Taam, R. E. 2013, ApJ, 773, 49

Pannuti, T. G., Kargaltsev, O., Napier, J. P., & Brehm, D. 2014, ApJ, 782, 102

Park, S., Hughes, J. P., Slane, P. O., et al. 2012, ApJ, 748, 117

Park, S., Badenes, C., Mori, K., et al. 2013, ApJ, 767, L10

Patnaude, D., & Badenes, C. 2017, Supernova Remnants as Clues to Their Progenitors, ed. A. W. Alsabti & P. Murdin, 2233

Patnaude, D. J., Badenes, C., Park, S., & Laming, J. M. 2012, ApJ, 756, 6

Patnaude, D. J., Ellison, D. C., & Slane, P. 2009, ApJ, 696, 1956

Patnaude, D. J., Lee, S.-H., Slane, P. O., et al. 2015, ApJ, 803, 101

—. 2017, ApJ, 849, 109

Patnaude, D. J., Slane, P., Raymond, J. C., & Ellison, D. C. 2010, ApJ, 725, 1476

Paxton, B., Bildsten, L., Dotter, A., et al. 2011, ApJS, 192, 3

Paxton, B., Cantiello, M., Arras, P., et al. 2013, ApJS, 208, 4

Paxton, B., Marchant, P., Schwab, J., et al. 2015, ApJS, 220, 15

—. 2016, ApJS, 223, 18

Pereira, R., Thomas, R. C., Aldering, G., et al. 2013, A&A, 554, A27

Perlmutter, S., Aldering, G., Goldhaber, G., et al. 1999, ApJ, 517, 565

Pian, E., Mazzali, P. A., Masetti, N., et al. 2006, Nature, 442, 1011

Piatti, A. E., & Geisler, D. 2013, AJ, 145, 17

Piersanti, L., Bravo, E., Cristallo, S., et al. 2017, ApJ, 836, L9

Pietrzyński, G., Graczyk, D., Gieren, W., et al. 2013, Nature, 495, 76

Piro, A. L. 2008, ApJ, 679, 616

Piro, A. L., & Bildsten, L. 2008, ApJ, 673, 1009

Piro, A. L., & Chang, P. 2008, ApJ, 678, 1158

Piro, A. L., & Morozova, V. S. 2016, ApJ, 826, 96

Piro, A. L., Thompson, T. A., & Kochanek, C. S. 2014, MNRAS, 438, 3456

Prantzos, N., Abia, C., Limongi, M., Chieffi, A., & Cristallo, S. 2018, MNRAS, 476, 3432

Rakowski, C. E., Badenes, C., Gaensler, B. M., et al. 2006, ApJ, 646, 982

Raskin, C., Scannapieco, E., Rockefeller, G., et al. 2010, ApJ, 724, 111

Raskin, C., Timmes, F. X., Scannapieco, E., Diehl, S., & Fryer, C. 2009, MNRAS, 399, L156

Rest, A., Suntzeff, N. B., Olsen, K., et al. 2005, Nature, 438, 1132

Rest, A., Welch, D. L., Suntzeff, N. B., et al. 2008a, ApJ, 681, L81

Rest, A., Matheson, T., Blondin, S., et al. 2008b, ApJ, 680, 1137

Rest, A., Scolnic, D., Foley, R. J., et al. 2014, ApJ, 795, 44

Reynolds, S. P., Borkowski, K. J., Green, D. A., et al. 2008, ApJ, 680, L41

Reynolds, S. P., Borkowski, K. J., Hwang, U., et al. 2007, ApJ, 668, L135

Reynoso, E. M., & Goss, W. M. 1999, AJ, 118, 926

Riess, A. G., Filippenko, A. V., Challis, P., et al. 1998, AJ, 116, 1009

Ritossa, C., Garcia-Berro, E., & Iben, Jr., I. 1996, ApJ, 460, 489

Rosswog, S., Kasen, D., Guillochon, J., & Ramirez-Ruiz, E. 2009, ApJ, 705, L128

Ruiz-Lapuente, P. 2018, arXiv e-prints, arXiv:1812.04977

Ruiz-Lapuente, P., Damiani, F., Bedin, L., et al. 2018, ApJ, 862, 124

Safi-Harb, S., Dubner, G., Petre, R., Holt, S. S., & Durouchoux, P. 2005, ApJ, 618, 321

Sankrit, R., Blair, W. P., Delaney, T., et al. 2005, Advances in Space Research, 35, 1027

Sarbadhicary, S. K., Chomiuk, L., Badenes, C., et al. 2017, ArXiv e-prints, arXiv:1709.05346

Scalzo, R. A., Ruiter, A. J., & Sim, S. A. 2014, MNRAS, 445, 2535

Schwab, J., Bildsten, L., & Quataert, E. 2017, MNRAS, 472, 3390

Schwab, J., Quataert, E., & Bildsten, L. 2015, MNRAS, 453, 1910

Schwab, J., Shen, K. J., Quataert, E., Dan, M., & Rosswog, S. 2012, MNRAS, 427, 190

Sedov, L. I. 1959, Similarity and Dimensional Methods in Mechanics

Seitenzahl, I. R., Cescutti, G., Röpke, F. K., Ruiter, A. J., & Pakmor, R. 2013a, A&A, 559, L5

Seitenzahl, I. R., Taubenberger, S., & Sim, S. A. 2009, MNRAS, 400, 531

Seitenzahl, I. R., Timmes, F. X., Marin-Laflèche, A., et al. 2008, ApJ, 685, L129

Seitenzahl, I. R., Ciaraldi-Schoolmann, F., Röpke, F. K., et al. 2013b, MNRAS, 429, 1156

Shappee, B. J., Kochanek, C. S., & Stanek, K. Z. 2013, ApJ, 765, 150

Shaviv, G., & Regev, O. 1977, A&A, 54, 581

Shen, K. J., & Bildsten, L. 2009, ApJ, 699, 1365

—. 2014, ApJ, 785, 61

Shen, K. J., Bildsten, L., Kasen, D., & Quataert, E. 2012, ApJ, 748, 35

Shen, K. J., Guillochon, J., & Foley, R. J. 2013, ApJ, 770, L35

Shen, K. J., Kasen, D., Miles, B. J., & Townsley, D. M. 2018, ApJ, 854, 52

Shen, K. J., & Moore, K. 2014, ApJ, 797, 46

Shklovskii, I. S. 1962, Soviet Ast., 6, 162

Sim, S. A., Röpke, F. K., Hillebrandt, W., et al. 2010, ApJ, 714, L52

Slane, P., Lee, S.-H., Ellison, D. C., et al. 2014, ApJ, 783, 33

Soker, N. 2018, Science China Physics, Mechanics, and Astronomy, 61, 49502

Sollerman, J., Lindahl, J., Kozma, C., et al. 2004, A&A, 428, 555

Sollerman, J., Taddia, F., Arcavi, I., et al. 2019, A&A, 621, A30

Someya, K., Bamba, A., & Ishida, M. 2014, PASJ, 66, 26

Starrfield, S., Truran, J. W., Sparks, W. M., & Kutter, G. S. 1972, ApJ, 176, 169

Stehle, M., Mazzali, P. A., Benetti, S., & Hillebrandt, W. 2005, MNRAS, 360, 1231

Stein, J., & Wheeler, J. C. 2006, ApJ, 643, 1190

Stinson, G., Seth, A., Katz, N., et al. 2006, MNRAS, 373, 1074

Sukhbold, T., Ertl, T., Woosley, S. E., Brown, J. M., & Janka, H.-T. 2016, ApJ, 821, 38

Sukhbold, T., & Woosley, S. E. 2016, ApJ, 820, L38

Tanaka, M., Mazzali, P. A., Stanishev, V., et al. 2011, MNRAS, 410, 1725

Tashiro, M., Maejima, H., Toda, K., et al. 2018, in Society of Photo-Optical Instrumentation Engineers (SPIE) Conference Series, Vol. 10699

Taylor, G. 1950, Proceedings of the Royal Society of London Series A, 201, 159

Thielemann, F.-K., Nomoto, K., & Yokoi, K. 1986, A&A, 158, 17

Thornton, K., Gaudlitz, M., Janka, H.-T., & Steinmetz, M. 1998, ApJ, 500, 95

Tian, W. W., & Leahy, D. A. 2011, ApJ, 729, L15

—. 2014, ApJ, 783, L2

Timmes, F. X., Brown, E. F., & Truran, J. W. 2003, ApJ, 590, L83

Timmes, F. X., Woosley, S. E., & Weaver, T. A. 1996, ApJ, 457, 834

Toki, H., Suzuki, T., Nomoto, K., Jones, S., & Hirschi, R. 2013, Phys. Rev. C, 88, 015806

Tominaga, N., Tanaka, M., Nomoto, K., et al. 2005, ApJ, 633, L97

Toonen, S., Nelemans, G., & Portegies Zwart, S. 2012, A&A, 546, A70

Toonen, S., Perets, H. B., & Hamers, A. S. 2018, A&A, 610, A22

Townsley, D. M., Jackson, A. P., Calder, A. C., et al. 2009, ApJ, 701, 1582

Townsley, D. M., Miles, B. J., Timmes, F. X., Calder, A. C., & Brown, E. F. 2016, ApJS, 225, 3

Travaglio, C., Hillebrandt, W., Reinecke, M., & Thielemann, F.-K. 2004, A&A, 425, 1029

Travaglio, C., Röpke, F. K., Gallino, R., & Hillebrandt, W. 2011, ApJ, 739, 93

Truelove, J. K., & McKee, C. F. 1999, ApJS, 120, 299

Tsuruta, S., & Cameron, A. G. W. 1970, Ap&SS, 7, 374

van der Heyden, K. J., Bleeker, J. A. M., Kaastra, J. S., & Vink, J. 2003, A&A, 406, 141

van Kerkwijk, M. H., Chang, P., & Justham, S. 2010, ApJ, 722, L157

Vink, J. 2012, A&A Rev., 20, 49

—. 2016, ArXiv e-prints, arXiv:1612.06905

Vogt, F., & Dopita, M. A. 2011, Ap&SS, 331, 521

Wang, B. 2018, Research in Astronomy and Astrophysics, 18, 049

Wang, B., & Han, Z. 2012, New A Rev., 56, 122

Warren, D. C., & Blondin, J. M. 2013, MNRAS, 429, 3099

Warren, J. S., & Hughes, J. P. 2004, ApJ, 608, 261

Warren, J. S., Hughes, J. P., Badenes, C., et al. 2005, ApJ, 634, 376

Webbink, R. F. 1984, ApJ, 277, 355

Weiler, K. W., & Panagia, N. 1978, A&A, 70, 419

Weinberg, D. H., Andrews, B. H., & Freudenburg, J. 2017, ApJ, 837, 183

Wilk, K. D., Hillier, D. J., & Dessart, L. 2018, MNRAS, 474, 3187

Williams, B. J., Blair, W. P., Blondin, J. M., et al. 2011, ApJ, 741, 96

Williams, B. J., Borkowski, K. J., Reynolds, S. P., et al. 2014, ApJ, 790, 139

Wolf, W. M., Bildsten, L., Brooks, J., & Paxton, B. 2013, ApJ, 777, 136

Wolfire, M. G., McKee, C. F., Hollenbach, D., & Tielens, A. G. G. M. 2003, ApJ, 587, 278

Woltjer, L. 1972, ARA&A, 10, 129

Woods, T. E., Ghavamian, P., Badenes, C., & Gilfanov, M. 2017, Nature Astronomy, 1, 263

—. 2018, ArXiv e-prints, arXiv:1807.03798

Woosley, S., & Janka, T. 2005, Nature Physics, 1, 147

Woosley, S. E., Arnett, W. D., & Clayton, D. D. 1971, Physical Review Letters, 27, 213

Woosley, S. E., & Bloom, J. S. 2006, ARA&A, 44, 507

Woosley, S. E., & Heger, A. 2007, Phys. Rep., 442, 269

Woosley, S. E., Heger, A., & Weaver, T. A. 2002, Reviews of Modern Physics, 74, 1015

Woosley, S. E., & Kasen, D. 2011, ApJ, 734, 38

Woosley, S. E., & Weaver, T. A. 1994, ApJ, 423, 371

—. 1995, ApJS, 101, 181

Woosley, S. E., Wunsch, S., & Kuhlen, M. 2004, ApJ, 607, 921

Wunsch, S., & Woosley, S. E. 2004, ApJ, 616, 1102

Yamaguchi, H., Koyama, K., & Uchida, H. 2012a, ArXiv e-prints, arXiv:1202.1594

Yamaguchi, H., Tanaka, M., Maeda, K., et al. 2012b, ApJ, 749, 137

Yamaguchi, H., Koyama, K., Katsuda, S., et al. 2008, PASJ, 60, S141

Yamaguchi, H., Badenes, C., Petre, R., et al. 2014a, ApJ, 785, L27

Yamaguchi, H., Eriksen, K. A., Badenes, C., et al. 2014b, ApJ, 780, 136

Yamaguchi, H., Badenes, C., Foster, A. R., et al. 2015, ApJ, 801, L31

Yaron, O., & Gal-Yam, A. 2012, PASP, 124, 668

Zegers, R. G. T., Brown, E. F., Akimune, H., et al. 2008, Phys. Rev. C, 77, 024307

Zhao, X., Wang, X., Maeda, K., et al. 2015, ApJS, 220, 20